Optical permeability characterization and evolution of a natural single fracture

Zur Erlangung des akademischen Grades eines

Doktors der Naturwissenschaften (Dr. rer. nat.)

von der KIT-Fakultät für
Bauingenieur-, Geo- und Umweltwissenschaften
des Karlsruher Instituts für Technologie (KIT)

genehmigte

Dissertation

von

M.Sc. Marco Fuchs

Tag der mündlichen Prüfung: 09. Januar 2026

Referent: Prof. Dr. Philipp Blum
Korreferent: Prof. Dr. Martin O. Saar

Karlsruhe 2026

Abstract

The permeability of the subsurface is a crucial parameter for the feasibility of many geoscientific applications, such as shallow and deep geothermal energy, nuclear waste disposal, the storage of energy carriers (e.g., hydrogen) and CO_2, as well as tunnel construction. Most of these applications occur at depths where the rock matrix exhibits low permeability. Consequently, subsurface fluid flow predominantly occurs in secondary structures such as karst conduits, fault zones, or fractures. The latter is particularly relevant in the context of increasingly important energy policy issues mentioned above. Thus, this thesis focuses on developing novel approaches, advancing existing methods for characterizing permeability, and investigating the underlying hydro-mechanical processes in natural single fractures.

The first part of this thesis addresses the further development of methodological approaches to characterize the permeability of a single fracture. The first study of this cumulative thesis focuses on the digital representation of fracture surfaces, which forms the basis for many permeability-determining methods. For this purpose, a portable 3D laser scanner, a combined system of a mounted 3D laser scanner and a robotic arm, as well as the photogrammetric "Structure from Motion" method, are compared and evaluated for their suitability in determining the permeability of single fractures. Flow simulations are conducted using the geometries generated by each method and calibrated against experimental air permeameter measurements. The study, as well as the entire thesis, was conducted on a bedding joint in Flechtinger Sandstone, a well-researched German reservoir rock. The results show that the portable laser scanner cannot accurately capture the fracture surface, which is attributed to its low resolution and precision, rendering it unsuitable for permeability determination. The other two methods can adequately capture the fracture surface but yield higher permeability values compared to the calibration data. Consequently, the initial contact area of the fractures was increased. At contact areas of 5 - 7 % of the total fracture surface, the simulated permeability aligns with the air permeameter measurements.

Building on the results of the first study, the second study uses a topological analysis of the obtained fracture geometry as a basis to characterize permeability. The method of persistent homology was selected, which has previously been applied to porous media and fracture networks, and was validated using air permeameter measurements and numerical simulations. Persistent homology was applied to three datasets of the same fracture at different resolutions (200 µm, 100 µm, and 50 µm). The results show, on the one hand, that the estimated permeabilities are within the same order of magnitude as the validation data. On the other hand, it is shown that the relative error compared to the validation data decreases with increasing resolution. However, in terms of quality and time requirements, it becomes evident that the improve-

ment in quality from a resolution of 100 µm to 50 µm is marginal, while the analysis time increases by 75 %.

The second part of the thesis, consisting of the third study, focuses on changes in permeability due to shear displacement of the fracture under varying normal stresses. A novel method is employed that combines a mechanical Discrete Element Method (DEM) model with a hydraulic Finite Element Method (FEM) model. This enables a realistic representation of the mechanical behavior of the single fracture during simulations of direct shear tests and allows for the reconstruction of the sheared fracture surfaces at each stage of the test. The combined shear tests were simulated under six different normal stress conditions (1.5 MPa – 15.0 MPa). The results reveal three distinct regimes: (1) At low normal stresses (< 4.0 MPa), the fracture mechanically dilates on intact asperities, resulting in increased permeability. (2) At normal stresses between 4.0 MPa and 4.5 MPa, a transition occurs, aperities start to break, and permeability remains constant during the shear test. Furthermore, a pronounced anisotropy in permeability is observed. (3) By further increasing normal stresses > 4.5 MPa, the fracture mechanically closes due to mechanical deformation and gouge formation, leading also to hydraulic closure. It is observed that the transition at 4.0 MPa corresponds precisely to the weakest mechanical property of the rock, the ultimate tensile strength, which is also 4.0 MPa for Flechtinger Sandstone.

Kurzfassung

Die Permeabilität des Untergrunds ist eine entscheidende Größe für die Machbarkeit vieler geowissenschaftlicher Anwendungen wie der oberflächennahen und tiefen Geothermie, der sicheren Endlagerung radioaktiver Abfälle, der Speicherung von Energieträgern (z.B. Wasserstoff) und CO_2 oder des Tunnelbaus. Die meisten dieser Anwendungen befinden sich in Tiefenbereichen, in denen die Gesteine eine geringe Matrixpermeabilität aufweisen. Folglich findet der unterirdische Fluidfluss besonders in sekundären Strukturen wie Karst, Störungszonen oder Klüften statt. Letztere spielen vor allem in den zunehmend an Relevanz gewinnenden, oben aufgeführten, energierpolitischen Fragestellungen eine wichtige Rolle. Diese Arbeit fokussiert sich deshalb auf die Entwicklung neuartiger Ansätze und die Weiterentwicklung bestehender Methoden zur Charakterisierung der Permeabilität und Erforschung der zugrunde liegenden hydro-mechanischen Prozesse in natürlichen Einzelklüften.

Der erste Teil dieser Thesis beschäftigt sich mit der Weiterentwicklung von methodischen Ansätzen zur Permeabilitätsbestimmung einer Einzelkluft. Die erste Studie behandelt die digitale Abbildung von Kluftflächen, die die Grundlage für viele permeabilitätsbestimmende Methoden bildet. Hierzu werden ein tragbarer 3D-Laserscanner, ein kombiniertes System aus hochauflösendem 3D-Laserscanner und robotischem Arm sowie die photogrammetrische „Structure from Motion“-Methode verglichen und für ihren weiteren Einsatz in der Permeabilitätsbestimmung von Einzelklüften evaluiert. Mit der jeweils erzeugten Geometrie werden Durchflusssimulationen durchgeführt und mit experimentell ermittelten Luftpermeametermessungen kalibriert. Die Studie wie auch die gesamte Arbeit wurden an einer Schichtfuge in Flechtinger Sandstein, einem bekannten deutschen Reservoirgestein, durchgeführt. Die Ergebnisse zeigen, dass der tragbare Laserscanner die Kluftfläche nicht akkurat abbilden kann, was aufgrund seiner geringen Auflösung und Genaugkeit erklärt werden kann und somit für die Permeabilitätsbestimmung ungeeignet ist. Die beiden anderen Methoden können die Kluftfläche zwar hinreichend gut abbilden, weisen aber erhöhte Permeabilitätswerte verglichen mit den Kalibrationsdaten auf. Folglich wurde die initiale Kontaktfläche der Klüfte erhöht. Bei relativen Kontaktflächen von 5 – 7 % der Gesamtkluftfläche weist die Kluft eine übereinstimmende Permeabilität zu den Luftpermeametermessungen auf.

Aufbauend auf den Ergebnissen der ersten Studie wurde in der zweiten Studie die Kluftgeometrie als Grundlage dafür verwendet, eine topologische Methode zu entwickeln, die die Permeabilität ohne den Einsatz einer experimentellen Messung oder eines numerischen Modells abschätzen kann. Dafür wurde die Methode der persistenten Homologie ausgewählt, die zuvor schon für poröse Medien und Kluftnetzwerke eingesetzt worden war und mit Luftpermeametermessungen sowie numerischen Simulationen validiert wurde. Die persistente Homologie wurde an drei Datensätzen derselben Kluft mit unterschiedlicher Auflösung angewendet (200 µm, 100 µm und 50 µm). Die Ergebnisse zeigen zum einen, dass die ermittelten Permeabilitäten in der Größenordnung der Validierungsdaten liegen. Zum anderen kann gezeigt werden, dass mit zunehmender Auflösung der relative Fehler zu den Validierungsdaten abnimmt. Bei Betrachtung der Qualität und der Zeitbeanspruchung zeigt sich jedoch, dass die Qualitätsteigerung bei einer Erhöhung der Auflösung von 100 µm zu 50 µm marginal ist, wohingegen sich die aufzubringende Analysezeit um 75 % verlängert.

Der zweite Teil der Thesis, der die dritte Studie umfasst, konzentriert sich auf die Änderung der Permeabilität durch Scherung der Kluft unter verschiedenen Normalspannungen. Hierzu wird eine neuartige Methode entwickelt, bei der ein mechanisches Diskrete-Elemente-Methoden (DEM)-Modell mit einem hydraulischen Finite-Elemente-Methoden (FEM)-Modell kombiniert wird. Dies ermöglicht eine realistische Abbildung des mechanischen Verhaltens der Einzelkluft in Simulationen von Scherversuchen sowie die Rekonstruktion der abgescherten Kluftflächen zu jedem Zeitpunkt des Scherversuchs. Die kombinierten Scherversuche wurden unter sechs Normalspannungsbedingungen simuliert (1,5 MPa – 15,0 MPa). Die Ergebnisse zeigen, dass drei hydraulische Regime unterschieden werden können: (1) Bei geringen Normalspannungen (< 4,0 MPa) öffnet sich die Kluft durch die Scherung mechanisch und die Permeabilität nimmt zu. (2) Bei Normalspannungen zwischen 4,0 MPa und 4,5 MPa kommt es zu einem Wechsel der Permeabilitätsentwicklung und die Permeabilität nimmt durch die Scherung nicht mehr zu, sondern bleibt über den Verlauf des Scherversuchs konstant. Zudem ist eine ausgeprägte Anisotropie der Permeabilität zu beobachten. (3) Bei Normalspannungen > 4,5 MPa schließt sich die Kluft durch die Scherung hydraulisch, was vor allem mit der mechanischen Deformation der Kluft sowie der Bildung von Abriebmaterial erklärt werden kann. Es wird beobachtet, dass der Wechsel bei etwa 4,0 MPa genau der schwächsten mechanischen Gesteinseigenschaft, der maximalen Zugfestigkeit, die ebenfalls 4,0 MPa für Flechtinger Sandstein beträgt, eintritt.

List of contents

List of figures

List of tables

List of abbreviations

a	Aperture	L
a_h	Hydraulic aperture	L
a_m	Mechanical aperture	L
A	Cross-sectional area of the flow domain	L^2
$A_{c,r}$	Relative contact area	[-]
A_{int}	Interacting surface	L^2
ARR	Accuracy-resolution ratio	[-]
b	Birth (= Creation of a new flow path)	[-]
c	Cohesion	$M/(LT^2)$
CCS	Carbon capture and storage	
CT	Computed tomography	
d	Death (= Closure of an existing flow path)	[-]
D	Displacement	L
DE	Discrete element	
DFN	Discrete fracture networks	
DIM	Dense image matching	
DST	Direct shear test	
E_{eq}	Bulk modulus equivalent	$M/(LT^2)$
EGS	Enhanced geothermal system	
F	Fluid flux	$M/(L^2T)$
$F^{advective}$	Advective fluid flux	$M/(L^2T)$
$F^{diff+disp}$	Diffusive and dispersive fluid flux	$M/(L^2T)$
F_{int}	Interaction force	ML/T^2
F_n	Normal component of the interaction force	ML/T^2
F_s	Shear component of the interaction force	MLT^2
g	Acceleration of gravity	L/T^2

GPU	Graphical processing unit	
h	Hydraulic head	L
H	Hurst exponent	
HLS	Handheld laser scanner	
HM	Hydro-mechanical	
k	Permeability	L^2
k_r	Relative permeability (function of saturation)	[-]
K	Hydraulic Conductivity	L/T
K_n	Normal stiffness	M/T^2
K_s	Shear stiffness	M/T^2
L	Length	L
LCL	Local cubic law	
M	Mass of fluid per bulk volume	M
MLS	Mounted laser scanner	
MOOSE	Multiphysics object-oriented simulation environment	
MVS	Multi-view stereo algorithm	
N	Number of elements	[-]
N_c	Number of elements in contact	[-]
NAPL	Non-aqueous phase liquid	
NRMSE	Normalized root mean squared error	
p	Hydraulic pressure	$M/(LT^2)$
PH	Persistent homology	
q	Fluid source/sink	$M/(L^3T)$
Q	Volumetric flow rate	L^3/T
r	Resolution	L
r_b	Resolution of the binary image	L
R	Radius	L
Re	Reynold’s number	[-]
RMSE	Root mean squared error	

SfM	Structure from motion	
t	Time	T
TDA	Topological data analysis	
THMC	Thermal-hydraulic-mechanical-chemical	
u_s	Tangential displacement	L
UTS	Ultimate tensile strength	$M/(LT^2)$
w	Depth of a flow channel	L
W	Width	L
v	Darcy velocity	L/T
v_s	Velocity of the solid skeleton	L/T
Λ	Radioactive decay rate	
μ	Dynamic viscosity	M/(LT)
ρ	Density	M/L^3
φ	Friction angle	
φ_r	Residual friction angle	
ΦI_{chem}	Chemical precipitation/dissolution	
χ	Mass fraction	

1 Introduction

1.1 Motivation

The permeability of a geological material is the parameter that describes the material's ability to conduct fluids through itself. Historically, the concept of permeability is directly connected to porosity (Bear, 1972). Analogous to primary and secondary porosity, two types of permeability can be distinguished: (1) primary permeability and (2) secondary permeability (Gerhart, 1984; Nelson & Handin, 1977; Westerman, 1981). Primary permeability is directly related to primary porosity and the formation of the rock by sedimentation, compaction, crystal growth, or diagenetic processes. It is mainly formed by interconnected pores in the rock and is therefore closely related to the effective porosity. In contrast, secondary permeability is created by processes that occur after the formation of the rock (Nelson & Handin, 1977). Such processes include weathering of superficial rocks, dissolution of minerals (e.g., karstification), or faulting and fracturing. These processes can change the flow conditions in the rock drastically and increase the permeability by several orders of magnitude (Figure 1.1).

Consequently, secondary permeability structures govern the fluid flow in most of the consolidated rocks (Westerman, 1981). Due to the particular prerequisites for karstification (i.e., presence of water-soluble minerals) or weathering (i.e., shallowness of the geological formation), fractures and faults are prevalently the major pathways in most parts of the deep geological subsurface. Thus, many geoscientific applications rely on the knowledge and control of flow processes in fractured rocks (Viswanathan et al., 2022). For instance, applications, such as geothermal energy production (e.g., Zhang & Zhao, 2020) or hydrocarbon extraction (e.g., Aydin, 2000), are based on well-connected fracture networks in the respective reservoir formation and on the high permeability of each individual fracture to establish profitable fluid flow rates. In contrast, applications, such as nuclear waste disposal (e.g., Bossart et al., 2017) and carbon capture and storage (CCS) (e.g., Bond et al., 2017), depend on the absence or low permeability of fractures to prevent fluid migration. Regardless of the actual geoscientific application, a profound understanding of the governing processes affecting fracture permeability on multiple scales is indispensable for the application's success.

Due to the ongoing global climate change and the resulting energy transition, the expansion and further development of some of the previously mentioned applications have become increasingly relevant in recent years. In Germany, for instance, the 8th Energy Research Program of the German government particularly highlights the safe storage of hydrogen and the further development of geothermal energy as future priorities (BMWK, 2023). The latter includes both the general expansion of shallow and deep hydrothermal and closed-loop systems, as well as the development of unconventional systems, such as enhanced geothermal systems (EGS), in which artificially created fractures ("hydraulic fracturing") or existing fractures in fault zones are exploited as major pathways for fluid migration. However, in the last decades, several EGS projects failed in Germany and its surrounding states due to a lack of permeability in the subsurface (Gaucher et al., 2015). The latter can lead to an increase in hydraulic pressure, a reduction in effective stress, and an induction of shearing reactivation on fault zones and fractures, manifesting as induced seismic events, as demonstrated by projects in Landau in 2009 (Grünthal, 2014), Basel in 2006 (Deichmann & Giardini, 2009), or Strasbourg in 2019/2020 (Schmittbuhl et al., 2022). It thus becomes apparent that a hydraulic investigation of fracture permeability in such systems is indispensable, but also not sufficient, since a mechanical consideration of normal loading and shear processes is additionally required.

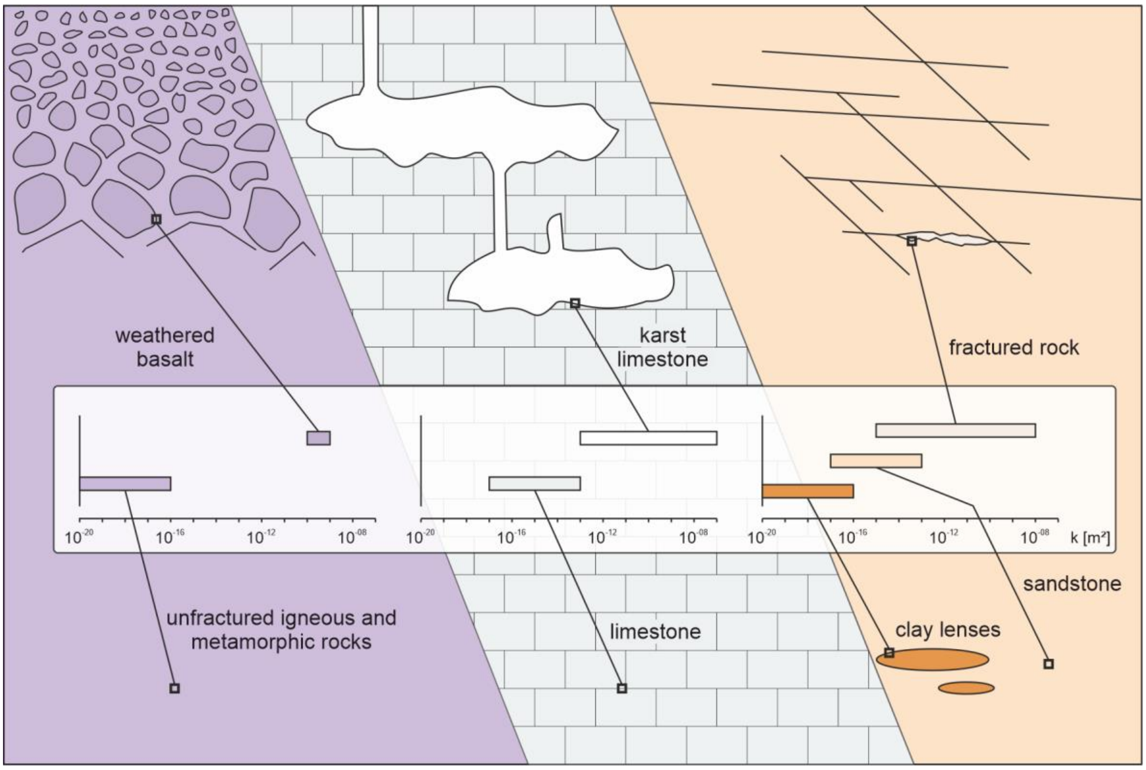

Figure 1.1: Representative permeability ranges for different rocks with primary permeability (bottom) and with typical secondary permeability structures (top). The permeability ranges are taken from Freeze & Cherry (1979) and Ingebritsen & Manning (2011).

Thus, this thesis depicts both novel methods for hydraulic permeability estimation of single fractures and investigations on the influence of normal and shear stress on the fracture permeability. The individual objectives of this thesis are highlighted in Chapter 1.3, with the structure of this thesis being provided in Chapter 1.4. However, first, an introduction is given to the general procedure of hydro-mechanical (HM) permeability characterization of single fractures (Chapter 1.2).

1.2 Permeability characterization of single fractures

The characterization of permeability in single fractures is a multi-step process. The fundamental principles underlying this process will be addressed in the following chapter. First, the various parameters used to describe permeability or hydraulic conductivity in a single fracture will be classified (Chapter 1.2.1). Subsequently, the workflow for determining permeability will be outlined.

1.2.1 Parameters of permeability measurement

Historically, the flow of fluids through geological media has been described using Darcy's law, which represents a specific solution of the Navier-Stokes equations (Bear, 1972).

$$Q = K \cdot A \cdot \frac{\Delta h}{L} \tag{1.1}$$

In Darcy's law, Q is the volumetric flow rate [m³/s], K is the hydraulic conductivity [m/s], A is the cross-sectional area of the flow domain [m²], Δh is the difference of hydraulic heads between the inlet and outlet [m], and L is the length of the flow domain [m].

In porous media, this is a useful concept, since the flow rate, the cross-sectional area of the flow domain, and the hydraulic gradient can be well determined experimentally. Consequently, hydraulic conductivity can be used as a measure of the material's ability to be permeated by water at room temperature. However, the hydraulic conductivity depends on the density and viscosity of the fluid as well as the acceleration of gravity. Thus, hydraulic conductivity is not a material property of the permeated medium, but exhibits significant variation in response to changes in fluid properties and spatial location. Especially in applications involving deep subsurface environments (e.g., geothermal brines) or fluids other than water (e.g., oil, gas, NAPL), this concept becomes inadequate. Thus, the concept of permeability was introduced as an intrinsic material property that is independent of the fluid properties and the location (Bear, 1972):

$$k = \frac{\mu}{\rho g} K \tag{1.2}$$

Here, the permeability is described by k [m²], whereas K is the hydraulic conductivity [m/s]. μ is the dynamic viscosity of the fluid [Pa·s], ρ the fluid density [kg/m³], and g is the acceleration of gravity [m/s²].

Although the concepts of hydraulic conductivity and permeability are primarily applicable to porous media, they have also been applied to fractures (Lomize, 1951; Louis, 1969). However, in the presence of rock fractures, the characterization of fluid flow becomes significantly more complex and cannot be described as straightforwardly as in porous media (Louis, 1969). In fact, the permeability of individual fractures must first be characterized in order to subsequently estimate the overall permeability of the fractured rock. To achieve this, it is essential to understand the hydraulic processes occurring within a single fracture. Since a fracture consists of two morphologically complex surfaces and therefore cannot be compared to a porous medium, the following challenges arise:

- **Fracture aperture:** The variable aperture between the two fracture surfaces, caused by asperities, makes accurate determination of the effective flow cross-section highly challenging.
- **Turbulent flow:** Due to the significantly higher porosity, substantially higher flow velocities can occur, potentially leading to turbulent flow effects within the fracture. Since the application of Darcy's law assumes laminar flow conditions, the flow velocity must be analyzed accordingly using the Reynolds number.

Thus, the principle of describing fluid flow through fractured rocks was only established in the 1950s - 1970s (Lomize, 1951; Louis, 1969; Witherspoon et al., 1980). In this context, the fractures were also regarded as a porous medium, and Darcy's law was applied. Based on experimental investigations and theoretical considerations, a model was developed that generalized Darcy's law to account for fluid flow through a single fracture as a function of its aperture:

$$\frac{Q}{\Delta h} = \frac{W}{L}\frac{\rho g}{12\mu}a^3 \qquad (1.3)$$

Here, Q is the flow rate [m³/s], Δh is the difference of hydraulic heads between the inlet and the outlet of the fracture [m], W and L are the width and the length of the fracture, respectively. ρ is the density of the fluid [kg/m³] and μ is its dynamic viscosity [Pa·s], g is the acceleration of gravity [m/s²], and a is the aperture of the fracture.

Equation 1.3 is widely referred to as the "cubic law" for flow in fractures, as the flow rate is proportional to the cube of the fracture aperture. Consequently, the hydraulic conductivity can be expressed as a function of the aperture (Witherspoon et al., 1980):

$$K = \frac{\rho g a^2}{12\mu} \qquad (1.4)$$

While the first studies proposing the cubic law mainly used K as the parameter to describe the fracture's conductivity (Lomize, 1951; Louis, 1969), the predominant application of the cubic law in the field of oil and gas extraction led to the use of the permeability as the standard parameter describing the conductivity of a fracture:

$$k = \frac{a^2}{12} \qquad (1.5)$$

To determine the fracture aperture, it was assumed that the fracture consists of two parallel plates. The parameter a serves as the equivalent aperture representing the perpendicular distance between these two hypothetical plates.

To better distinguish between different types of apertures, a distinction was first introduced in the 1980s (Barton, 1982). The mechanical aperture a_m refers to the directly measurable distance between two fracture surfaces. It is typically measured perpendicular to a reference plane that averages the geometry of each fracture surface (Hakami & Larsson, 1996; Vogler et al., 2018).

Due to the morphological characteristics of the fracture (e.g., contact area, constrictions impeding fluid flow), the flow does not strictly follow the geometry of the fracture. Therefore, a purely mechanical description of the fracture aperture is insufficient. To address this, the hypothetical hydraulic aperture a_h was introduced for the equivalent aperture in the parallel plate model discussed above (Barton, 1982; Vogler et al., 2018). In its original sense, a_h represents a global parameter that is valid for the entire fracture domain (Figure 1.2).

Consequently, it is not possible to characterize zones of high or low permeability within the fracture using the cubic law (Oron & Berkowitz, 1998). Thus, numerous studies have aimed to further develop the cubic law (e.g., Brown, 1987; Iwai, 1976; Moreno et al., 1988). The local cubic law (LCL) accounts for heterogeneities in aperture and permeability within a fracture (Oron & Berkowitz, 1998). The assumption of a parallel plate model is not applied to the entire fracture, but rather to a small representative segment. In this way, the hypothetical hydraulic aperture can be related to the actual mechanical aperture. Additionally, the pressure gradient can be reduced from a global to a local scale. If the segment is chosen sufficiently small, the roughness of the fracture surfaces can be realistically represented using the LCL.

In current practice, two parameters are commonly used to describe flow through a fracture: on one hand, the hydraulic aperture, and on the other, the permeability of the fracture. Both parameters can be applied either globally (using the cubic law) or locally (using the LCL). It should be noted that in this study, both parameters are used to determine hydraulic conductivity. These three parameters can be converted into one another using Equations 1.4 and 1.5.

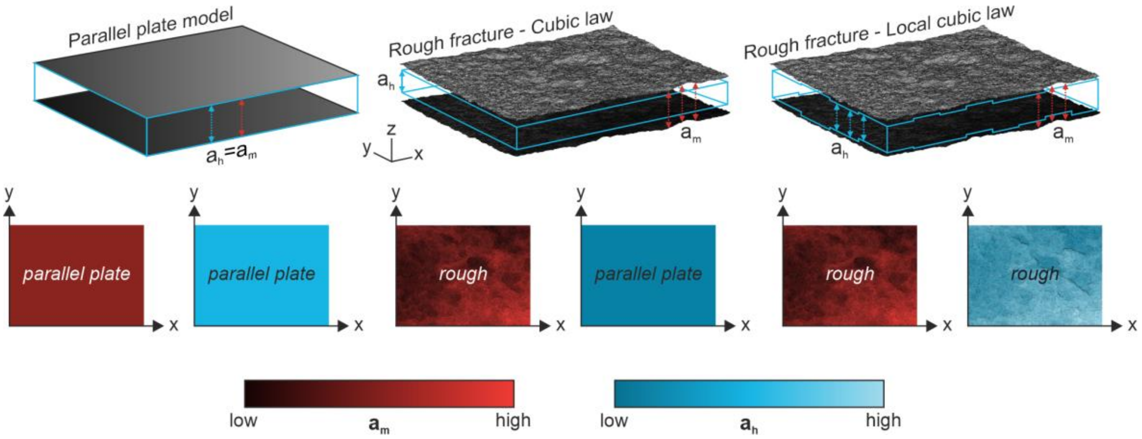

Figure 1.2: Mechanical aperture a_m (colored in red) and hydraulic aperture a_h (colored in blue) for the parallel plate model, the cubic law applied on a rough fracture, and the local cubic law of a rough fracture (modified after Hale, 2022).

1.2.2 Permeability characterization methods

Characterizing the permeability of subsurface fractures is one of the most critical challenges that remains a non-trivial and diverse task (Viswanathan et al., 2022). Thus, a wide range of methodological approaches can be employed. These approaches can be broadly categorized into four groups: (1) experimental investigations, which involve direct or indirect measurements of the permeability under controlled laboratory or field conditions; (2) numerical simulations, which compute fluid flow within fractured media representing the fracture digitally; (3) empirical models, which estimate permeability based on observed correlations and statistical relationships; and (4) geometric analyses, which infer permeability characteristics from the structural and morphological attributes of the fracture.

Historically, the standard method for determining fracture permeability has been experimental measurements (Bear, 1972). For this purpose, the fracture is mounted within a permeameter test, which is a specialized configuration of a flow-through experiment. During the experiment, the sample is subjected to water flow under steady-state conditions. Under a fixed difference of hydraulic heads, the volumetric fluid flow rate is measured, and the permeability can be subsequently calculated using Darcy’s law. A similar method is the use of gas-driven permeameters, such as the Hassler cell (Thomas & Ward, 1972). In these systems, the fracture is not permeated by water but by gas (i.e., air) under steady-state conditions (Filomena et al., 2014). Depending on the application, both water-driven and gas-driven permeameters have their respective advantages:

- **Water-driven permeameters:** Water interacts with minerals present in the sample. This can result in the dissolution or precipitation of minerals (e.g., calcite, dolomite), the swelling of minerals (e.g., clay minerals, anhydrite), or the adsorption of water molecules onto clay mineral surfaces (Filomena et al., 2014). All of these processes alter the effective flow volume of the fracture and, consequently, its permeability (Hale et al., 2022; Kling et al., 2017). However, for applications in the field of groundwater (e.g., geothermal energy, tunnel construction), water more accurately represents real-world conditions than gas.

- **Gas-driven permeameters:** Gas generally does not affect or contaminate the sample and therefore does not affect permeability (Filomena et al., 2014). As a result, gas is particularly well-suited for representing conditions relevant to applications in the oil and gas industry.

An advantage of gas permeameters is that, in the last decades, portable gas permeameters, also known as minipermeameters or probe permeameters, have been developed (Davis et al., 1994; Eijpe & Weber, 1971; Hurst & Goggin, 1995). These systems inject or abstract gas (i.e., air, nitrogen) from the sample and measure the corresponding pressure response under steady-state or transient conditions (Brown & Smith, 2013; Chandler et al., 1989; Davis et al., 1994). Due to their mobility and low costs, these devices enable rapid and efficient measurements both in the laboratory and in the field (Filomena et al., 2014).

Minipermeameters have become the standard method for field measurements, as other measurement techniques are often complex and expensive to implement (Hale et al., 2021). While transmissivity measurements of fractured zones in boreholes are conducted within rock laboratories such as Mont Terri (e.g., Bossart et al., 2004) or BedrettoLab (e.g., Bröker et al., 2024), these only allow for an estimation of single-fracture permeability. Real *in situ* experiments aimed at determining the permeability of individual single fractures remain rare (Novakowski & Lapcevic, 1994; Rutqvist, 2015; Sidle et al., 1998).

A recurring insight from experimental studies is the high cost and effort involved in conducting them. Due to increasing computational capacity, the determination of single-fracture permeability through numerical modeling has become increasingly popular.

In numerical simulations, the fracture is either represented as a two-dimensional plane, with each mesh element assigned a permeability value derived from the mechanical aperture, allowing the application of LCL and Darcy's law (e.g., Javanmard et al., 2021; Stoll et al., 2019). This approach allows a fast estimation of the fracture's hydraulic aperture. However, it ignores the correct representation of the three-dimensional geometry as well as turbulent flow effects. Considering these effects, the fracture can be modeled in three dimensions, and the Navier–Stokes equations are numerically approximated (e.g., Blöcher et al., 2019; Egert et al., 2021). This approach provides more accurate results but requires significantly more computational power and time (Egert et al., 2021). Previous studies have shown that for low Reynolds numbers, permeability can still be adequately estimated using Darcy's law (Egert et al., 2021).

However, it is generally accepted that Darcy’s law tends to overestimate permeability by up to 19 % compared to solutions based on the Navier-Stokes equations (Egert et al., 2021).

The major advantage of numerical modeling lies in its flexibility. It allows the versatile coupling of hydraulic, thermal, mechanical, and chemical processes (Tsang, 1991, 2024; Viswanathan et al., 2022). More importantly, unlike most experimental investigations, numerical modeling is always non-destructive, enabling the repetition of simulations under varying conditions. However, to obtain meaningful results, natural fracture surfaces must first be imaged and subsequently digitally reassembled. Since this process is non-trivial, yet particularly relevant to this thesis, it is described in detail in Section 1.2.3.

In general, numerical simulations and experimental investigations show that permeability depends mainly on the geometrical characteristics of a fracture, particularly on the roughness of the fracture surfaces. Based on this insight, many authors have attempted to develop empirical or statistical models to describe fracture permeability. These are often based on extending the Cubic Law by incorporating geometric and mechanical properties of a fracture (Hale et al., 2020; Kling et al., 2017). Consequently, it is possible to determine permeability without hydraulic measurements or simulations. Widely used parameters include the mechanical aperture (e.g., Louis, 1969; Witherspoon et al., 1980), the relative roughness of the fracture (i.e., standard deviation of the mechanical aperture distribution) (e.g., Barton & De Quadros, 1997; Brown, 1987; Kling et al., 2017), the Joint Roughness Coefficient (JRC) of the fracture surfaces (e.g., Barton, 1982; Olsson & Barton, 2001), the fractal dimension (e.g., Brown, 1987; Patir & Cheng, 1978), as well as the contact area (e.g., Zimmerman & Bodvarsson, 1996). A comprehensive overview of the various empirical models is provided in Kling et al. (2017) and Cardona et al. (2021).

Although these models enable the estimation of the hydraulic aperture of a fracture based on mechanical properties, they are often calibrated only for a limited range of roughness, apertures, or lithologies (Kling et al., 2017). As a result, they do not yield reliable predictions outside of these specific conditions. Moreover, the application of different equations or models can lead to significantly divergent permeability values (Hale et al., 2020). Thus, for an accurate scientific determination of permeability, an investigation using alternative methods (e.g., experiments, numerical simulation) is indispensable.

Recognizing the dependence of fracture permeability on geometric properties enables the use of a fourth category of approaches, the geometric approaches. These methods derive permeability through mathematical analysis of topological and morphological information. An early example is the Kozeny-Carman equation, which allows for the estimation of permeability based on the pore geometry of a porous medium (Carman, 1937; Kozeny, 1927). In recent decades, numerous studies have focused on determining permeability from pore structure in fracture images

(Costa, 2006; Oliveira et al., 2020; Torskaya et al., 2014), particularly in recent years with the support of artificial intelligence (e.g., Da Wang et al., 2021; Sudakov et al., 2019).

A specific yet promising method in this context is topological data analysis (TDA). TDA examines the topology of complex data and can extract information about their connectivity (Carlsson, 2009; Thiele et al., 2016). In geosciences, the method of persistent homology (PH) is particularly employed, as it enables the detection of changes and continuity in topological features (Edelsbrunner et al., 2000; Zomorodian & Carlsson, 2005). For permeability estimation, it is especially relevant that PH can link topological information to actual geometric characteristics of a fracture. In recent years, PH has been increasingly applied to porous media (Bizhani & Haeri Ardakani, 2021; Delgado-Friedrichs et al., 2014; Robins et al., 2016) and fracture networks (Suzuki et al., 2020, 2021). Since it shows comparable results to experimental or numerical approaches in these previous studies, PH is also applied to rough single fractures in this thesis.

1.2.3 Fracture imaging methods

As described in the previous chapter, various approaches for determining the permeability of single fractures require high-resolution imaging of the fracture geometry. Alongside numerical and geometric approaches that directly rely on a digital model of the fracture (Javanmard et al., 2021; Vogler et al., 2018), they are also relevant for related processes, such as the accurate characterization of the fracture surface roughness (Tatone & Grasselli, 2012). A particular relevance arises in applications involving coupled thermal, hydraulic, mechanical, and chemical (THMC) processes in fractures, as fracture imaging allows capturing system changes such as mineral dissolution or precipitation, and mechanical deformation of asperities (Viswanathan et al., 2022).

Since THMC processes in fractures span a wide range of scales, the requirements for fracture imaging methods are diverse. While processes at the millimeter scale may be negligible in large fault zones, many laboratory experiments require resolutions at the micrometer scale (Candela et al., 2012). Consequently, the quality of a scan is always a trade-off between the size of the system and the desired resolution and accuracy (Tatone & Grasselli, 2012). This makes the application of quality metrics indispensable. A common metric is the Accuracy-Resolution Ratio (ARR), which is defined as follows (Tatone & Grasselli, 2012):

$$ARR = \frac{Accuracy}{Resolution} \tag{1.6}$$

The involved parameters are defined as follows:

- **Accuracy:** The average spatial deviation between a measured point and the corresponding actual location of this point. The accuracy reflects the measurement error.

- **Resolution:** The distinguishable distance between two points. The resolution reflects the level of detail captured in a scan.

The ARR threshold is proposed to be ≤ 5 % to receive an accurate representation of fracture and fracture surfaces, respectively (Tatone & Grasselli, 2012). Thus, three categories of imaging methods have emerged in geoscientific research meeting both the required ARR criteria as well as the necessary flexibility: (1) laser scanning, (2) photogrammetry, and (3) computed tomography (CT) scanning.

Laser scanning is one of the most commonly used methods. Its origins date back to the 1990s, when surfaces were imaged using closely spaced 2D laser profiles (Brown, 1995; Huang et al., 1992; Kulatilake et al., 1995). In the early 2000s, 3D laser scanners replaced 2D laser profilometers (Chae et al., 2004; Fardin, 2008; Lanaro, 2000). Nowadays, two types of laser scanners have to be distinguished. For large-scale applications, terrestrial laser scanners are used, where a laser beam is directed at a target and a sensor measures the reflection (e.g., time-of-flight systems, phase-shift systems). However, for the high precision needed to scan single fracture surfaces, these systems lack sufficient resolution and accuracy. For high-precision measurements, triangulation laser scanning is therefore employed. In this method, a laser projects a pattern (i.e., points, lines) onto the fracture surface. The pattern is then captured by a separate camera, and the 3D coordinates of the laser pattern are triangulated (similar to the principle used in photogrammetry).

Laser scanners can offer high resolution (< 100 µm) and accuracy (< 10 µm). Additionally, modern laser scanners are capable of performing further processing steps, such as meshing, directly from the scanned point cloud, making them a time-efficient tool for most applications. However, their main disadvantage lies in the high cost associated with the equipment.

The principle of most photogrammetric methods works similarly to the principle applied in laser triangulation. In the widely used photogrammetric method of structured light scanning, visible light patterns are projected on a fracture surface instead of laser patterns, which are then captured by separate cameras (Grasselli et al., 2002; Kling et al., 2017; Tatone & Grasselli, 2012; Vogler et al., 2018). Subsequently, a point cloud of the fracture surface is triangulated using the overlapping patterns observed in multiple images (Grasselli et al., 2002). The accuracy of this approach is comparable to laser triangulation, reaching values < 50 µm, and under optimal conditions, even < 10 µm. (Grasselli et al., 2002; Vogler et al., 2016). Furthermore, portable devices are used for structured light scanning, enabling the use in the field, although similar to laser triangulation, optimal conditions can only be reached in a laboratory environment (Tatone & Grasselli, 2012).

Thus, for a more flexible handling, the photogrammetric Structure from Motion (SfM) method has emerged (Marsch et al., 2020; Zambrano et al., 2019). SfM operates entirely without the projection of light patterns. The generation of a point cloud is achieved solely through the reconstruction of overlapping images of the fracture surface taken from different angles. This enables the creation of high-resolution point clouds using only a digital camera, which significantly facilitates field applications. The accuracy strongly depends on the specific conditions of the setting, such as lighting, number of images, and viewing angles, but can reach down to 35 µm under optimal conditions (Marsch et al., 2020).

Although both laser scanning and photogrammetry are widely used to image fracture surfaces, they share a fundamental conceptual limitation: to obtain a 3D point cloud of a fracture, both surfaces must be scanned separately and then digitally re-matched (Grasselli et al., 2002; Vogler et al., 2018). This inevitably introduces matching errors when the surfaces are merged to reconstruct the fracture.

An alternative to avoid matching errors is the use of high-resolution CT scanning, such as µ-CT scanning, synchrotron-based CT scanning, or medical CT scanning (Crandall et al., 2010; Karpyn et al., 2007; Kling et al., 2016; Ruf & Steeb, 2020). In contrast to other methods, CT scanning relies on differences in material properties (i.e., air-rock or water-rock), enabling the *in situ* fracture imaging of a non-seperated sample (Kling et al., 2016). Furthermore, geometrical changes of fractures during THMC experiments can directly be imaged by CT scanners (Renard et al., 2009, 2020). The resolution of < 50 µm and the accuracy of < 10 µm under optimal conditions are comparable to other approaches (Lee et al., 2022). However, in order to achieve such high resolutions and accuracy, the sample size must be correspondingly small (less than a few centimeters), which makes it ideal for detailed observation of THMC processes in (micro-)fractures, but limits its applicability in scenarios requiring larger-scale representativity (Lee et al., 2022; Renard et al., 2020; Ruf & Steeb, 2020).

1.2.4 Coupling with mechanical processes

THMC processes are widely known to affect the permeability of single fractures (Viswanathan et al., 2022). Although all THMC processes can influence fracture permeability, mechanical processes are the most common and often have a massive impact. In general, mechanical processes can be divided by the direction they affect the fracture surface (Cardona et al., 2021):

- **Normal loading:** Normal loading acts perpendicular to the fracture surface, resulting in the closure of the mechanical aperture (Cardona et al., 2021). Consequently, normal closure of a fracture increases the contact area and the stiffness of the fracture, which counteracts the normal stress (Nemoto et al., 2009). To predict fracture closure, various contact models can be applied to compute deformation of the fracture using different approaches, such as the Hertzian/Greenwood-Williamson contact model (Greenwood & Williamson, 1966), the Hopkins method (Hopkins et al., 1987), interpenetration approaches (Watanabe et al., 2008), or fast Fourier transform-based convolution methods (e.g., Kling et al., 2018).

- **Shear displacement**: Shear displacement results from a complex deformation that can be decomposed into a normal stress component perpendicular to the fracture surface and a shear component parallel to it (Cardona et al., 2021; Fang & Wu, 2022). The resulting shear behavior is always a compromise between dilation at asperities, potential overriding of asperities, stress buildup at asperities, and their subsequent failure (Gutierrez et al., 2000). Consequently, multiple interrelated factors influence the evolution of a fracture during shearing (Cardona et al., 2021). Thus, shear displacement includes the following sub-processes:
    - **Contact area evolution:** The contact area evolution is crucial during the shearing of fractures. Shear and normal stresses inevitably generate contact areas at the asperities of the fracture surfaces. Depending on the magnitude of the stress, this results in dilation at the asperities, or their failure or deformation. The development of the contact area is primarily dependent on the initial state of the fracture. In perfectly mated fractures (e.g., induced fractures), shearing reduces the contact area, whereas in unmated fractures (e.g., natural fractures), it leads to an increase (Cardona et al., 2021). Hydraulically, contact area closes potential flow paths and can therefore reduce the fracture's permeability.
    - **Dilaton:** Dilation refers to the sliding of one fracture surface over the asperities of the opposing surface (Esaki et al., 1999; Wenning et al., 2019). Thus, it leads to an increase in the mechanical aperture and an enlargement of potential flow paths (Ishibashi et al., 2018). Significant dilation typically occurs under low stress conditions or in rocks with high stiffness (Fang & Wu, 2022).
    - **Asperity degradation:** Asperity degradation occurs particularly under high shear rates and high normal stress conditions, when stress accumulates at contact points (Liu et al., 2016). Thus, microcracks form within the asperities, leading to asperity deformation (Liu et al., 2016). Continued asperity degradation results in asperity failure, the mechanical closing of a fracture, and the formation of gouge material (Asadi et al., 2012).
    - **Gouge formation:** Gouge material is generated either through asperity degradation or by the "carving" of one fracture surface by the asperities of the opposing surface (Asadi et al., 2012). This is primarily caused by high pressures or low-strength material (Fang & Wu, 2022; Li et al., 2023; Liu et al., 2016). Consequently, the released gouge can close the fracture and clog potential flow paths, resulting in a reduction of the fracture's permeability (Welch et al., 2022).

1.3 Objectives

The objective of this thesis is to improve the understanding of hydro-mechanical (HM) processes in a natural single fracture of Flechtinger sandstone, a former oil and gas reservoir rock considered now for deep geothermal energy applications. The focus is in particular on the development of novel methods to accelerate the permeability estimation in natural single fractures and on the implementation of novel numerical approaches enabling the detailed investigation of HM processes in numerical models.

In this context, this thesis aims to:

- compare and evaluate various fracture surface imaging approaches as an essential but often underexposed part of the process of characterizing the permeability of fractures.
  To evaluate different imaging methods, three modern imaging methods were applied to a bedding joint in a sandstone block, and the resulting three-dimensional point clouds were used as a basis for numerical flow simulations.

- transfer the topological persistent homology method from fracture networks and porous media to single fractures and evaluate its applicability for permeability estimation compared to conventional experimental and numerical methods.

- investigate the impact of increasing normal stress and shear displacement on the permeability evolution and gouge formation of a single fracture.
  A novel combination of a three-dimensional discrete element method (DEM) model used to represent the mechanical deformation of the fracture and a finite element method (FEM) model to simulate the hydraulic flow through the single fracture is used. Particular focus was also placed on the formation and influence of gouge material and contact area.

This thesis addresses the entire workflow of determining the permeability of single fractures. The same bedding joint sample in a sandstone block of Flechtinger sandstone originating from a quarry in Bebertal, Germany, is used for all studies. For better understanding, Figure 1.3 shows a graphical overview of the process of permeability determination and contextualizes studies compiled in this thesis.

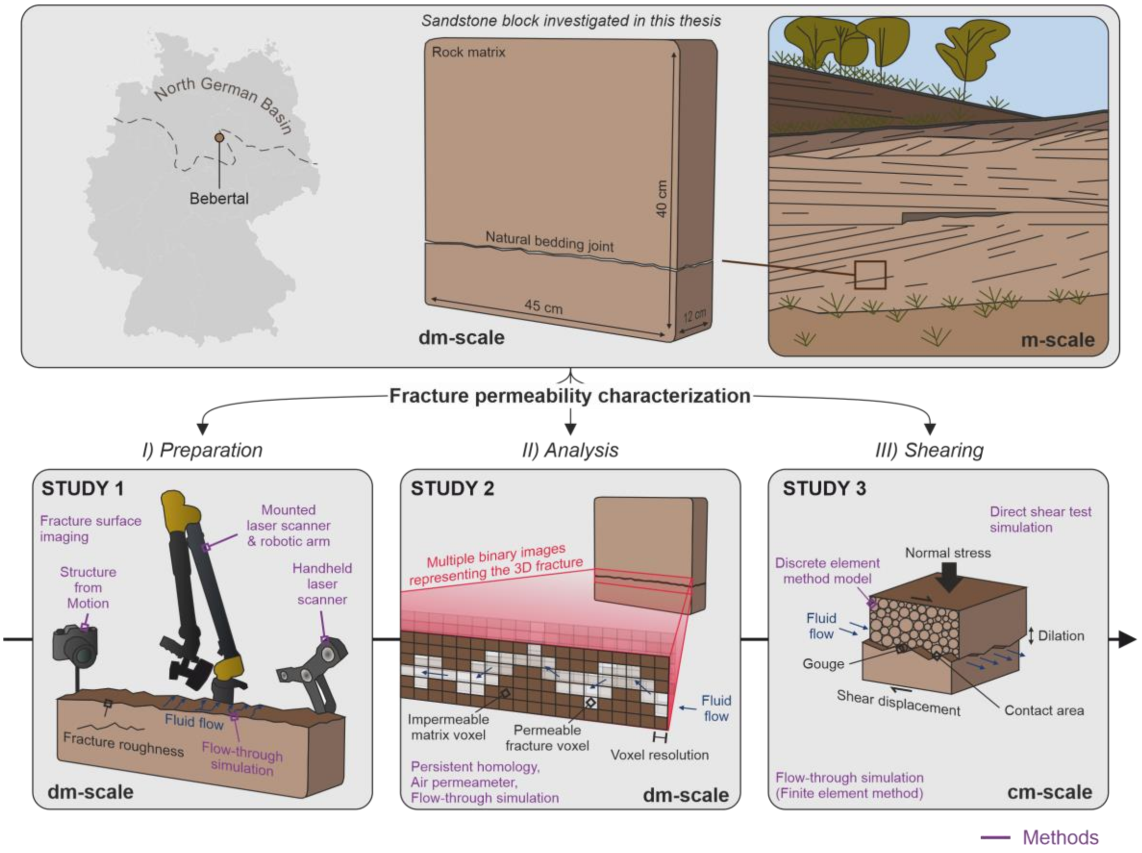

Figure 1.3: Graphical overview of the studies of this thesis and the applied methodology. The entire process of sample preparation (Study 1), permeability determination analysis (Study 2), and the evolution of permeability under shearing conditions (Study 3) is addressed by this thesis within the context of fracture permeability characterization.

1.4 Structure of the thesis

This cumulative thesis presents three individual studies, which are enclosed in Chapters 2 – 4. All studies were submitted to peer-reviewed international journals. Studies 1 and 2, presented in Chapters 2 and 3, are already published, while Study 3 in Chapter 4 is currently under review. The thesis is structured according to the objectives outlined above:

- **Chapter 2:** *“Evaluating fracture surface imaging methods using flow simulations and air permeameter measurements”*, published in *Rock Mechanics and Rock Engineering*
  This chapter aims to evaluate fracture surface imaging methods for their use in numerical flow simulations. Thus, a handheld laser scanner, a combined system of a mounted laser scanner and a robotic arm, and the photogrammetric Structure from Motion method are applied to scan the surfaces of a natural single fracture in a reservoir rock (Flechtinger sandstone). Furthermore, an algorithm is developed to match the two scanned fracture surfaces to subsequently use them in two-dimensional fluid flow simu-

lations. The resulting permeabilities as well as flow distributions are discussed and validated using experimental air permeameter measurements of the fracture.

- **Chapter 3:** *"Investigating rough single-fracture permeabilities with persistent homology"*, published in *Solid Earth*
  In this chapter, the topological persistent homology (PH) method is applied to fracture scans generated by the mounted laser scanner system described in Study 1 (Chapter 2). PH has already been used to characterize the permeability of small-scale fracture networks and porous media. Here, it is transferred to natural single fractures. Thus, three distinct datasets of the same fracture, each with a different resolution, are created to investigate the dependency of resolution on the permeability estimation using PH. The findings are then validated using air permeameter measurements and numerical flow simulations. In addition, an evaluation of the PH method was conducted with respect to the expenditure of time, in comparison to the other conventional approaches.

- **Chapter 4:** *"Permeability evolution and gouge formation during fracture shearing"*, published in *Geophysical Research Letters*
  This chapter investigates the evolution of the previously used natural single fracture during shearing with respect to changes in normal stress. As part of the study, a novel approach was developed that combines mechanical direct shear test simulations using the discrete element method (DEM) with subsequent hydraulic flow simulation using the finite element method (FEM). Consequently, multiple coupled simulations were conducted under six different normal stress scenarios to identify changes in permeability and determine influencing factors. Particular focus was placed on dilation at asperities, the development of contact area, and the formation of gouge material. In conclusion, the conditions for fracture opening or closure are discussed, and generalized threshold values are identified, enabling the transferability of the results to other fractures.

- **Chapter 5:** *Synthesis*
  In this chapter, the findings of Studies 1 – 3 (Chapters 2 – 4) are summarized, and conclusions about their improvement for permeability characterization of natural single fractures are derived. Finally, an outlook on pending research questions is provided.

2 Evaluating fracture surface imaging methods using flow simulations and air permeameter measurements

Reproduced from: Fuchs, M., Hale, S., Blesch, L., Rau, G. C., Menberg, K., Blum, P. (2024): Evaluating Fracture Surface Imaging Methods Using Flow Simulations and Air Permeameter Measurements. Rock Mechanics and Rock Engineering 57, 1849–1860, https://doi.org/10.1007/s00603-023-03615-6

Abstract

Knowledge of fracture properties and associated flow processes is important for geoscience applications such as nuclear waste disposal, geothermal energy and hydrocarbons. An important tool established in recent years are hydro-mechanical models which provide a useful alternative to experimental methods determining single fracture parameters such as hydraulic aperture. A crucial issue for meaningful numerical modeling is precise imaging of the fracture surfaces to capture geometrical information. Hence, we apply and compare three distinct fracture surface imaging methods: (1) handheld laser scanner (HLS), (2) mounted laser scanner (MLS) and (3) Structure from Motion (SfM) to a bedding plane fracture of sandstone. The imaging reveals that the resolution of the fracture surface obtained from handheld laser scanner (HLS) is insufficient for any numerical simulations, which was therefore rejected. The remaining surfaces are subsequently matched and the resulting fracture dataset is used for detailed fracture flow simulations. The resulting hydraulic aperture is calibrated with laboratory measurements using a handheld air permeameter. The air permeameter data provide a hydraulic aperture of 81 ± 1 µm. For calibration, mechanical aperture fields are calculated using stepwise increasing contact areas up to 15 %. At 5 % contact area, the average hydraulic aperture obtained by MLS (85 µm) is close to the measurement. For SfM, the measurements are fitted at 7 % contact area (83 µm). The flow simulations reveal preferential flow through major channels that are structurally and geometrically predefined. Thus, this study illustrates that resolution and accuracy of the imaging device strongly affect the quality of fluid flow simulations and that SfM provides a promising low-cost method for fracture imaging on cores or even outcrops.

2.1 Introduction

Determining fluid flow through natural fractures is an important task in many geoscientific fields such as geothermal energy, nuclear waste disposal, resource mining, or building tunnels (Berkowitz, 2002; Zimmerman & Bodvarsson, 1996). The hydro-mechanical properties of fractured rocks are controlled by the characteristics of fractures rather than by the matrix of the intact rock (Tatone & Grasselli, 2012). This necessitates detailed characterization of the hydraulic and mechanical fracture properties (Kling et al., 2018; Renshaw, 1995).

The aperture of a fracture is used as a representative parameter for its hydro-mechanical properties, mainly the mechanical (a_m) and hydraulic (a_h) aperture. The mechanical aperture is defined as the distance between the two fracture surfaces measured perpendicular to a reference plane averaging both surfaces (Hakami & Larsson, 1996; Vogler et al., 2018). In contrast, the hydraulic aperture considers fluid flow and a pressure gradient across the fracture and is directly related to the permeability of the fracture (Javanmard et al., 2021; Vogler et al., 2018). The determination is often based on the cubic Law which approximates hydraulic fractures by considering the space between two parallel and smooth planes (Louis, 1967; Witherspoon et al., 1980).

Various methods have been established to estimate both mechanical and hydraulic fracture apertures (Renshaw, 1995). Mechanical fractures are mainly determined by distance measurements between two spatially referenced and matched scans of the fracture surfaces (Hakami & Larsson, 1996; Olsson & Barton, 2001; Vogler et al., 2018). Multiple methods for the determination of hydraulic apertures exist: (1) experimental methods such as flow experiments or air permeameter measurements (Cheng et al., 2020; Hale et al., 2020, 2021; Novakowski & Lapcevic, 1994; Riegel et al., 2019; Thörn et al., 2015; Thörn & Fransson, 2015; Weede & Hötzl, 2005), (2) hydraulic numerical simulations (Cardenas et al., 2007; Crandall et al., 2010; Xiong et al., 2011; Zambrano et al., 2019) and (3) derivation by empirical equations based on parameters such as mechanical apertures or roughness (Barton & De Quadros, 1997; Javanmard et al., 2021; Kling et al., 2017; Renshaw, 1995).

Various imaging methods for 3D surface representations have been developed which can be categorized into three major groups based on measurement technique and required equipment: (1) laser scanning (Tatone & Grasselli, 2013), (2) computed tomography (CT) scans (Johns et al., 1993) and (3) photogrammetry (Grasselli et al., 2002). Laser scanning is one of the most popular imaging techniques. Its use started in the 1990’s, when the 3D fracture surface was represented by multiple close-spaced 2D profiles obtained by a laser profilometer (Brown, 1995; Huang et al., 1992; Kulatilake et al., 1995). Despite the advantage of constructing a rough surface, there were several disadvantages such as slow data generation or inaccurate mapping of the surface (Tatone & Grasselli, 2013). In the following decades, laser scanners were developed that could scan surfaces with high resolution and accuracy and were applied for fracture surface scanning (e.g., Candela et al., 2012; Li et al., 2014; Renard et al., 2006; Tatone & Grasselli, 2012, 2013).

In contrast to other methods, laser scanners provide a high resolution and accuracy, but most tools have limited mobility and little flexibility. Since the fracture surfaces are separated for scanning, the scans have to be re-matched afterwards using marker points or computer algorithms, which compromises accuracy. In order to avoid matching errors, high-resolution CT scans such as µ-CT, synchrotron-based CT or medical CT scans, can be used to image fractures (Crandall et al., 2010; Karpyn et al., 2007; Kling et al., 2016, 2018; Ruf & Steeb, 2020). In contrast to laser scanning, the two fracture surfaces are not separated from each other, but a fractured block or core sample is scanned as a whole. In addition, the fracture surface itself is not scanned, but the rock is imaged slice by slice. Due to different material properties of the solid and void phase, these can be segmented in the scan data (Kling et al., 2016). µ-CT scanning was first used for aperture determination by Johns et al. (1993) and has gained popularity especially in the last two decades with respect to its application in fracture flow simulations (e.g., Bertels et al., 2001; Crandall et al., 2010; Karpyn et al., 2007; Kling et al., 2016; Stoll et al., 2019; Zambrano et al., 2018). This is mainly due to the improvement in resolution of the devices, which is now < 50 µm and can compete with other methods such as laser scanning or structured light scanning (Crandall et al., 2010; Karpyn et al., 2007; Ruf & Steeb, 2020). However, the disadvantages of this technique are the time-consuming scanning to obtain a good resolution and the low mobility, as this method that can only be performed stationary (Kling et al., 2016).

The third group of methods is based on digital images. Photogrammetry uses patterns in overlapping images and the principle of triangulation to generate a three-dimensional model of an object. There are proven techniques in the field of fracture surface imaging such as structured light scanners which cast a light pattern onto the surface and use two cameras to record these (Bitenc et al., 2019; Grasselli et al., 2002; Kling et al., 2017; Lianheng et al., 2020; Vogler et al., 2018). Like laser scanners and CT, structured light scanners have to be used in a stationary or mounted state to produce maximum resolution. In order to tackle this issue, the mobile and flexible Structure from Motion (SfM) method was developed and successfully applied for imaging fracture surfaces (Lianheng et al., 2020; Marsch et al., 2020; Zambrano et al., 2019). However, this method has not been compared to other approaches such as laser scanning yet.

Estimating the hydraulic from the mechanical aperture necessitates consideration of flow processes. Numerical simulations have become popular in the last decades due to their cost- and time-effectiveness as well as their wide range of applicability compared to experimental methods (Berre et al., 2019; Bobet et al., 2009; Viswanathan et al., 2022). However, same as with the determination of the mechanical aperture, numerical simulations require an exact representation of the fracture surface geometry as an input (Tatone & Grasselli, 2012).

The aims of this study are therefore to (1) compare the data quality obtained from Structure from Motion fracture surface imaging with two different laser scanners and (2) reconcile the hydraulic aperture from detailed flow simulations with direct measurements from an air permeameter. Our proposed workflow simplifies the fracture imaging procedure, reduces the cost of application, and provides guidance for fracture imaging on cores and outcrops.

2.2 Materials and methods

2.2.1 Rock sample

A block of Flechtinger sandstone from Bebertal, Germany, was investigated in this study (e.g., Hale & Blum, 2022; Heidsiek et al., 2020). The block contains one bedding joint with about 450 mm in length (x-axis) and 120 mm in width (y-axis). The porosity of the Flechtinger Sandstone is around 9 – 11 % and the rock shows a low matrix permeability of 0.1 – 10 mD, which was determined in previous studies (Cheng et al., 2020; Frank et al., 2020; Hassanzadegan et al., 2012; Heidsiek et al., 2020). Other known characteristics are mineralogical and chemical compositions, Young’s and bulk modulus and thermal dependencies of stress and strain behavior (Fischer et al., 2012; Hassanzadegan et al., 2012). Furthermore, fractures in the Flechtinger Sandstone have been previously investigated and values for hydraulic properties such as permeability or transport parameters also exist in the literature (Blöcher et al., 2019; Frank et al., 2020; Hale et al., 2020). Of particular interest are the findings from Hale et al. (2020) and Hale & Blum (2022), who experimentally investigated the hydraulic aperture on the same fracture sample.

2.2.2 Fracture surface imaging and matching methods

We apply and compare three fracture surface imaging methods (Figure 2.1): (1) laser scanning using a handheld device (HLS), (2) laser scanning using a mounted laser scanner (MLS), and (3) Structure from Motion (SfM). A HLS with a specified resolution of 200 µm and a 3D point accuracy of ≤ 500 µm was used (Freestyle3D Objects manufactured by Faro Technologies Inc, 2016). For MLS, a combined system of the handheld scanner Nikon ModelMaker MMDx 100 and an articulated arm on which the scanner is mounted (MCA II, Nikon Metrology, NV) was used. The latter features a specified resolution of 100 µm with an accuracy of 10 µm (Nikon Metrology NV, 2018). The articulated arm provides a single-point accuracy of 28 µm (Nikon Metrology NV, 2010). Both laser scanners use the triangulation method for determining 3D point coordinates of a fracture surface. Importantly, the MLS scans the fracture geometry stripe-by-stripe, whereas the HLS scans an area. All scans result in 3D point clouds with a practical resolution of about 250 µm for the MLS and about 800 µm for the HLS.

The SfM approach is photogrammetric. A 3D model of an object was calculated from overlapping pictures taken by a digital camera using a computer algorithm (James & Robson, 2012). We used the Dense Image Matching (DIM) approach to generate 3D point clouds of the fracture surfaces (Marsch et al., 2020). To spatially reference and correctly scale the constructed point clouds, a portable norm containing eight spheres fixed on a carbon frame was recorded in addition to the fracture surface as spatial reference points (Figure 2.1). This approach is based on the same construction principle and materials as previously discussed by Marsch et al. (2020). The pictures of the fracture and the norm were captured by a single-lens reflex camera (Sony α58, SLTA58) with a 20.1 megapixel Exmor® APS-C CMOS sensor (manufactured by Sony). In addition, the camera was equipped with a lens hood (DÖRR DR-SH-108). All pictures were taken at artificial lighting conditions by spotlights without flash.

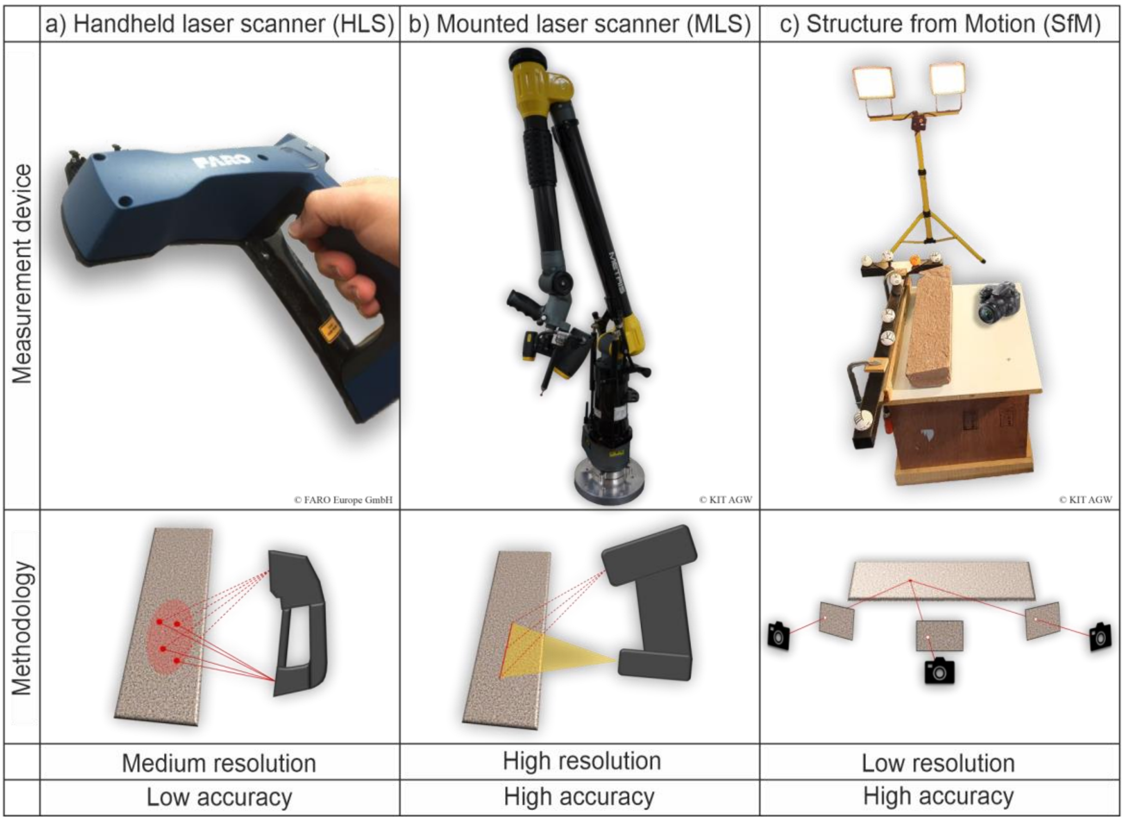

Figure 2.1: Overview of the three imaging methods used in this study to quantify fracture surfaces: a) Handheld laser scanner (HLS), b) mounted laser scanner (MLS), c) Structure from Motion (SfM). For each method, an overview of the methodology, an assessment of the resolution and single-point accuracy are also provided. The image of HLS is modified after Faro (2017).

To generate the 3D point cloud the open-source and free software VisualSFM was used (Wu, 2013; Wu et al., 2011). This applies the SiftGPU algorithm which uses the graphical processing unit (GPU) for 3D image processing (Wu, 2007). The software extracts key points with distinctive pixel patterns from different intersecting pictures estimated that the ideal number of pictures is between 10 and 1000 depending on the size and complexity of the object (James & Robson, 2012). We used 97 pictures to capture each fracture surface. VisualSFM reconstructs the camera position and orientation for each picture to produce a 3D model of the imaged object (Marsch et al., 2020; Wu, 2013). The resulting point cloud is sparse and consists of a few thousands key points (James & Robson, 2012). VisualSFM contains the software CMVS which infers a dense point cloud from the sparse results (Furukawa et al., 2010). Based on a multi-view stereo algorithm (MVS), a large number of points was produced. The final point cloud has an average resolution of about 330 µm, although this varies between 280 and 400 µm across the dataset. The single-point accuracy was not derived in this study, but using a similar experimental setup, Marsch et al. (2020) determined a single-point accuracy of about 35 µm. In addition, the Python code “FracMatch” was developed to convert the 3D fracture surfaces into 2D aperture fields and to create a mesh for the simulation (Figure 2.2). The code allows fracture matching, a process that involves stepwise rotation and translation of the two individual fracture surfaces within specified limits in order to find the best fit that minimizes the average mechanical aperture. This approach is required because each fracture surface can only be imaged separately. After the matching process, a regular 2D grid with a resolution of 400 µm was generated. This resolution represents the realistic resolution of the imaging devices (Kling et al., 2016).

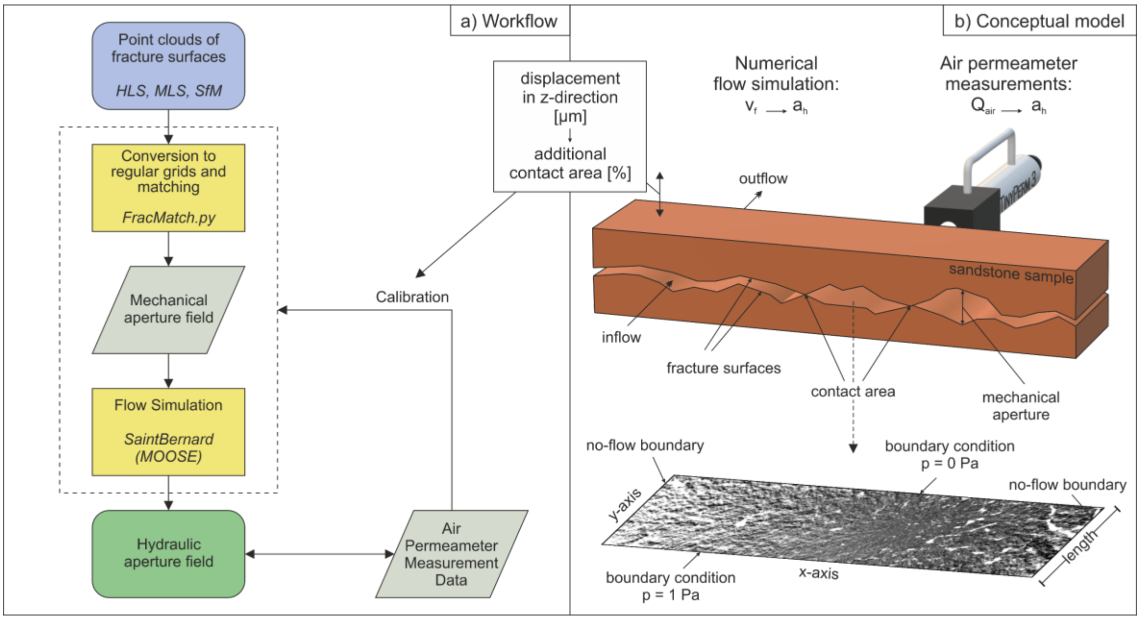

Figure 2.2: a) Workflow and b) conceptual model of the study (not to scale)

2.2.3 Measurement of the fracture permeability

The transient-flow syringe air permeameter TinyPerm 3 (manufactured by New England Research Inc.) was used to measure the permeability of the fracture. This is a portable handheld device, which is able to directly measure rock permeability and hydraulic fracture apertures on outcrops in the field and on cores in the laboratory (e.g., Cheng et al., 2020; Hale et al., 2020, 2021). The device was validated for the determination of hydraulic apertures down to 5 µm by Cheng et al. (2020). The air permeameter can be placed on a fracture, from which it withdraws a defined air volume while monitoring the transient air pressure at the sample outlet and the changing air volume within the syringe (Brown & Smith, 2013). An implemented microcontroller unit then computes a response function. By means of empirical calibration of the air permeameter, the response function is directly related to the permeability of the sample. Further information about the working principle of TinyPerm 3 are given in Brown & Smith (2013) and Hale et al. (2020).

We used measurements from previous work reported in Hale et al. (2020) and Hale & Blum (2022). Before measuring the fracture properties, the sandstone sample had to be reassembled, because it had previously been separated by the fracture. To ensure that the measurements were performed without any artificially induced displacement of the two fracture surfaces, the two separate blocks were fixed by two screw clamps applying pressure to the fracture. The clamping stress is approximately 0.04 MPa (Hale et al., 2020). Since the clamps and the weight of the sample made physical rotation no longer possible, all permeameter measurements were carried out on one accessible edge of the fracture. To obtain a uniform measurement of the entire fracture, the edge was divided into 21 intervals each 17 mm wide corresponding to the air permeameter outlet diameter. The hydraulic aperture of each interval was measured 10 times and the geometric mean was determined as 81 ± 1 µm (Hale et al., 2020).

2.2.4 Fluid flow simulation

Fluid flow through the fracture was simulated to determine the governing hydraulic aperture from the mechanical aperture of the fracture. The numerical simulations were performed using the Multiphysics Object Oriented Simulation Environment (MOOSE) framework, an open-source, parallel finite element software for fully-coupled multi-physics simulations (Permann et al., 2020). To simulate flow and transport through fractures the SaintBernard application developed within MOOSE was applied (Schädle, 2020). It uses the inbuilt PorousFlow module to solve the governing equations for fluid flow (Wilkins et al., 2020, 2021).

SaintBernard is specialized in flow simulations through lower dimensional fractures, which means that the original three-dimensional surfaces are projected on a two-dimensional plane embedded in a three-dimensional environment. This plane is the mechanical aperture field, which has the same spatial extent in x- and y-direction as the original surface and includes the mechanical aperture as z-value. Due to the low matrix permeability of the sample, matrix flow was neglected and it was assumed that all fluid flow occurs through the single fracture.

Before simulation the 2D grid obtained from fracture matching is directly converted into a quadrilateral 2D mesh with the same resolution. The cubic Law is used to estimate permeability from the mechanical aperture. This implies assumptions to simplify the Navier-Stokes equations, i.e. the parallel-plate model (Witherspoon et al., 1980; Zimmerman & Bodvarsson, 1996) and laminar flow through the fracture. The fracture permeability k is expressed as:

$$k = a_h^2/12 \tag{2.1}$$

based on the hydraulic aperture a_h (Cheng et al., 2020; Zimmerman & Bodvarsson, 1996).

The SaintBernard application solves the continuity equation which describes mass conservation for fluid flow (Wilkins et al., 2020). Since this work deals only with the flow of one fluid phase without solutes or change in temperature, we do not require dispersive or diffusive flow, heat flux or chemical transport in the mass conservation equation. In addition, only the flow through a single fracture is considered in this simulation, thus neglecting terms describing mechanical processes or porous rock interaction. This leaves advective fluid flux F governed by Darcy's Law with Darcy velocity v. Furthermore, ρ is the density of the fluid, k_r is the relative permeability and a function of saturation, k is the absolute permeability tensor, p is the pressure and g is the gravitational constant:

$$F^{advective} = \rho v = -\rho(k_r k)/\mu(\nabla p - \rho g) \tag{2.2}$$

The simulation outputs a Darcy velocity for each mesh cell. The hydraulic aperture a_h is determined using this Darcy velocity by combining Darcy's Law and cubic Law as follows:

$$a_h = \sqrt[2]{12 v \mu L/\Delta p} \tag{2.3}$$

Here, v is the Darcy velocity, μ is the dynamic viscosity of the fluid, L is the sample length and Δp is the pressure difference between the inflow and outflow according to Dirichlet boundary conditions (Cheng et al., 2020).

Flow through the fracture was set from bottom to top with the inlet and outlet placed on a long side of the fracture each (Figure 2.2). Dirichlet boundary conditions were applied at the inlet and outlet. Since Darcy flow was assumed for the simulation, the pressure was set to 1 Pa at the inlet and 0 Pa at the outlet. This resulted in a pressure gradient of about 0.09 Pa/cm along the y-axis and avoided turbulent flow effects in the fracture. No flow boundary conditions were assumed at both shorter sides of the fracture.

The flow velocity was then simulated in each cell of the mesh and hydraulic aperture fields of the fracture were calculated. The hydraulic apertures were subsequently determined using Eq. 3, and average values, arithmetic mean and median, were calculated from individual values across the fracture surface.

In order to align the simulated hydraulic aperture with the air permeameter measurements (Hale et al., 2020), a calibration of the hydraulic aperture using the air permeameter measurements was performed (Figure 2.2a). Since the geometry of the fracture surfaces is clearly defined, the displacement of the two fracture surfaces in z-direction (vertical) results in different levels of contact area, and was consequently used as a calibration parameter. The range of contact area was set from 1 % up to 15 %. The contact area of 1 % was enforced as a minimum value for the mechanical aperture field to approximate the experimental setup of the air permeameter measurements. This represents the clamping stress that is applied to the fracture surfaces during the air permeameter measurements. The upper limitation of 15 % contact area was estimated from previous studies showing contact areas in the percentage range without mechanical stress (Crandall et al., 2010; Hakami & Larsson, 1996).

2.3 Results and discussion

2.3.1 Comparison of the fracture surface imaging methods

Figure 2.3 shows the mechanical aperture fields after matching of the two fracture surfaces with 1 % contact area according to the lower limit of the uncertainty range for the three different imaging devices with a_m values between 0 and 700 µm. Although all three aperture fields visually differ from each other, the results from HLS (top) clearly and significantly exceed the values of the other two aperture fields. Whereas the aperture fields obtained from MLS (middle) and SfM (bottom) show mainly reddish to yellowish colors corresponding to mechanical apertures up to 500 µm, large areas of the HLS derived aperture field show higher apertures (blue colors). However, there are also differences between the MLS and SfM aperture fields. For example, the general spatial distribution of the MLS aperture field is the same over the entire fracture area, whereas the SfM aperture field contains slightly increased apertures in the left and right boundary area of the fracture.

A qualitative metric for the resolution and the single point accuracy according to the manufacturer’s specifications is shown in Figure 2.1. It is noticeable that the MLS and SfM have an accuracy of < 50 µm and an accuracy-resolution ratio of about 4 % and 11 %, respectively, using the actual resolution of the point clouds. To generate point clouds with adequate quality, the optimal accuracy of an imaging device should be less than 5 % of the resolution (Tatone & Grasselli, 2012). In contrast, the accuracy for the HLS (≤ 500 µm) is about one order of magnitude higher compared to the other devices and, in addition, the accuracy-resolution ratio is 63 %. Consequently, the cloud points measured by HLS are likely to overlap and therefore do not reflect the actual geometry of the fracture surfaces. With respect to the accuracy-resolution ratio proposed by Tatone & Grasselli (2012), the MLS is the only approach that meets this criterion, whereas the HLS far exceeds this limitation. If the absolute mechanical apertures of the fracture (> 500 µm in the largest part of the fracture) are also considered, it is evident that the aperture field of the HLS is unsuitable as input for flow simulations.

Thus, the HLS derived aperture field is excluded from further hydraulic simulations. SfM also does not strictly fulfill the accuracy-resolution ratio criteria. However, since SfM provides a significantly smaller deviation (6 %) from the proposed limitation compared to HLS (58 %), SfM is also used for the flow simulations.

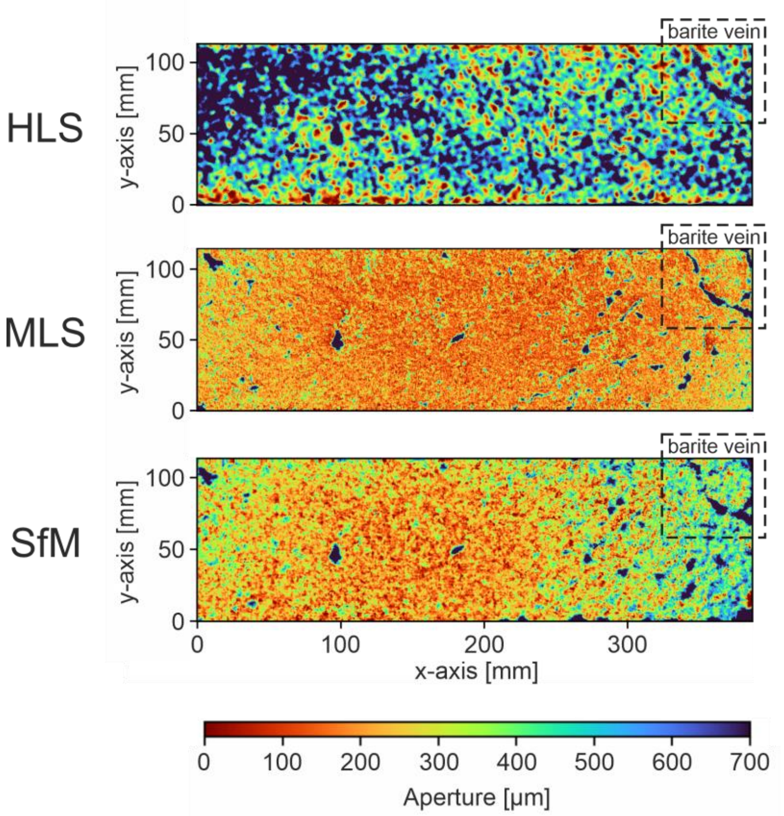

Figure 2.3: Comparison of the mechanical aperture fields of HLS, MLS, and SfM. The displayed aperture fields are initial results generated with 1 % contact area (lower limit of the calibration range) and are only used to evaluate the quality of the three imaging methods, but not for flow simulation. In all images, the barite vein crossing the fracture surfaces is marked in the top-right part.

2.3.2 Calibration of the hydraulic aperture

The mechanical aperture fields derived from MLS and SfM were used for fracture flow simulations. The calibration of the hydraulic apertures was performed by simulating several mechanical aperture fields with contact areas increasing in 1 % steps from 1 to 15 %. Figure 2.4 shows the difference between the average simulated hydraulic aperture and the average hydraulic aperture of the air permeameter measurements (81 ± 1 µm). It is shown that as contact area increases, the average hydraulic aperture decreases exponentially (Figure 2.4). The best match of simulation results and calibration data is achieved at 5 % contact area for the aperture field obtained by MLS and slightly higher at 7 % for SfM.

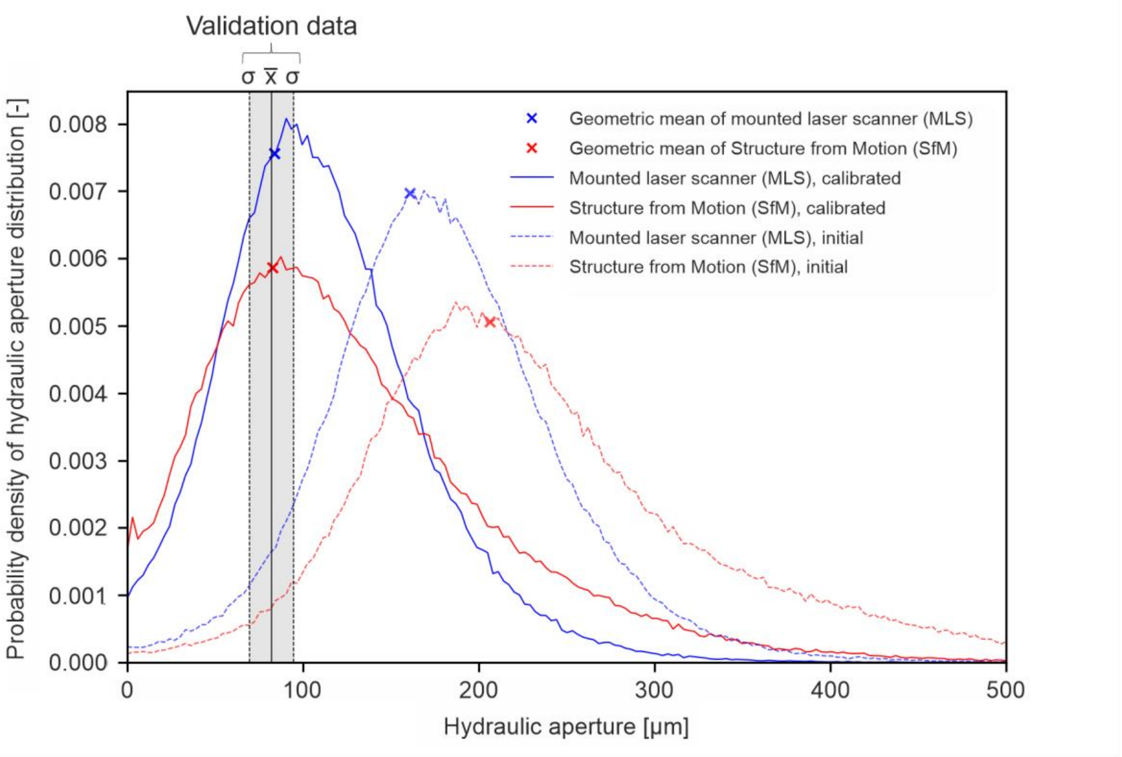

Figure 2.4: Probability distribution of the calibrated hydraulic aperture values and geometric mean for 5 % (MLS) and 7 % (SfM) contact area in solid lines and the initial hydraulic aperture values for 1 % contact area in dashed lines. The grey area shows the interval of standard deviation for air permeameter measurements. $\bar{x}$ is the mean, σ is the standard deviation of the validation data.

In Figure 2.5, the distribution of the apertures as well as the geometric mean hydraulic apertures for MLS and SfM are shown as 85 ± 2 µm and 83 ± 3 µm, respectively (Table 2.1). These results are consistent with other studies, which also have shown that even at low or non-existent external influences (e.g., mechanical pressure, sealing of the fracture), higher contact areas can be assumed in sandstones or granites (Blöcher et al., 2019; Crandall et al., 2010; Hakami & Larsson, 1996). Similar to this study, Blöcher et al. (2019) investigated a sample of Flechtinger sandstone and assumed a contact area of 20.1 % for their numerical simulation without external stress. Crandall et al. (2010) also obtained different contact areas when meshing identical µ-CT scans of the same fracture, depending on the meshing method. The contact areas for their sandstone sample range between 0 % and 12.5 %. In the study by Hakami & Larsson (1996), the contact area was determined experimentally using several cross-sections of multiple subareas of their fracture sample. They were able to show that all subareas provided contact area of above 0.5 % with some subareas showing contact areas of up to 7.0 %. It is therefore reasonable that the fracture has a contact area of 5 % or 7 % without external influences, respectively.

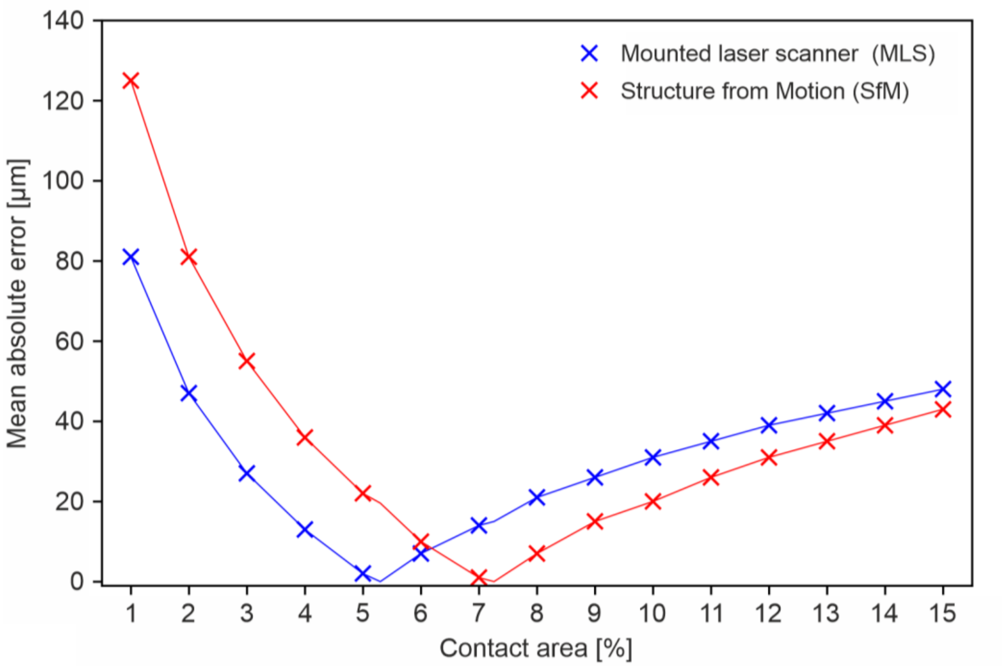

Figure 2.5: Mean absolute error of the average hydraulic aperture derived from (1) MLS and (2) SfM compared to the air permeameter measurements at contact areas of 1 % up to 15 %.

Table 2.1: Geometric means and geometric standard deviations of the aperture distributions for initial and calibrated MLS and SfM geometries.

Method	Geometric mean [µm]	Geometric standard deviation [µm]
MLS, calibrated	85	2.4
SfM, calibrated	83	3.0
MLS, initial	163	1.8
SfM, initial	207	1.8

However, there are some factors that could affect the flow simulation results and the air permeameter measurement leading to uncertainties in the calibration process and the determined values for the contact areas.

Firstly, the simulations are based on simplified governing equations such as Darcy's Law and the cubic Law. Previous research found that such simulations tend to overrate the flow through fractures (e.g., Brush & Thomson, 2003; Egert et al., 2021; Marchand et al., 2020). The overestimation amounts up to 19 % for linear flow, but can increase significantly for turbulent flow with Reynold's numbers (Re) > 100 (Egert et al., 2021). However, in this study all cells obtained by MLS at 5 % contact area and SfM at 7 % contact area show Re < 100 with maximum values of Re = 16 for MLS and Re = 51 for SfM, respectively. In addition, > 99 % (MLS) and 99 % (SfM) of the cells yield Re < 10. The simulation is therefore not significantly affected by non-linear flow (Egert et al., 2021). Re > 10 occur mainly in and around the barite vein and are thus spatially restricted, so that the general flow regime of the fracture does fulfill the assumptions made using Darcy's Law and cubic Law and do not provide turbulent flow effects. Hence, the real flow velocity should be less affected than the literature value of 19 % compared to the simulation results. Since a decrease in flow velocities does not propagate linearly to a reduction in simulated hydraulic apertures, this could only have minor influence on the results of the flow simulation.

Furthermore, the air permeameter measurements could be influenced by uncertainties resulting from the experimental setup and manually matching the fracture surfaces of the sample. The pressure exerted by the clamps on the sample could cause small-scale shearing of the two fracture surfaces against each other which would affect the contact area in a range of up to multiple percentages (Giwelli et al., 2014; Nemoto et al., 2009). In general, increasing shear displacement results in the reduction of contact area and the increase of apertures, but also in the broadening of the aperture distribution enabling a local increase of contact area (Giwelli et al., 2014). In addition, due to the two-dimensional representation of the fracture, only the contact area in the vertical (z) direction (caused by vertical displacement of one fracture surface) is considered in the simulation, but not the contact area along the flanks of the asperities (horizontal contact area). In the real fracture, it is possible that the vertical contact area is less and additional horizontal contact area exists.

2.3.3 Hydraulic aperture field analysis

Calibration of the model has shown that although the different imaging methods result in similar values for contact area, there are still differences in the spatial distribution of hydraulic aperture. A more detailed analysis reveals significant local differences between the mechanical and hydraulic aperture fields as well as between the MLS and SfM (Figure 2.6a). For example, in all aperture fields, the hydraulic apertures along the edges are higher compared to the center. This originates primarily from higher mechanical apertures consisting of more widely open and smoother relief of the fracture surfaces, such as the barite vein that was visually identified in the upper right part of the fracture. This causes channeling of fluid flow in continuous areas of enlarged aperture values (Figure 2.6b). Assessing flow channeling is crucial for single fracture flow simulations, because turbulent flow due to high flow velocities can potentially occur rendering the assumptions behind Darcy's Law and the cubic Law invalid (Hakami, 1995; Zimmerman & Bodvarsson, 1996). However, a quantitative assessment of hydraulic apertures for high flow velocities is difficult, because the cubic Law overestimates actual flow velocities, and as a consequence, hydraulic apertures can exceed mechanical apertures (Egert et al., 2021; Neuville et al., 2010). As indicated before, this is negligible in this study, due to locally limited possible flow effects and over 99 % of the fracture showing linear flow.

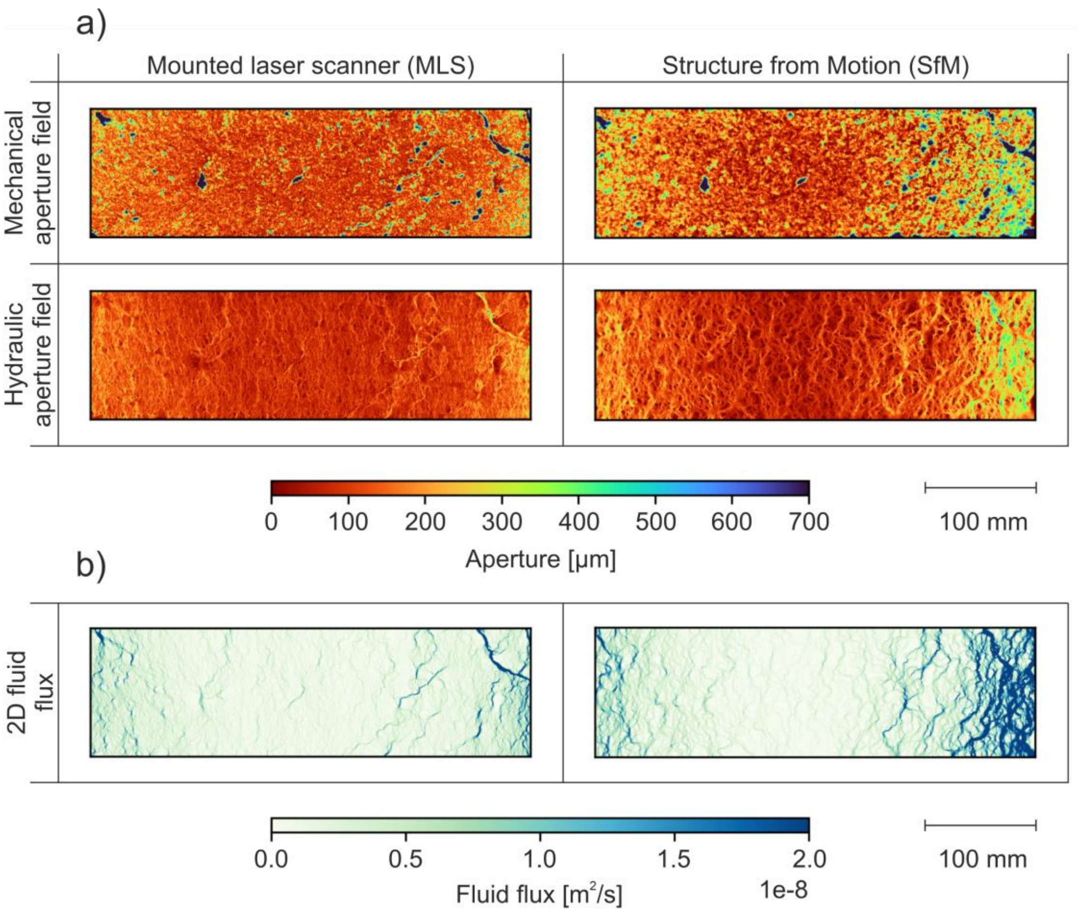

Figure 2.6: a) Mechanical and hydraulic aperture fields and b) 2D flux fields of the results derived from the MLS (left) and the SfM (right) method. The aperture fields are provided after calibration for 5 % (MLS) and 7 % (SfM) contact area, respectively.

Increased occurrence of channeling can be seen in the SfM compared to the MLS aperture field, especially in the center of the fracture. This is caused by the lower single point accuracy of SfM (~ 35 µm) compared to MLS (10 µm) and the concomitant increase of roughness due to poorer accuracy (Tatone & Grasselli, 2012). Consequently, the fluid flow through the fracture is more split due to the higher asperities of the aperture field and more preferential flow paths are formed. This in turn results in increased channeling. In addition, calculations presented in Tatone & Grasselli (2012) showed that a difference of 20 µm in 3D single point accuracy and a fracture mechanical aperture of 81 µm, as it is the case in this study, can result in an increase of up to 12 % in the mechanical aperture, assuming that the error in accuracy is equally distributed over all three spatial directions. This can subsequently also be reflected in the hydraulic aperture, since higher hydraulic apertures mainly follow higher mechanical apertures. Thus, the higher contact area corresponding to the higher closure of the SfM aperture field, which is required to fit the average hydraulic aperture of the MLS aperture field, can also be explained.

However, not all areas with high mechanical apertures correspond to high hydraulic apertures. In Figure 3.6, there are areas with high mechanical apertures that are not connected to major flow channels, but surrounded by lower permeability areas restricting fluid flow and resulting in small hydraulic apertures.

Nevertheless, the flow behavior in fractures with higher roughness seems to be consistent with other studies in which fractures are closed mechanically in a stress field. Javanmard et al. (2021), for example, simulated fluid flow through different synthetic fracture samples using a contact model with stress levels from 0 to 50 MPa. They displayed that flow is compressed in few main flow channels with significantly increased flow rates compared to the surrounding fracture parts. Similar work was done by Deng et al. (2021), who could show that with increasing contact area the number of flow channels decreases for an artificially generated, self-affine fracture. Hence, at high contact areas of around 50 %, nearly the entire flow occurs in one flow channel in their study. However, a correlation between contact area and channeling was already investigated previously using experimental as well as numerical methods (e.g., Méheust & Schmittbuhl, 2003; Nolte et al., 1989; Unger & Mase, 1993). As it is shown in these studies, it is also probable that there is a correlation between channeling and the measurement accuracy of the imaging method.

2.4 Conclusions

We evaluated three different fracture imaging methods: (1) a handheld laser scanner (HLS), (2) a mounted laser scanner (MLS), and (3) a single lens reflex camera used for Structure from Motion (SfM). The focus was set on the usefulness of their results for numerical simulations of flow through a single fracture and the calibration of these with hydraulic apertures directly measured using an air permeameter. Numerical simulations of the fluid flow based on the cubic Law and Darcy’s Law were performed using a two-dimensional representation of the fracture.

It was demonstrated that single fracture flow simulations require sufficient resolution and accuracy of the imaged fracture surfaces to achieve meaningful results. The resolution should be high enough to cover all important structures of a fracture surface. Although Tatone & Grasselli (2012) proposed that the accuracy should not be higher than 5 % of the resolution, our study showed that an accuracy-resolution ratio of 11 % also provides acceptable results. The applied handheld laser scanner failed these requirements and is therefore not suitable for the application in single fracture flow simulations.

The calibration of the hydraulic apertures revealed a good fit to the air permeameter measurements for 5 % (MLS) and 7 % (SfM) contact area, respectively. Fluid flow simulations illustrated that the main flow occurs in predefined structural flow channels, where the mechanical aperture is locally increased. The development of flow channels is influenced by the resolution and accuracy of the imaging method as well as the matching of the imaged fracture surfaces. The SfM aperture field shows more channeling compared to MLS due to slightly poorer single point accuracy.

Overall, it is illustrated that the SfM method delivers results that are comparable to those from the significantly more expensive and less mobile MLS. Further research is required to confirm our findings for more challenging applications such as larger field applications. To address uncertainties which arose during this study, Navier‑Stokes equations could be solved in the simulation process instead of assuming Darcy Flow. This could prevent the overestimation of flow through the fracture due to possible turbulent flow effects in areas with high mechanical apertures. To apply the Navier‑Stokes equations, a three-dimensional representation of the fracture is required, which, however, would also result in the additional consideration of horizontal contact area on the flanks of the asperities. Nevertheless, one of the major uncertainties that has to be considered in future work is the matching of the fracture surfaces, since even small displacements or rotations can result in large different mechanical apertures. An optimal approach would be to place georeferenced points in and around the fracture, so that they can be scanned and merged in an appropriate way. However, this method still has to be tested, as it currently has too high measurement inaccuracies. After eliminating these uncertainties, future research should also focus on confirming the applicability of SfM in other applications such as several different fractures, fracture sizes, lithologies and dimensions. Due to its more mobile application and better cost efficiency, the SfM method seems to be especially promising for studies on drilling cores or larger outcrops in the field.

Acknowledgements

The support by Kristofer Marsch in setting up the Structure from Motion (SfM) approach is greatly acknowledged. This study was mainly carried out in the framework of the subtopic “Geoenergy” in the program “MTET – Materials and Technologies for the Energy Transition” of the Helmholtz Association.

3 Investigating rough single-fracture permeabilities with persistent homology

Reproduced from: Fuchs, M., Suzuki, A., Hasumi, T., Blum, P. (2024): Investigating rough single-fracture permeabilities with persistent homology. Solid Earth 15, 353-365, https://doi.org/10.5194/se-15-353-2024

Abstract

The permeability of rock fractures is a crucial parameter for flow processes in the subsurface. In the last few decades, different methods were developed to investigate on permeability in fractures, such as flow-through experiments, numerical flow simulations, or empirical equations. In recent years, the topological method of persistent homology was also used to estimate the permeability of fracture networks and porous rocks, but not for rough single fractures yet. Hence, we apply persistent homology analysis on a decimetre-scale, rough sandstone bedding joint. To investigate the influence of roughness, three different data sets are created to perform the analysis: (1) 200 µm, (2) 100 µm, and (3) 50 µm resolutions. All estimated permeabilities were then compared to values derived by experimental air permeameter measurements and numerical flow simulation. The results reveal that persistent homology analysis is able to estimate the permeability of a single fracture, even if it tends to slightly overestimate permeabilities compared to conventional methods. Previous studies using porous media showed the same overestimation trend. Furthermore, the expenditure of time for persistent homology analysis, as well as air permeameter measurements and numerical flow simulation, was compared, which showed that persistent homology analysis can be also an acceptable alternative method.

3.1 Introduction

The permeability of rocks is a crucial parameter for fluid flow processes in the subsurface. While the prevailing flow processes in porous media are well understood, a different picture emerges when the flow is dominated by fractures (Suzuki et al., 2019). Although flow in geological settings controlled by fractures is occurring in both shallow aquifers (e.g., for drinking water supply) and deep reservoirs (e.g., geothermal energy production and oil and gas abstraction), fractures are often simplified as two parallel plates. In addition, due to complexity reasons, a single parameter, the hydraulic aperture, is often used to represent the permeability of a single fracture or even entire discrete fracture networks (Blum et al., 2009; Min et al., 2004; C. Müller et al., 2010). However, due to roughness of fracture surfaces, a single value is not sufficient to capture the flow channelling and critical flow paths (Tsang & Neretnieks, 1998; Tsang, 1992). Hence, investigations of the fracture roughness are essential, although this is more expensive in terms of the costs and time (Tatone & Grasselli, 2012, 2013).

Nowadays, various methods are available to study how fluid flow is influenced by fracture roughness through single fractures. These can be divided into four major categories: (1) empirical, (2) experimental, (3) numerical, and (4) geometric methods.

Empirical methods are simple and also fast, cheap, and often sufficient to provide a first overview over the flow behaviour of a fracture. There are different empirical models derived from flow experiments, numerical simulations, or statistical models of different fracture types (Barton & De Quadros, 1997; Kling et al., 2017; Louis, 1972; Suzuki et al., 2017; Xiong et al., 2011). Often, solely mechanical apertures and relative roughness, depending on the standard deviation, are required to not only calculate hydraulic apertures but also the fractal dimension or the Peklenik number, which is defined as the ratio of the correlation length in the x- and y-directions (Brown, 1987; Patir & Cheng, 1978).

Experimental methods provide more detailed results than empirical methods which use more simplified relations for fast practical application. The standard methodology is flowthrough experiments at laboratory scale to observe flow patterns in single fractures (Brown et al., 1998; Ferer et al., 2011; Watanabe et al., 2008). In recent years, hydromechanical coupling (Vogler et al., 2018; Wang et al., 2021) or reactive transport have additionally been performed for the exclusive investigation of flow patterns in flow-through experiments (Durham et al., 2001; Huerta et al., 2013). In addition to typical flow tests at laboratory scale, it is also possible to perform flow experiments on larger scales in the laboratory or in the field (Novakowski & Lapcevic, 1994; Thörn & Fransson, 2015; Weede & Hötzl, 2005). Flow-through experiments allow us to investigate direct fluid flow through fractures. The flow distribution and preferred flow paths can be predicted by replicating the fracture geometry in transparent materials. Beside flow-through experiments, air permeameters can be used to determine the permeability of fractures (Cheng et al., 2020; Hale et al., 2020; Hale & Blum, 2022). Air permeameters allow us to measure the permeability of fractures directly on an outcrop or drilling core (Brown & Smith, 2013). In addition, it is also possible to obtain a zonal observation of the permeability, since several measurements have to be conducted along a fracture outcrop due to the measurement method (Hale et al., 2020).

Another way to investigate flow in fractures is the representation of the fracture in numerical models. For this purpose, the geometry of a fracture is either projected onto a two-dimensional surface (Javanmard et al., 2021; Pyrak-Nolte & Morris, 2000) or represented in three dimensions (Chen et al., 2021; Javadi et al., 2010; Wang et al., 2016; Xiong et al., 2011). The latter increases the computational effort considerably and also allows a more accurate investigation of flow processes. Another major advantage is that it is possible to simulate various scenarios under different conditions, such as high confining pressures or high flow rates, which would exceed technically possible conditions in laboratory experiments. In addition, numerical models are able to consider flow effects, region by region, in the fracture and therefore characterize the main flow paths (Javanmard et al., 2021; Marchand et al., 2020). However, the geometry of the fracture and the prevailing boundary conditions for simulations have to be precisely known in order to obtain meaningful results (Barton et al., 1985; Tatone & Grasselli, 2012).

If the focus is set on the investigation of the flow behaviour and permeability distribution within the fracture, then geometric methods can also be used. The Kozeny–Carman equation is well known as a representative method for estimating flow properties from pore structures (Carman, 1937; Kozeny, 1927), and attempts have long been made to estimate permeability by extracting porosity from images without experiments or numerical simulations (Costa, 2006; Oliveira et al., 2020; Torskaya et al., 2014). More recently, attempts have been made to use machine learning or deep learning on images (Alqahtani et al., 2021; Anderson et al., 2020; Araya-Polo et al., 2020; Da Wang et al., 2021; Hong & Liu, 2020; Sudakov et al., 2019). Of course, deep learning is a powerful method, but adequate use of machine learning requires deep technical understanding, rigorous testing, and sufficient amounts of training data.

Topological data analysis (TDA) is another way to extract the information of shapes and structures from big data (Carlsson, 2009; Thiele et al., 2016). TDA is an analysis method that focuses on the structure of data within the field of algebraic topology, demonstrating particular strengths in handling data types such as images, complex structures, and networks. TDA can capture the structure of the data in a rough sense and characterize the features of connectivity and holes, therefore ignoring noises in data and extracting important information, such as the independent of coordinate system and number of dimensions. Persistent homology (PH), one of the most used TDA methods, can capture changes and continuity of topological features by tracking algebraic descriptions called homology. This method was developed in the early 2000s (Edelsbrunner et al., 2000; Zomorodian & Carlsson, 2005) and is applied in various research fields such as materials science (Hiraoka et al., 2016), computer science (Choudhury et al., 2012), and biology (Chan et al., 2013). In geosciences, this approach has only been applied in the past decade to characterize porous rocks and to determine their permeability (Bizhani & Haeri Ardakani, 2021; Delgado-Friedrichs et al., 2014; Robins et al., 2016). Furthermore, the determination of hydroelastic properties of porous media is possible with this method (Jiang et al., 2018). In the field of fractured rocks, persistent homology was recently also applied to study small-scale fracture networks (Suzuki et al., 2020, 2021). Based on these studies, the general application of PH for permeability estimation of fracture networks could be demonstrated. In these small-scale (millimetre to centimetre scale) studies, the effect of fracture roughness was not particularly investigated (Suzuki et al., 2020, 2021). Further research is therefore needed to investigate larger-scale fractured rocks, in which surface roughness has a significant effect on flow behaviour.

The objective of this study is therefore the application of the persistent homology analysis on a natural, mesoscale (decimetre scale) single fracture to estimate the permeability. The focus is on the anisotropy of permeability in different flow directions, as well as the influence of resolution on permeability. Thus, three data set of the same fracture are prepared, which have different resolutions (50, 100, and 200 μm). Finally, these results are compared with results from experimental air permeameter measurements, as well as numerical flow simulations.

3.2 Methods

3.2.1 Fracture sample

The fracture sample is a natural bedding joint in a sandstone block taken from a quarry in Bebertal, Germany (Figure 3.1; Hale & Blum, 2022; Heidsiek et al., 2020). The sandstone is Flechtinger sandstone, an oil and gas reservoir rock in the North German Basin. The block contains one bedding joint, with a length of 120 mm in the x-direction and 450 mm in the y-direction (Figure 3.1). Previous studies have already characterized the relevant hydromechanical properties of Flechtinger sandstone such as porosity (9 %–11 %), matrix and fracture permeability, Young’s modulus and bulk modulus, thermal dependencies of stress and strain behaviour, and the mineralogical composition (Blöcher et al., 2019; Cheng et al., 2020; Fischer et al., 2012; Frank et al., 2020; Hale et al., 2020; Hale & Blum, 2022; Hassanzadegan et al., 2012; Heidsiek et al., 2020). Of particular interest for this study is the low-matrix permeability of 0.1-1 mD (Cheng et al., 2020; Hassanzadegan et al., 2012). Furthermore, the findings of Gutjahr et al. (2022), Hale et al. (2020), and Hale and Blum (2022) are crucial, since they performed investigations on fracture permeability on exactly the same fracture. Gutjahr et al. (2022) investigated on the roughness of the fracture and calculated the Hurst exponent for different angles. The medians of all Hurst exponents in the x-direction and in the y-direction are 0.48 and 0.42, respectively. Hale et al. (2020) and Hale & Blum (2022) determined the average fracture permeability to be $5.6 \cdot 10^{-10}$ m². In addition, they found that the centre of the fracture is less permeable than the left and right side of the fracture (according to the front view of the sandstone block shown in Figure 3.1). On the right-hand side of the fracture, this can be explained by a barite vein intersecting the fracture, which was formed before the fracture opening. In the closer vicinity of the vein, the mechanical aperture is increased compared to central parts of the fracture. Comparing fracture and matrix permeabilities shows that the fracture permeability exceeds the matrix permeability by more than 8 orders of magnitude. Thus, the matrix permeability is considered negligible in this study.

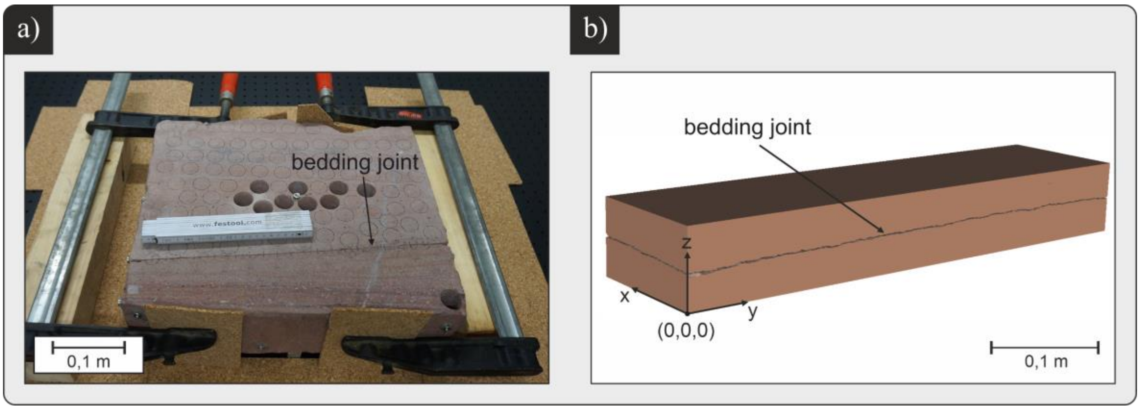

Figure 3.1: a) Photo of the studied sandstone block showing also the investigated bedding joint. The front surface of the real block corresponds to the y-z plane in the digital model on the right-hand side. b) 3D model of the bedding joint and the surrounding sandstone block.

3.2.2 Data preparation and matching

For data preparation, a self-developed Python code called FracMatchPy was used. This code is able to (1) match two separated and spatially uncorrelated fracture surfaces and (2) create binary cross sections of the fracture as input for the PH analysis.

In the matching process, meshed laser scans of the bedding joint surfaces were used as input data for the Python code (Figure 3.2). The surfaces were scanned by a combined system of the high-resolution laser scanner Nikon ModelMaker MMDx 100 and the articulated arm MCA II on which the scanner was mounted (Nikon Metrology NV, 2010, 2018). The scanner provides a resolution of 100 µm and a single-point accuracy of 10 µm (Nikon Metrology NV, 2018).

The scanned point cloud was then meshed using MeshLab (Cignoni et al., 2008). Since the meshes were not spatially related, the two surfaces were roughly matched by hand to shorten the runtime of the Python code for data preparation. The exact matching was then performed stepwise by several rotation and translation steps within specified limits using the Python code. The translation limit was 3 mm total distance in each direction so that one surface was displaced in 100 µm steps, starting from the geometric center of the surface. In addition, there was a rotation range of -0.3 to 0.3 ° in which the rotation was performed in 0.01 ° steps. The best fit was then determined by applying a minimization function of the average mechanical aperture using the arithmetic mean between the fracture surfaces.

3.2.3 Binary image generation and permeability estimation using persistent homology

We apply the permeability estimation method proposed by Suzuki et al. (2021), which uses persistent homology (PH) to extract information about the flow channels from image data. The first step is to convert the fracture information prepared in Section 3.2.2 into 3D binarized image data sets.

Three-dimensional image construction of the bedding joint and the surrounding sandstone block was generated. The image construction is a series of binary cross-sectional images of the x-z planes along the y axis. The size of the image area is 115 mm × 8.4 mm × 392.2 mm. Three data sets with different resolutions were generated to investigate the effect of varying resolution on permeability estimation. The first data set was created with a low resolution of 200 µm in all spatial directions. The data set contains 578 × 1962 × 42 voxels. The second data set was generated with a medium resolution of 100 µm in each spatial direction. The data set contains 1154 × 3922 × 84 voxels. In the third data set, the resolution was again reduced by half to 50 µm in all spatial directions. The data set contains 2308 × 7844 × 169 voxels. The fracture was considered to be fully permeable, with no low-permeable filling or sealing. Since the matrix permeability is 8 orders of magnitude lower than the fracture permeability, the matrix was considered to be fully impermeable (Cheng et al., 2020; Hassanzadegan et al., 2012). Thus, each image contains the permeable fracture in white colors (binary value = 1) and the impermeable matrix in black colors (binary value = 0).

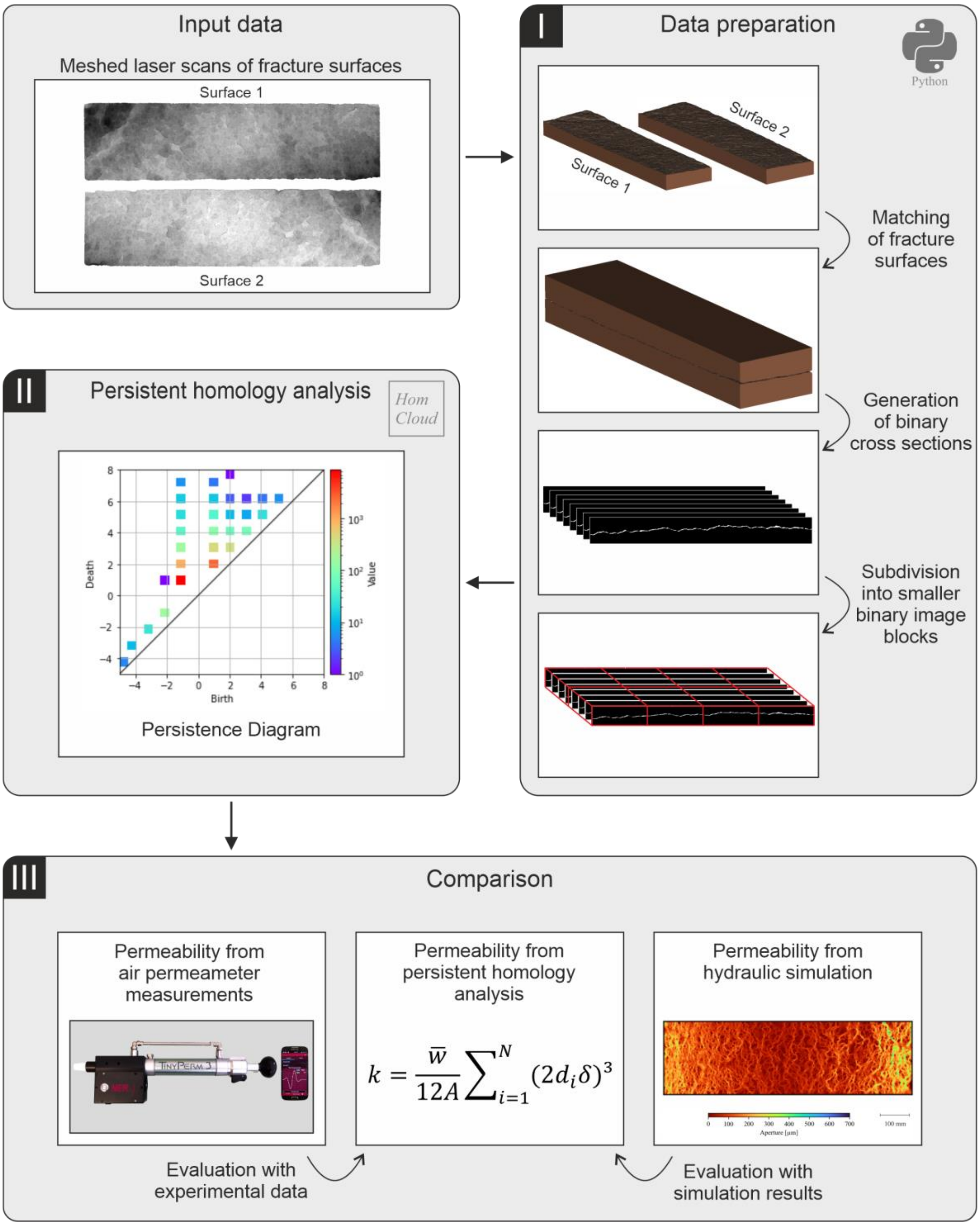

Figure 3.2: Workflow of this study with three distinct steps, which is applied on the laser-scanned fracture surfaces.

PH analysis was then performed using HomCloud (Obayashi et al., 2022). Since HomCloud can only handle a maximum data volume of 1021 × 1021 × 1021 voxels in a single-analysis run, the data sets were divided into several subpackages which were processed separately (Figure 3.2). The data set with low resolution (200 µm/pixel) has 578 × 1962 × 42 voxels and was split into two divisions in the y-direction. Thus, two subpackages were created for the data set with low resolution, each of which contained 578 × 981 × 42 voxels. Dividing the x-direction and z-direction for the data was not necessary because the length of one side of the image was < 1021 pixels. The data set with middle resolution (100 µm/pixel) has 1154 × 3922 × 84 voxels and was split into two divisions in the x-direction and four divisions in the y-direction. The data set was divided into eight subpackages, with an average of 577 × 981 × 84 voxels each. The data set with high resolution (50 µm/pixel) has 1154 × 3922 × 84 voxels and was split into three divisions in the x-direction and eight divisions in the y-direction. The data set was divided into 24 subpackages, with an average of 769 × 981 × 169 voxels each.

PH analysis was then performed for each subpackage. HomCloud enables the extraction of topological features; a 3D object can consist of three different topological features. First, 0-dimensional topological features characterize connected components such as impermeable, solid matrices without voids. Structures such as fractures or connected pores are recognized as 1-dimensional (1D) topological features. Finally, 2-dimensional (2D) topological features are represented by enclosed pores not connecting to other flow channels. Since only fractures connected between an inlet and an outlet of the domain can serve as potential flow channels, this study focuses on the analysis of 1D topological features.

In HomCloud, a process called filtration is performed to detect 1D topological features from image data. For simplicity, an example of a two-dimensional image is shown in Figure 3.3. In the binary image, the black areas are the rock matrix (binary value = 0), while the white areas are the void space (binary value = 1). During the filtration, the black pixels are thinned or thickened by 1 pixel from the boundary between the white and black pixels. The process is considered to be time variation, and the initial image is assumed to be time 0 (t = 0). The time change in the negative direction is to make the black pixels thin, and the time change in the positive direction is to make the black pixels thick. The images are stored at each time. Continuing this operation, if the pixels continue to be thinned (time change in the negative direction), then the image becomes all white. If time is advanced in the positive direction from the all-white state, then a channel (i.e., 1D topological feature) appears at certain times, and if time is continuously advanced in the positive direction, then the channel disappears further. Note that the channel (1D topological feature) here is the connected shape from left to right, surrounded by black pixels. These times are called birth (b) and death (d), respectively. This method is named “persistent homology” because it attempts to see how persistent topological features are. While other topological data analysis extracts only topological features, the advantage of PH is that by utilising birth-death information, one can obtain not only topological features but also the geometric information on length.

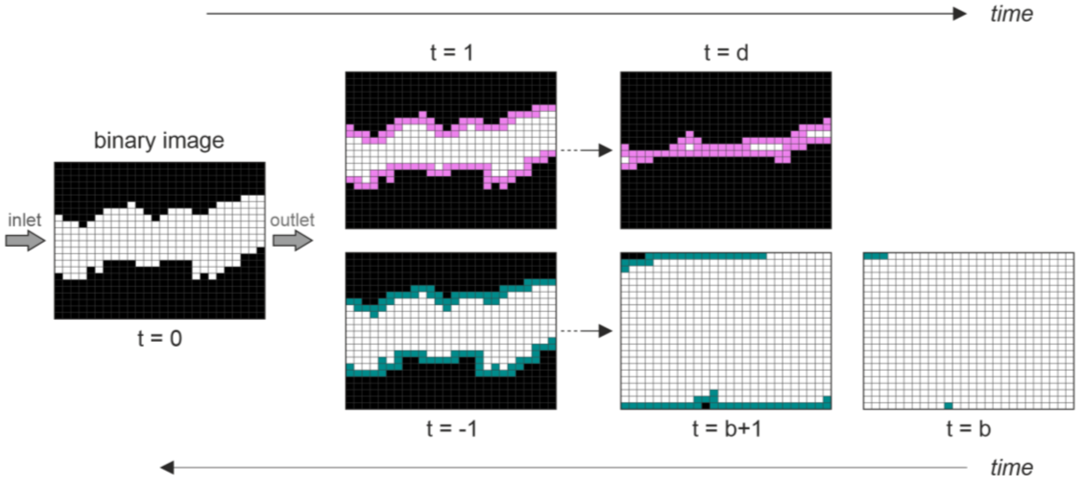

Figure 3.3: Schematic illustration of the filtration process during persistent homology analysis. The permeable area of the binary image (fracture) is thickened (cyan) and thinned (pink).

In HomCloud, the output is a persistence diagram representing a frequency distribution of the number of birth and death pairs, as shown in step II in Figure 3.2. From the definitions of birth and death, the presence of a flow channel (1D topological feature) in an image means that birth time is negative and death time is positive. Thus, the number of such pairs ($b < 0 < d$) can be considered to be the number of flow channels in the image. In addition, in the case of the process of the thickening of the black area, as shown in Figure 3.3, the fracture is closed from both sides (see the image labeled “t = d”). Therefore, the doubling of death and multiplying by the resolution of the image can be taken as the smallest aperture of the channel. Thus, from HomCloud, the frequency distribution of the number of channels present in the image and their minimum aperture widths can be obtained. It is important to note that the 1D topological features evaluated in PH include the aforementioned left-to-right connected shapes surrounded by black pixels, as well as the void ring structures that are not connected to the outside. How to remove such structures is described in Suzuki et al. (2021). It should also be noted that if the channels are connected like a ladder, then PH may detect a large number of channels. Suzuki et al. (2021) assumed that the channels have parallel-plate geometries and that they are parallel to each other. The permeability is estimated based on the power law as follows:

$$k = \sum_{i=1}^{N} \frac{w_i a_i^3}{12A} \tag{3.1}$$

A is the surface area of the cross-section of the medium, and N is the number of flow channels. w_i is the depth of flow channel i, and a_i is the aperture of the flow channel i. As mentioned above, the number of flow channels N was estimated from the number of birth-death pairs, and the aperture a_i was estimated as $2d_i r_b$ in PH analysis, where d_i is the death of the flow channel i, and r_b is the resolution of the images. The average of the depth of the flow channel $\overline{w}$ is determined by the cross-sectional area of the image (Suzuki et al., 2021). Thus, the above equation can be converted to the parameters from PH and image analysis.

3.2.4 Experimental measurement of the fracture permeability

An air permeameter was used to experimentally measure the fracture permeability. The transient air permeameter TinyPerm 3 (manufactured by New England Research, Inc.) is a portable device, which is able to directly measure matrix permeabilities or hydraulic fracture apertures on outcrops or cores (Cheng et al., 2020; Filomena et al., 2014; Hale & Blum, 2022). For this purpose, the device is filled with air by lifting the piston, and the rubber nozzle of the instrument is pressed against the fracture outlet. The measurement is started by depressing the piston in direction of the sample, creating a vacuum between the fracture and the device. A microcontroller unit in the air permeameter simultaneously records the transient change in air pressure at the fracture outlet and the volume change in the device. Once the total volume of the device is compressed, the permeability is automatically determined from the recorded curve (Brown & Smith, 2013). The range of measurable permeabilities is from 1 mD to 10 D for porous rocks and hydraulic apertures of approximately 10 μm to 2 mm for fractures (New England Research Inc., 2016). The latter corresponds to permeabilities in orders of magnitude from 10^{-11} m² to 10^{-7} m².

This study uses both existing air permeameter measurements from Hale et al. (2020) and measurements conducted in this study. In the study of Hale et al. (2020), experiments along the long edge (y-direction) of the fractured block were performed, and the permeability in the x-direction was measured. In addition, complementary measurements along the x-axis with permeabilities measured in the y-direction were performed in the frame of this study. In total, the y-axis was divided into 21 sections and the x-axis into 4 sections. The corner areas were not included in the measurement due to breakouts from the block. Each section was measured 10 times to obtain average values. The hydraulic aperture along the y edge in the x-direction was determined to be 81 ± 1 μm (Hale & Blum, 2022) and that along the x edge in the y-direction to be 57 ± 1 μm.

3.2.5 Numerical flow simulation

Apart from experimental air permeameter measurements, hydraulic apertures of the fracture were also determined by numerical flow simulations, using the Multiphysics Object-Oriented Simulation Environment (MOOSE) framework (Permann et al., 2020). Within this framework, the fluid flow through the fracture was simulated with the SaintBernard application (Schädle, 2020), which is based on the inbuilt PorousFlow module (Wilkins et al., 2020, 2021). In this application, a 3D fracture is projected on a 2D surface embedded in a 3D environment. The aperture of the fracture is assigned as a permeability parameter to each cell of the 2D mesh. The fluid flow velocity is then simulated in the lower dimension, and the hydraulic aperture is calculated, considering Darcy flow and the cubic law with the following equation for each cell of the mesh:

$$a_h = \sqrt[2]{\frac{12v\mu L}{\Delta p}} \tag{3.2}$$

In Equation 3.2, a_h is the hydraulic aperture of the fracture, v is the fluid flow velocity, μ is the dynamic viscosity, L is the length of the fracture (in flow direction), and Δp is the hydraulic pressure gradient. Further information about the numerical simulation and SaintBernard can be found in Javanmard et al. (2021).

Similar to the air permeameter measurements, numerical flow simulations were performed with fluid flow in both the x- and y-direction to determine the permeability in each of these.

3.3 Results and discussion

3.3.1 Permeability estimation from persistent homology analysis

The prepared binary data sets were used to calculate the permeability of the fracture. The permeability was calculated in two different flow directions for flow parallel to the x-axis and parallel to the y-axis (Figure 3.4). The calculated permeabilities for the 200 µm resolution data set are $6.4 \cdot 10^{-10}$ m² in the x-direction and $6.2 \cdot 10^{-10}$ m² in the y-direction. Using the cubic law, the calculated hydraulic apertures are 88 µm and 86 µm, respectively. For the data set with 100 µm resolution, the permeabilities are $4.4 \cdot 10^{-10}$ m² in the x-direction and $4.0 \cdot 10^{-10}$ m² in the y-direction. This corresponds to hydraulic apertures of 73 µm in the x-direction and 69 µm in the y-direction. For the 50 µm resolution data set, the permeability in the x-direction is $7.0 \cdot 10^{-10}$ m² and $3.2 \cdot 10^{-10}$ m² in the y-direction, which equals hydraulic apertures of 92 µm and 62 µm, respectively. Comparing the three different data set shows that PH analysis for all data sets results in higher permeability in the x-direction than in the y-direction ($k_x/k_y > 1.0$).

The k_x/k_y ratio of the data sets with 200 µm and 100 µm resolution is nearly identical, 1.0 and 1.1, respectively, whereas the ratio of the 50 µm data set shows a higher ratio of 2.2.

Detailed examination of the individual fracture surfaces and the matched fracture shows that the highest mechanical apertures of > 1 mm occur mainly along the barite vein that crosses the fracture parallel to the x-direction (Figure 3.4). From previous studies on the fracture, it appears that this barite vein dominates the flow behavior and, thus, forms the main flow path along the fracture due to its increased mechanical aperture and lower roughness compared to other regions of the fracture (Hale et al., 2020). Hence, it serves as a preferential flow path in the x-direction, whereas it acts more as a barrier or redirection for flow in the y-direction. The study of Gutjahr et al. (2022) shows that, in addition to the anisotropy of the permeabilities, a slight anisotropy of the roughness can be observed. Analogous to the permeability, the Hurst exponent in the x-direction is higher (H_x = 0.48) than in the y-direction (H_y = 0.42). It is noteworthy that the ratio of the Hurst exponents (H_x/H_y) is 1.1 and thus corresponds well with the determined ratios for permeabilities. This is reasonable, as increased roughness tends to result in more distinct flow channels with larger mechanical apertures. Consequently, this leads to increased permeabilities.

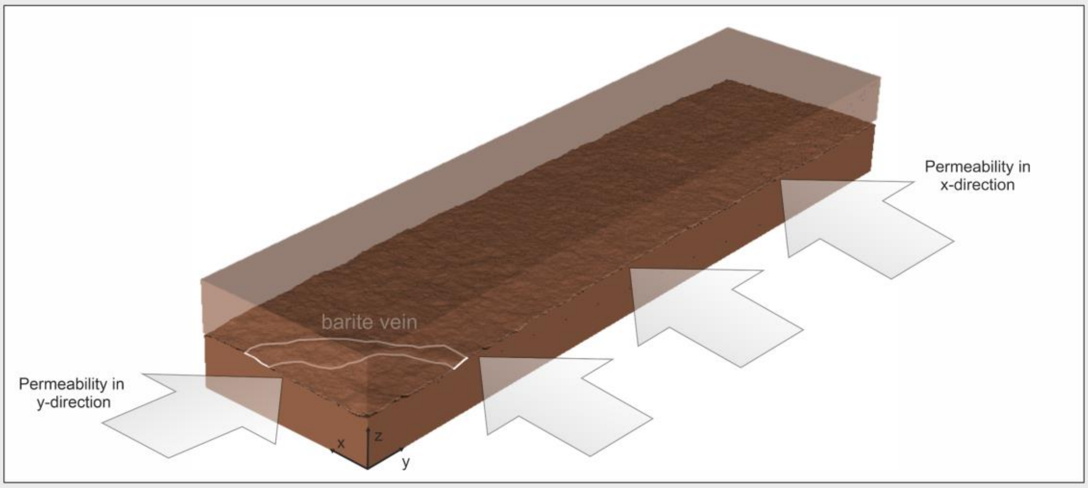

Method and data set	Permeability in x-direction k_x [m²]	Permeability in y-direction k_y [m²]	Permeability ratio k_x/k_y [-]
Air permeameter measurements	5.6×10^{-10}	2.7×10^{-10}	2.1
Numerical flow simulation	6.0×10^{-10}	4.4×10^{-10}	1.4
Persistent homology r = 200 µm	6.4×10^{-10}	6.2 x 10^{-10}	1.0
Persistent homology r = 100 µm	4.4×10^{-10}	4.0 x 10^{-10}	1.1
Persistent homology r = 50 µm	7.0×10^{-10}	3.2×10^{-10}	2.2

Figure 3.4: Permeability determined by air permeameter measurements, numerical flow simulations, and persistent homology using data sets with resolutions of 200 µm, 100 µm, and 50 µm.

3.3.2 Comparison to air permeameter measurements and numerical simulation

In addition to the estimation of the fracture permeability by PH, the results were also compared to permeabilities derived from alternative methods. Thus, a comparison was performed using experimental air permeameter measurements and numerical flow simulations to show the validity of the PH analysis. In Figure 3.4, the values for the permeability in the x- and y-directions, as well as the ratio of the two permeability values of air permeameter measurements and numerical simulation, are also shown. All x permeabilities differ by $< 1.5 \cdot 10^{-10}$ m² from the experimental or numerical results. However, the permeabilities in the y-direction scatter slightly more.

Overall, there is a good fit between PH analysis and alternative methods, which is reflected by a root mean squared error (RMSE) of $1.5 \cdot 10^{-10}$ m². Normalization with the difference between maximum and minimum of all observed permeabilities leads to a normalized root mean squared error (NRMSE) of 0.34. However, there is also the trend that the values agree increasingly better with the comparative values as the resolution of the data set increases. For example, the RMSE of the x and y permeability between air permeameter or numerical simulation and the 200 µm resolved data set is $2.0 \cdot 10^{-10}$ m². For the 100 µm data set, it reduces to $1.2 \cdot 10^{-10}$ m², and for the 50 µm data set, it is $1.1\ 10^{-10}$ m². The NRMSEs are 0.54 (200 µm), 0.38 (100 µm), and 0.25 (50 µm), respectively.

This trend was also shown in studies using persistent homology in porous media or fracture networks before (Moon et al., 2019; Suzuki et al., 2021). The study of Moon et al. (2019), in which fluid flow through the pore spaces of different digital sandstone and chalk samples was examined, could show particularly that the number of excessively high outlier permeabilities can be prevented with higher resolution. Similar findings are shown in Suzuki et al. (2021), in which permeabilities that are significantly higher than the comparison simulation could also be reduced by improving the resolution. Conclusively, it can be stated that apart from the permeability estimation of the 50 µm data set in the x-direction, the results of the PH analysis improve with increasing resolution.

3.3.3 Evaluation of persistent homology analysis

Since the results of three different methods for permeability determination are in good agreement (NRMSE = 0.34), a classification of the results in the context of other PH analyses was carried out. The study of Suzuki et al. (2021) applied PH on different data sets of porous and fractured rocks of previous studies (Andrew et al., 2014; Mehmani & Tchelepi, 2017; Muljadi et al., 2016). The 16 data sets of porous media and 15 data sets of fracture networks were analyzed, each with PH and numerical flow simulation. In Figure 3.5, the results of this study, as well as the results by Suzuki et al. (2021), are shown. The method of PH for permeability estimation in both studies provides comparable results to the respective reference method. The results of this study are closely scattered around the 1:1 line and thus match well with the results based on fracture networks (dark grey diamonds). It appears that the results of this study can be estimated even better than most of the data points of previous data sets, especially those generated from porous media (light grey crosses). In the latter, PH tends to overestimate the permeability, which cannot be confirmed for the data in this study. However, this study indicates that the quality of the permeability estimation is not only attributable to the type of cavity (pores, single fractures, or fracture networks). Based on the results, the quality of the permeability estimation by PH is also dependent on the resolution and anisotropy of the respective data set.

Nevertheless, a larger number of data sets should be examined for a more precise assessment of the various influences on the quality of the permeability estimation.

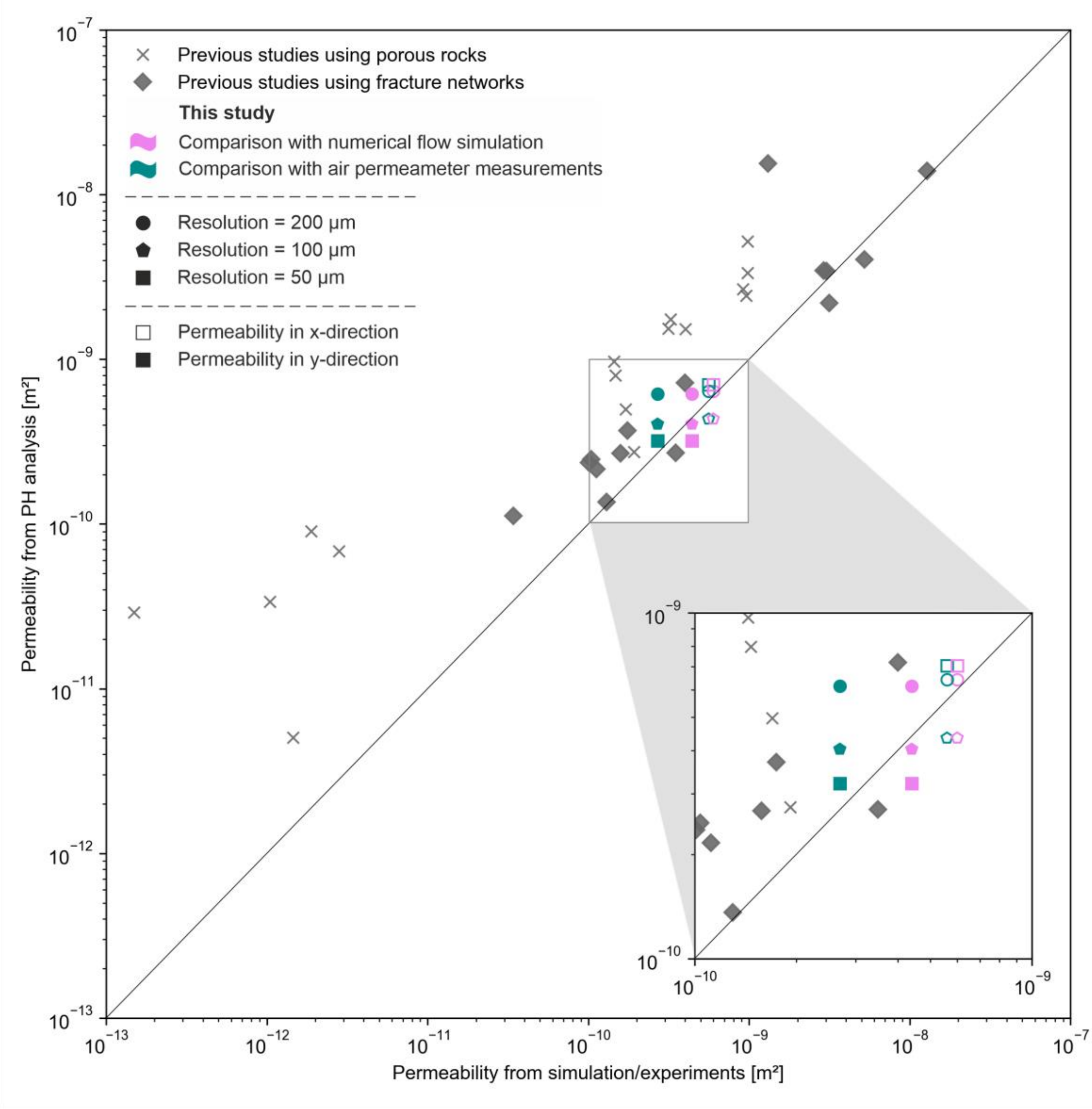

Figure 3.5: Comparison of the estimated permeabilities of this study with the estimated permeabilities for porous media (light grey crosses) and fracture networks (dark grey diamonds) of previous studies by Suzuki et al. (2021), using data of Andrew et al. (2014), Muljadi et al. (2016) and Mehmani and Tchelepi (2017).

In previous sections, it is shown that PH provides comparable results for permeability estimation of rough single fractures compared to other more conventional methods. However, for it to be an alternative, the effort and computational time also has to be considered. In Table 3.1, an estimation of different working steps is presented for the permeability estimation of single fractures. For PH analysis, the dependency of the time needed on the resolution is also considered. The table is divided into three working steps. The step of preparation and preprocessing contains every working step after the collection of a sample, including imaging and matching of fracture surfaces, generating binary images, setting up a numerical model, or initialising the air permeameter. In the second working step, the effort for the actual measurement, numerical simulation or PH analysis is considered for one sample. In postprocessing, all working steps recalculating the fracture permeability from the measured, simulated, or analysed results is considered. Comparing the expenditure of time for all methods and resolutions, all methods apart from PH analysis for 50 µm data are ranging in the same order of magnitude. An increase to 50 µm resolution demands an enormous increase in time expenditure, mainly due to the extremely high analysis time. Considering the quality of the results, the data set with 100 µm therefore seems to be an adequate alternative to conventional methods, as it can provide high-quality results with similar efforts.

Table 3.1: Estimation of expenditure of time in hours for air permeameter measurements, numerical flow simulation, and persistent homology for three different resolution steps (200, 100, and 50 µm).

Method		Preparation and processing	Measurements/ simulation/ analysis	Postprocessing	Total
Air permeameter measurements		1.0	4.8	0.2	6.0
Numerical flow simulation		7.0	< 0.1	0.1	7.1
Persistent homology analysis	200 µm	5.5	0.1	< 0.1	5.6
	100 µm	6.5	0.8	< 0.1	7.3
	50 µm	8.0	4.6	0.2	12.8

3.4 Conclusions

This study shows that persistent homology (PH) provides acceptable results for the permeability estimation of a natural bedding plane joint of a sandstone. Compared to other methods such as experimental air permeameter measurements and numerical flow simulation, it tends to slightly overestimate lower permeabilities. The overestimation of permeabilities is also traceable in previous studies using PH analysis on porous media, as well as small-scale fracture networks. For single-fracture application, a reason could be the application of the cubic law, which tends to overestimate the permeability in fracture networks or rough fractures.

In comparison to other methods, PH is a cheap and time-effective method. Once the geometry of a fracture is imaged (e.g., laser scanning, computed tomography, and structure from motion), all the tools to determine permeability are accessible and open-source. In contrast to most experimental methods, no laboratory is required to estimate the permeability. An exception to this is the air permeameter used here, which is even applicable in field experiments due to its portability. The advantages of PH compared to numerical modeling are, first, the lower required computing capacity and computing time. Furthermore, the number of parameters required to successfully perform a simulation is significantly reduced, since only the geometry is sufficient as an input parameter.

Suzuki et al. (2020) showed that small-scale (millimeter to centimeter scale) discrete fracture networks (DFNs) can be precisely studied by PH analysis. Our study demonstrates the applicability of the methods to a mesoscale (decimetre scale), rough bedding joint of Flechtinger sandstone. In order to verify these results, future work should focus on other types of fractures, such as open-mode or shear-mode fractures, as well as different lithologies, such as fractures in granites or clay. Furthermore, the influence of roughness on the flow behavior and the permeability distribution across the fracture should be investigated. In addition, a more detailed investigation of the permeabilities of different areas of this fracture could be performed on the basis of the high-resolution scans used here. This could also allow a potential scaling effect of the permeabilities to be analyzed in more detail. By combining the approach of fracture networks and rough single fractures, a long-term objective could also investigate the influence of fracture surface roughness on fracture networks at larger scales. In particular, the well-functioning subdivision of the total data set into smaller, high-resolution subpackages should allow analysis of larger DFNs without compromising the resolution. Other potential future work could be found in the comparison of such PH analysis with numerical DFN models. In addition, since numerical models for the accurate representation of fracture networks are computationally expensive, it is expected that PH is able to save time and costs.

Acknowledgements

The authors would like to thank Ruben Stemmle, Anna Albers, and Hagen Steger, for their support in conducting the air permeameter experiments, and Keiichiro Goto, for his support in performing the persistent homology analysis.

This research has been supported by the Japan Society for the Promotion of Science (KAKENHI, grant no. JP22H05108) and the Japan Science and Technology Agency, ACT-X (grant no. JPMJAX190H).

4 Permeability evolution and gouge formation during fracture shearing

Reproduced from: Fuchs, M., Blum, P., Blöcher, G., Scholtès, L. (2025): Permeability evolution and gouge formation during fracture shearing. Geophysical Research Letters 52, e2025GL117217, https://doi.org/10.1029/2025GL117217

Abstract

Hydro-mechanical processes are crucial in shear-controlled geoscientific applications such as enhanced geothermal systems and often result in stress-dependent permeability changes. The present study aims to investigate shear-induced permeability evolution of a natural sandstone fracture using a novel modeling approach. Combining a mechanical discrete element model and a hydraulic finite element model, three normal stress-related hydro-mechanical regimes can be identified. Under low normal stress conditions (< 4.0 MPa), permeability is enhanced during shearing due to dilation on intact asperities. With increasing normal stress, asperities break and gouge is formed, leading to a normal stress-related transition where permeability tends to decrease during shearing. In our study, this transition occurs when normal stress equals the rock's ultimate tensile strength (4.0 MPa). For normal stresses > 4.0 MPa, permeability decreases during shearing due to intense fracture surface damage.

Plain Language Summary

Being able to characterize fracture flow in the subsurface is essential to sustainably manage geothermal reservoirs. Previous studies have shown that fracture permeability can either increase or decrease when fractures are sheared. Using computer simulations, we studied how the normal stress influences permeability changes of a single sandstone fracture subjected to shearing. Our results highlight three different regimes depending on the normal stress applied to the fracture. At low normal stress, the fracture asperities remain intact during shearing and favor fracture opening, which induces an overall increase in the permeability. At high normal stresses, the asperities break during shearing and favor fracture closing, which produces a decrease in the

permeability. For intermediate normal stresses, a transitional regime is observed, in which permeability remains constant during shearing.

4.1 Introduction

Understanding the hydro-mechanical (HM) behavior of fractures is essential for subsurface systems such as enhanced geothermal systems (EGS), where hydraulic stimulation plays a crucial role (Amann et al., 2018). Hydraulic stimulation increases fluid pressures that reduce the effective stress and potentially enable shear slips of existing fractures (e.g., Ellsworth, 2013; Nguyen et al., 2021), which, in turn, induce permeability changes that can have drastic effects at the reservoir scale.

Empirical models can be used to correlate permeability and geometrical properties of single fractures. One fundamental model is the cubic law that relates permeability and mechanical aperture (Louis, 1969; Witherspoon et al., 1980). Since the cubic law was developed for two parallel plates, other studies tried to enhance its capability by including additional parameters in its formulation such as relative roughness (e.g., Barton & De Quadros, 1997; Renshaw, 1995), joint roughness coefficient (e.g., Barton, 1982; Olsson & Barton, 2001), or contact area (Walsh, 1981; Zimmerman & Bodvarsson, 1996). However, most of these existing models do not consider shear-related processes, such as dilation on asperities, or gouge and contact area formation (Cardona et al., 2021).

HM coupled direct shear tests (DST) are commonly used to investigate fracture permeability evolution during shearing (e.g., Frash et al., 2016; Li et al., 2023). Based on such tests, two shear-induced hydraulic regimes have been identified: (1) an opening regime associated with a permeability increase, and (2) a closing regime associated with a permeability decrease. These regimes are dependent on multiple factors, such as normal stress, surface roughness, and material properties (Fang & Wu, 2022). High-strength materials, low normal stresses, and pronounced surface roughness promote fracture opening (Fang & Wu, 2022). Thus, permeabilities of fractures in granites or marbles tend to increase during shearing (Esaki et al., 1999; Wenning et al., 2019), whereas they tend to decrease in shales (Carey et al., 2015; Fang et al., 2017), although exceptions exist (Frash et al., 2016; Li et al., 2023).

Since DST are destructive for the tested fractures, systematic studies on natural fractures are challenging. Thus, many studies have used artificial fractures (e.g., saw-cut fractures, 3D printed fractures), which, however, have only limited significance due to their specific morphology and material properties (Fang & Wu, 2022; Tatone & Grasselli, 2015). Alternatively, numerical approaches provide a relevant alternative to study such HM-coupled and progressive processes due to their flexibility and evolving capabilities. However, studies providing 3D HM coupled models to investigate permeability changes during shearing remain scarce. Most numerical studies focus either on hydraulic flow and permeability changes during shearing or on mechanical processes, such as gouge or contact area formation (e.g., Chen et al., 2021; Wang et al., 2020). Hydraulic studies have been mostly performed using continuum approaches such as the finite element method (FEM) (e.g., Auradou, 2009; Matsuki et al., 1999) and thus tend to simplify or neglect mechanical processes such as gouge formation or fracture surface evolution, since they are not able to reflect breakages of asperities.

For an advanced representation of the mechanical behavior of fractures, discontinuum approaches, such as the discrete element method (DEM), have been increasingly used due to their capacity to describe explicitly progressive failure processes. DEM models can actually simulate the evolution of fracture contact area (Lambert & Coll, 2014) or the formation of gouge material (Asadi et al., 2012; Liu et al., 2016; Wang et al., 2019, 2020). However, due to the complex representation of fluid flow in DEM models, hydraulic processes are often neglected, and permeability changes are generally determined empirically (Wang et al., 2020).

In recent years, several studies focused on detailed investigations of permeability changes related to HM processes (Chen et al., 2021; Deng et al., 2024). For instance, Li et al. (2024) developed an approach that allows a mechanical DEM model to be coupled to a hydraulic FEM simulator in order to compute permeability changes during a DST simulation. Nonetheless, although technically possible, none of these studies focused on the effect of the normal stress on shear-induced permeability changes.

Hence, the objective of this study is to investigate permeability changes of a natural sandstone fracture during shearing, considering specifically the influence of the normal stress on its evolution, using numerical experiments combining a mechanical DEM model and a hydraulic FEM model.

4.2 Materials and methods

4.2.1 Fracture sample

This study is built upon a natural bedding joint in a block of Flechtinger sandstone taken from a quarry in Bebertal, Germany (Fischer et al., 2012). Flechtinger sandstone is an oil and gas reservoir rock in the North German Basin considered for the development of EGS systems in recent years (Zimmermann et al., 2010). Thus, many previous studies investigated important HM parameters of the rock and its fractures, such as porosity, fracture and matrix permeability, fracture roughness, and grain size distribution (Blöcher et al., 2019; Cheng et al., 2020; Gutjahr et al., 2022; Hale et al., 2020; Hale & Blum, 2022; Hassanzadegan et al., 2012; Heidsiek et al., 2020; Heiland, 2003; Kluge et al., 2021). Due to the tectonic and diagenetic processes (Heidsiek et al., 2020) and superficial weathering, the fracture exhibits a low initial contact area (c.f., Appendix A1, Chapter C3).

In this study, two representative, self-affine 3D point clouds of high-resolution surface scans of the bedding joint were used (Fuchs et al., 2024a; Gutjahr et al., 2022). The extent of the bedding joint as well as the extent of the scans is 450 mm in x-direction and 120 mm in y-direction. The average resolution of these scans is 250 µm (Fuchs et al., 2024a). Due to computational constraints, the scans were cropped to a section of 50 mm × 50 mm taken from the center of the point cloud (Figure 4.1). To facilitate its numerical handling, the irregular point clouds were assigned to a regular grid and matched spatially (Fuchs et al., 2024a,b).

4.2.2 Mechanical simulation of direct shear tests

To simulate DST on the Flechtinger sandstone, we utilized the bonded particle model (BPM) proposed by Scholtès & Donzé (2013), implemented in the YADE software (Smilauer et al., 2021). First, the calibration of the BPM was required so that its mechanical properties match those of the Flechtinger sandstone. For this purpose, three standard rock experiments were conducted: (1) tensile, (2) uniaxial compression, and (3) triaxial compression tests. Subsequently, following the procedure proposed by Scholtès & Donzé (2013), the rock tests were simulated on cylindrical samples, and the interparticle parameters of the BPM were adjusted to match the experimental behavior of the Flechtinger sandstone (Appendix A1, Table S2).

After the calibration, two blocks packed with spherical particles were generated using the two fracture surface scans. To limit the computational cost, each block was packed with two layers of particles (Figure 4.1). The particles of the inner layer have an average diameter of 400 µm, reproducing the actual grain size of the sandstone (100-500 µm) to represent the fracture surface roughness. The particles of the outer layers have an average diameter of 800 µm. The ratio of the maximum to minimum particle diameters in each layer is equal to 3.

After creating the packings, the DST simulations were performed. Each test consists of two phases: 1) the normal loading phase, in which an increasing load is applied perpendicularly onto the fracture plane until the predefined normal stress is reached, and 2) the shearing phase, in which the upper fracture block is displaced at a constant velocity parallel to the fracture plane while keeping the normal stress constant and the lower block fixed. To investigate the influence of normal stress on permeability, DST simulations were conducted at six different normal stresses: 1.5 MPa, 3.0 MPa, 4.0 MPa, 4.5 MPa, 7.5 MPa, and 15.0 MPa. For all simulations, the loading rates were chosen to ensure a quasi-static response of the model (i.e., the simulated behaviors are rate-independent).

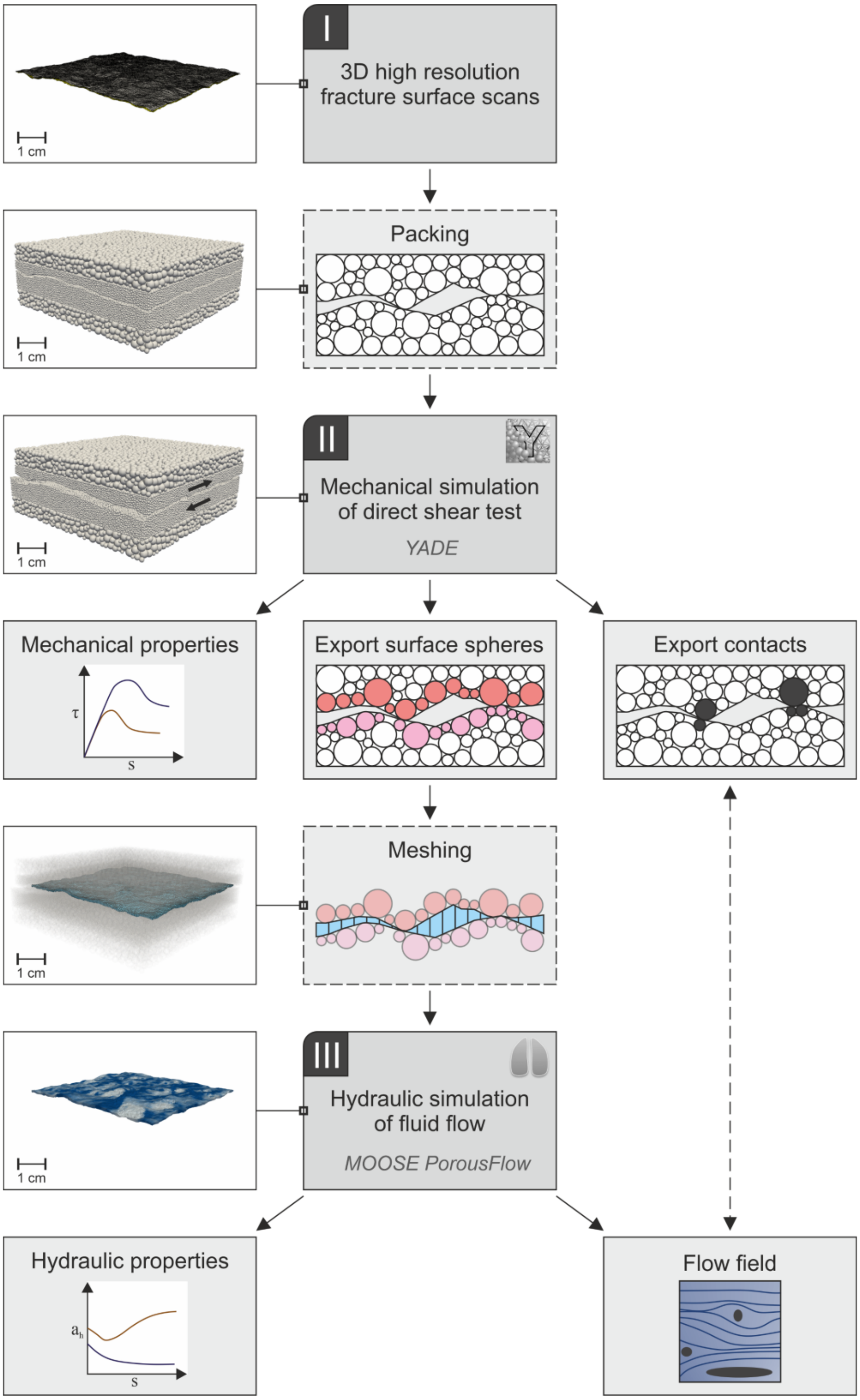

Figure 4.1: Workflow of the study with I) the sample preparation from 3D fracture surface scans, II) mechanical simulation of direct shear tests with a discrete element model, and III) hydraulic simulation of fluid flow with a finite element model.

4.2.3 Hydraulic simulation

An extension of the YADE code was developed to combine the mechanical DST simulations with hydraulic flow simulations performed with the MOOSE framework (Giudicelli et al., 2024), and the built-in PorousFlow module, which allows finite element method (FEM) simulations of flow in porous and fractured media (Wilkins et al., 2020, 2021). Since the flow simulations require a finite element mesh, the fracture surface geometry was reconstructed from the BPM. In particular, the particles forming the fracture surfaces were traced throughout the simulations so that the evolving fracture surfaces could be rebuilt at any time of the DST (every 70 µm of shear displacement here). An automatized triangulation algorithm was used to interpolate the surfaces from the particles. Then, these surfaces were used to produce a hexahedral mesh representing the fracture flow domain (Figure 4.1). It should be noted that while the detached particles (gouge) are considered in the mechanical DEM model, they were assumed to be flushed out of the fracture in the hydraulic FEM model due to the numerical representation. Thus, the permeability values computed in the presence of gouge material should be regarded as an upper limit since only the particles forming the fracture walls were considered when building the FEM mesh for flow simulations.

The mesh consists of elements with an average size of 400 µm × 400 µm, similar to the average particle size. The flow in the rock matrix was neglected, given its low permeability of 0.1-1 mD (Cheng et al., 2020; Hassanzadegan et al., 2012).

To simulate fracture flow within MOOSE, a constant hydraulic pressure gradient was applied along the fracture length. To ensure laminar flow conditions required for the application of Darcy's law, a pressure difference of 0.1 Pa was applied between the inlet and the outlet of the fracture (Zimmerman & Bodvarsson, 1996). Since the influence of flow direction was also examined in this study, flow was either applied parallel or perpendicular to the shear direction.

Once steady-state conditions were reached, the permeability was calculated using Darcy's law (Cheng et al., 2020; Zimmerman & Bodvarsson, 1996):

$$k = \frac{\mu \bar{v} L}{\Delta p} \tag{4.1}$$

where k is the permeability of the fracture [m²], μ is the dynamic viscosity of the fluid [Pa · s], $\bar{v}$ is the geometric mean of the flow velocity in the fracture [m/s], L is the length of the fracture domain [m] and Δp is the fluid pressure difference between inlet and outlet of the fracture [Pa].

4.3 Results and discussion

Based on the DST simulations results (c.f., Appendix A1, Chapter C3-4), three shear induced hydraulic regimes can be identified depending on the normal stress applied: (1) an opening regime, in which the fracture permeability is enhanced during shearing, (2) a transitional regime, in which permeability shifts from a regime of increase to one of reduction, and (3) a closing regime, in which permeability is reduced during shearing (Figure 4.2). In the following sections, each regime is discussed.

4.3.1 Opening regime

The opening regime is observed for DST performed at low normal stresses (1.5 and 3.0 MPa). Mechanically, this regime is characterized by two main characteristics: (1) after the first peak shear stress is reached, strain softening is limited and the shear stress oscillates and reaches the peak shear stress several times (Figure 4.2a), and (2) the dilation rate is maximal compared to the higher normal stress cases (Figure 4.2b). The pronounced dilation and the oscillating shear stress around the peak value result from sliding over the fracture surface asperities that do not break during the shearing process as confirmed by the small amount of gouge formed (Figure 4.3).

As a result of ongoing dilation, the mode of the mechanical aperture distribution increases from 100-200 µm at the start to > 400 µm at the end of the DST, as the distribution changes gradually from a log-normal to a Gaussian distribution. Additionally, an increase in mechanical apertures < 100 µm as well as in contact area is observed with ongoing shear displacement. This shift in mechanical apertures has also been observed in µ-CT images of shear-induced fractures in shale (Welch et al., 2022). Since the investigated natural fracture has a small initial contact area (< 2 %), the displacement of the fracture results in an increase of contact area on the shear-facing sides of the asperities. Consequently, this leads to an enlargement of mechanical apertures on the shear-opposing side of asperities, increasing the overall mechanical aperture and creating potential flow channels (Figure 4.4a).

The hydraulic response reflects this mechanical behavior since the overall permeability of the fracture increases during the DST (Figure 4.2c). Additionally, flow channeling becomes increasingly pronounced with increasing shear displacement (Figures 4.4c-f), which was also observed for flow through shear fractures in shales (Li et al., 2024; Welch et al., 2022).

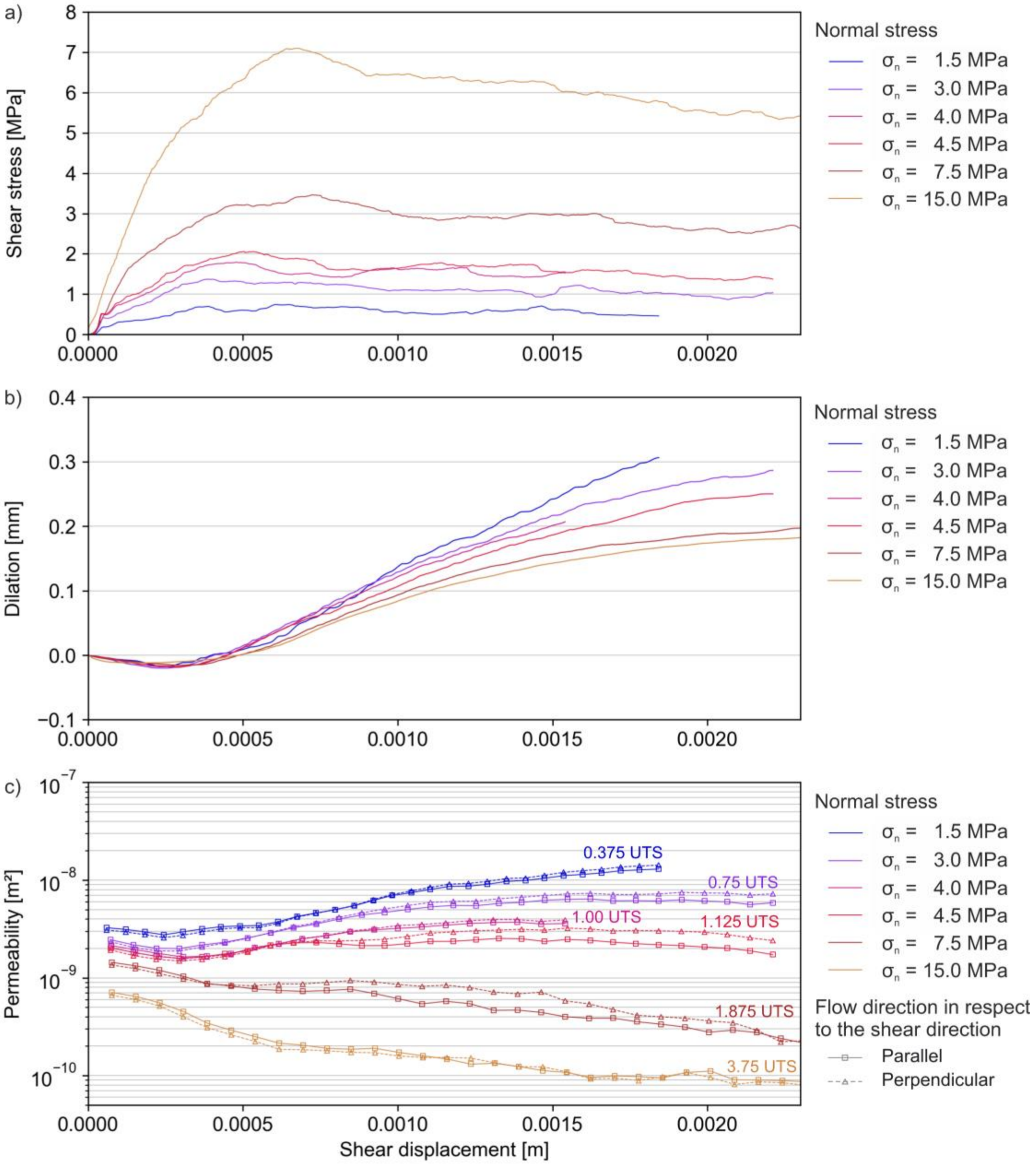

Figure 4.2: Shear displacement - a) shear stress evolution, b) dilation, and c) permeability evolution during the direct shear test for six normal stress scenarios: 1.5 MPa, 3.0 MPa, 4.0 MPa, 4.5 MPa, 7.5 MPa, and 15.0 MPa. If the normal stress exceeds the UTS (4.0 MPa), dilation and permeability are significantly decreased.

Based on these observations, the following conclusions can be drawn: the fracture opens mainly due to mechanical dilation on intact asperities. Interestingly, the associated increase in contact area does not result in a reduction of permeability (Figure 4.3). This result is in contrast to previous findings showing that permeability tends to increase when contact area decreases during shearing (Barton et al., 1985; Chen et al., 2000).

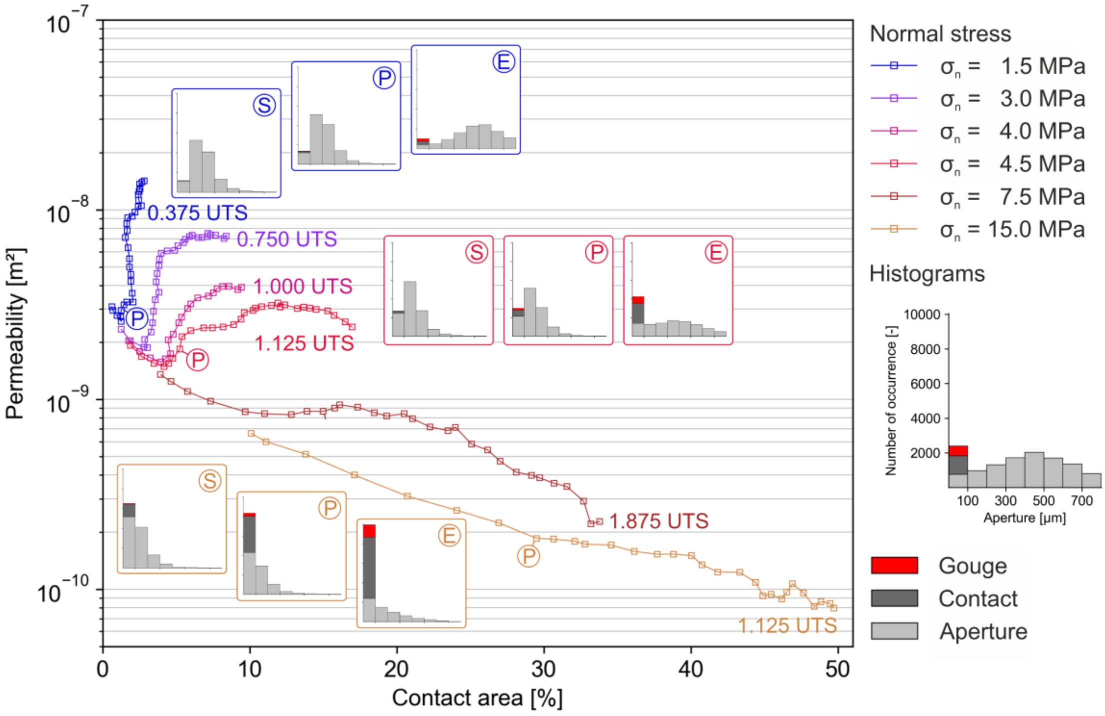

Figure 4.3: Permeability evolution (parallel to flow direction) and contact area during shearing with increasing normal stresses. Three curves are accompanied by three histograms showing the mechanical aperture distribution at the start (S), the peak shear stress (P), and the end (E) of each direct shear test. The color of the bars in the histogram indicates whether a cell in the hydraulic mesh is open (light grey), closed (dark grey), or would be filled with gouge (red).

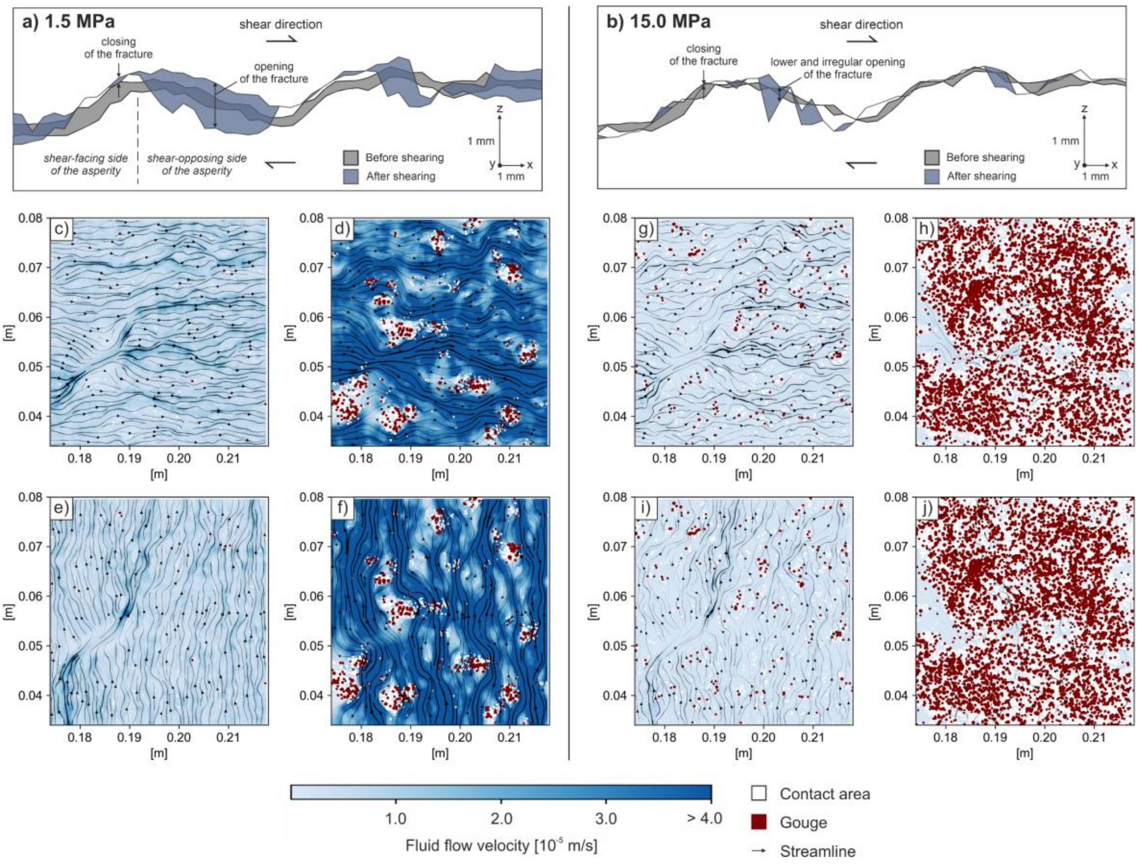

Figure 4.4: Results for normal stresses of 1.5 MPa (left) and 15.0 MPa (right). a) and b) Cross-section of the fracture before (grey) and after shearing (navy). c)-j) 2D flow fields with major streamlines (black arrows), contact area (white), and gouge (red) of the flow parallel to the shear direction before (c,g) and after shearing (d,h), as well as perpendicular to the shear direction before (e,i) and after shearing (f,j). The enlargement of major flow paths can be seen in d) and f). The hydraulic closing due to increasing contact areas and gouge is illustrated in h) and j).

4.3.2 Transitional regime

At normal stresses > 4.0 MPa, a transition from the above-described opening regime to a closing regime occurs (Figure 4.2c). The amount of gouge material and contact area increases significantly during shearing (Figure 4.3), leading to the closing of the main flow paths and to permeability reduction. Gouge material is formed from broken surface asperities (Gill et al., 2021). To characterize gouge formation, we analyzed the breaking modes of the bonds forming the BPM (Appendix A1, Chapter C2) and observed that more than 99 % of all cracks are tensile cracks (mode I) and only less than 1 % of all cracks are shear cracks (mode II). This indicates that the breaking of fracture asperities is governed by shear-induced local tensile stresses. Remarkably, it is observed that the normal stress at which the permeability transitions from an increasing to a decreasing regime corresponds to the ultimate tensile strength (UTS) of the rock matrix (4.0 MPa). Previous studies have shown relationships between mechanical parameters and permeability (Deng et al., 2024; Gutierrez et al., 2000; Makurat et al., 1997; Milsch et al., 2016). Of particular interest are the studies by Makurat et al. (1997) and Gutierrez et al. (2000), which pointed out that the hydraulic transition occurs when the effective normal stress exceeds the UCS of the rock matrix they tested (a shale). However, while their results clearly highlight the fact that fracture permeability drastically decreased during shearing for normal stresses higher than the UCS value, the transition from an opening to a closing hydraulic regime seemed to be reached at lower normal stresses when reanalysing their data (approximately 2 MPa). Unfortunately, the authors did not report the UTS of the rock they tested, and, at this point, we can only acknowledge that further investigations are required to state a representative threshold value for the transitional regime.

The increase in contact area related to fracture surface damage lead to additional changes in hydraulic properties, specifically in terms of flow anisotropy. This occurs in the DST at 3.0 MPa normal stress, as well as for the DST at 4.5 and 7.5 MPa normal stresses (Figure 4.2c). Due to transpression in shear direction, the permeability anisotropy (PA) $k_{\perp}/k_{//}$ is > 1.2 with a peak anisotropy of $k_{\perp}/k_{//} = 1.6$. Similar observations on PA during shearing were observed in previous experimental studies (Auradou et al., 2005; Yeo et al., 1998), performed on digital synthetic fracture models (Matsuki et al., 1999) or numerically (Auradou et al., 2005; Li et al., 2024). Besides, gouge material also has a decisive influence on permeability, since it reduces dilation or clogs major flow paths, and, therefore, reduces mechanical apertures in the fracture (Gill et al., 2021; Li et al., 2023). However, many studies, especially numerical studies, do not consider gouge formation (e.g., Egert et al., 2023; Welch et al., 2022).

4.3.3 Closing regime

For normal stresses exceeding the transition threshold of 4.0–4.5 MPa, the fracture is governed hydraulically by a closing regime during shearing (Figure 4.2c). Mechanically, this regime is characterized by a distinct peak shear stress and strain softening toward a residual state (Figure 4.2a). This behavior can be explained by the formation of a large amount of gouge associated to an increase of contact area (Figure 4.4b). Up to 50 % of the fracture is closed by gouge particles or contacts (Figure 4.3). This is also reflected in the mechanical aperture distribution. The initial log-normal distribution is shifted to a logarithmic distribution with the mode < 100 µm (Figure 4.3). The fracture is not just closed on the shear-facing sides of asperities, but also, in contrast to the opening regime, on the shear-opposing side (Figure 4.4b). Due to high normal and shear stresses, tensile cracks form in and around these asperities, promoting damage in the surrounding rock matrix and therefore producing even more gouge particles (Liu et al., 2016).

Hydraulically, the breakage of asperities and the associated increase of contact area lead to a total mechanical closure of all major flow paths during the DST, leaving only secondary flow paths open (Figure 4.4g-j), and limiting flow anisotropy (Figure 4.2c). This hydraulic closure of the fracture is, therefore, mainly due to fracture surface damage instead of the pure vertical compaction of two fracture surfaces, as previously observed by Li et al. (2024).

A crucial assumption of our BPM approach is that gouge material results from the detachment of the particles (either isolated or clustered in aggregates) forming the fracture walls, and that these particles are unbreakable. Since the sample mainly consists of quartz grains, such an assumption is acceptable at normal stresses up to 15 MPa. Nonetheless, it should be noted that, depending on material properties or alteration processes, actual gouge particles may break under high-stress conditions or large shear displacements (Fang & Wu, 2022; Li et al., 2023), and may have a significant effect on fracture closure (Zhao, 2013).

4.4 Conclusions

In this study, the hydro-mechanical behavior of a single sandstone fracture subjected to direct shear tests was investigated for normal stresses ranging from 1.5 to 15.0 MPa. A combined numerical approach (DEM and FEM) was designed to characterize fracture permeability changes during shearing. Our results indicate that three normal stress-related hydraulic regimes can be distinguished: (1) an opening regime at normal stresses between 1.5 MPa and 3.0 MPa, (2) a transitional regime at around 4.0 – 4.5 MPa, and (3) a closing regime for normal stresses > 4.5 MPa. These regimes can be characterized as follows:

(1) In the opening regime, dilation on intact asperities governs the fracture behavior, and gouge and contact area formation are negligible. In this regime, permeability increases with increasing shear displacement since existing flow paths are enlarged.

(2) In the transitional regime, increasing gouge formation and contact area start to affect the flow behavior of the fracture. This leads to high flow anisotropy, since gouge particles aggregate parallel to the shear direction and clog the flow in this direction, whereas perpendicular flow paths are kept open.

(3) In the closing regime, significant asperity breakages form large amounts of gouge and contacts between the fracture surfaces. This results in less but still significant dilation on gouge particles. Hydraulically, existing flow paths close, and permeability is reduced.

Conclusively, all three regimes can occur in deep reservoirs depending on the rock material properties and in situ stress levels. For instance, according to our study, the transition to a closing regime would correspond to a depth of around 300 m for Flechtinger sandstone. Assuming long-term permeability enhancement after hydraulic stimulation should therefore be scrutinized in the context of geothermal projects realized in greater depths and stresses, since the lack of permeability can lead to shear-slip events and induced seismicity (Gaucher et al., 2015), as observed in Strasbourg in 2019/2020 (Schmittbuhl et al., 2022) and in Pohang in 2017 (Li et al., 2024). Nonetheless, it should be noted that these findings are based on a small-scale fracture and numerical simulations. To address this important limitation, future studies should aim for experimental validation of the present findings. Extrapolations to geothermal systems should also consider scale effects and fracture network connectivity and orientation. Furthermore, more sophisticated numerical models and larger-scale experiments are necessary on reservoir scale. Thus, further studies should focus on two key aspects: First, detailed small-scale hydro-mechanical models should be established to enable an exact representation of governing processes, especially gouge formation, on the HM behavior during shearing. Second, methods should be developed to upscale small-scale results to reservoir scale. This includes the validation of such methods using laboratory and large in-situ experiments in underground research laboratories.

Acknowledgements

The authors thank Christian Kluge and Liang Pei for conducting the rock tests for model calibration. Marco Fuchs was supported by the Karlsruhe House of Young Scientists (KHYS) and the InVolc Graduate Track of the Université Clermont Auvergne. This work benefited from the French government initiative "programme d’investissements d’avenir" managed by the Agence Nationale de la Recherche (ANR) under grant ANR-20-SFRI-0003 project CAP GS. The authors would like to acknowledge the constructive comments made by the two reviewers, which helped to improve this manuscript.

5 Synthesis

5.1 Conclusions

The permeability of natural single fractures, although governed by sub-millimeter processes, is a crucial parameter for the feasibility of many larger-scale applications, such as geothermal energy production or nuclear waste disposal. Thus, this thesis presents various methods aimed at improving the characterization of natural single-fracture permeability. It explicitly addresses different stages of this process, starting with preparatory steps (i.e., imaging and spatial matching of fracture surfaces), followed by methods for determining permeability, and concluding with the evolution of fracture permeability under changing mechanical conditions. Consequently, the main findings of the thesis presented in Chapters 2 – 4 are summarized in the following sections.

i) Preparation – Surface imaging

A wide range of methods and devices is available for imaging of fracture surfaces. In Study 1 (Chapter 2), three of them were applied to a natural single fracture in a Flechtinger sandstone block to evaluate suitable approaches to generate the geometrical basis of numerical flow simulations. The study shows that resolution and accuracy of each method are the governing parameters that decisively impact not only the fracture surface scan quality, but subsequently also the permeability estimation and flow distribution.

Approaches exhibiting low resolution and accuracy, represented by a handheld laser scanner (HLS) in Study 1 (Chapter 2), are unable to image the fracture surfaces adequately. In contrast to more accurate methods, such as the mounted laser scanner (MLS) and Structure from Motion (SfM), the asperities were imprecisely reproduced, and key structures (e.g., barite vein) were not represented in the scan. Consequently, this was also underlined by the accuracy-resolution ratio (ARR), for which the HLS shows a respective value of approximately 63 %, far exceeding the benchmark of 5 % proposed by Tatone & Grasselli (2012).

In contrast, approaches exhibiting higher resolution and accuracy, such as MLS and SfM, can image the fracture surface in high quality and, therefore, provide a solid basis for numerical flow domain geometry. However, the two methods exhibit differences attributable to their respective accuracies. The lower single point accuracy (35 µm) of SfM compared to MLS (10 µm) results in slightly less accurate spatial location of scanned points. Subsequently, this leads to increased surface roughness and increased mechanical apertures. Study 1 (Chapter 2) shows that this directly impacts the flow distribution in fractures, leading to higher determined permeabilities and more pronounced preferential flow paths.

Further results of the study show that the hydraulic apertures of the performed numerical flow simulation (MLS: 163 µm, SfM: 207 µm) do not fit the average hydraulic aperture determined by the experimental air permeameter measurements (81 µm). However, assuming an initial contact area of the fracture, it is found that the hydraulic aperture is reduced (MLS: 85 µm, SfM: 83 µm), and the air permeameter value can be matched at 5 % (MLS) and 7 % (SfM) contact area, respectively. Although these results demonstrate the influence of the contact area, they also highlight the limitations of two-dimensional numerical flow simulations.

Despite the lower resolution and accuracy of SfM compared to MLS, and the resulting limitations in flow simulations, it becomes evident that SfM can still play a significant role considering acquisition costs, adaptability to varying scales or conditions, and mobility. Particularly in field applications or for fracture imaging across multiple scales, SfM may serve as a valuable alternative to MLS and other stationary, high-resolution systems.

ii) Analysis - Persistent Homology

However, since the geometry of the fracture was best imaged by MLS in Study 1 (Chapter 2), this geometry was selected for the application of the topological persistent homology (PH) analysis to estimate the single fracture permeability. This method was already successfully implemented to predict the permeability of small-scale discrete fracture networks (DFN) as well as porous media. However, characterizing individual fractures while accounting for surface roughness presents a particular challenge, as the scale of many fractures (decimeter scale) differs significantly from that of asperities (micrometer scale). Thus, in Study 2 (Chapter 3), PH was applied to the natural single fracture and evaluated against conventional methods, including air permeameter measurements and numerical flow simulations.

The results in Study 2 (Chapter 3) indicate that permeability can be predicted using PH analysis with a level of accuracy comparable to that of established validation methods. The hydraulic apertures estimated with PH range between 73 µm and 92 µm, similar to the air permeameter measurements (81 µm) and the calibrated numerical flow simulation (85 µm).

Besides the general estimation of fracture permeability with PH, the study examined the influence of different data set resolutions (200 µm, 100 µm, and 50 µm) on fracture permeability. The study shows that all resolution scenarios result in comparable values without significant outliers. Despite this, analysis of the normalized root mean squared error (NRMSE) of the results reveals that increased resolution is associated with reduced error, suggesting a clear dependency of PH analysis accuracy on spatial resolution.

Nonetheless, increasing spatial resolution is accompanied by an exponential increase in computational time. A comparison of datasets with varying resolutions and the applied validation methods reveals that PH analysis remains comparable to air permeameter measurements and numerical flow simulation at resolutions of 200 µm and 100 µm. However, enhancing the resolution from 100 µm to 50 µm increases the total expenditure of time by 75 %. Thus, considering both error and computational effort, the dataset with a resolution of 100 µm emerges as a promising alternative to conventional methods.

iii) Shearing - Permeability evolution under normal and shear stress

Study 3 (Chapter 4) illustrates how permeability can evolve under varying confining and shear stress conditions. To quantify this behavior, simulations of direct shear tests (DST) were conducted under normal stresses ranging from 1.5 MPa to 15.0 MPa, using a novel approach combining a mechanical DEM model and a hydraulic FEM model. This approach enables the investigation of mechanical processes such as gouge formation or dilation, without neglecting the impact on hydraulic processes.

The generated data show that the evolution of fracture permeability is primarily governed by the normal stress controlling the main mechanical processes during shearing. Based on this finding, three normal stress-related regimes are divided in Study 3 (Chapter 4):

- **Opening regime:** The fracture opens mechanically with increasing shear displacement due to dilation of the upper fracture surface under low normal stress conditions. Subsequently, this process leads to widening of existing flow paths and the enhancement of permeability.
- **Transitional regime:** Asperities on the fracture surfaces start to break under increasing normal stress, resulting in a constant permeability during the entire DST.
- **Closing regime:** The fracture hydraulically closes as asperities break and the main flow paths become obstructed by gouge material generated during shearing under high normal stress conditions. Mechanically, dilation is still ongoing, increasing the distance between the fracture surfaces, but not the mechanical aperture.

Particularly interesting is the threshold value at which the regime changes from an opening to a transitional regime, since this marks the normal stress after which permeability no longer increases due to shear displacement along the fracture. For the investigated Flechtinger Sandstone, this threshold was observed to be 4.0 MPa, corresponding to the ultimate tensile strength (UTS). However, further research is required to establish a connection between the UTS and the transitional regime.

Reflecting on the overarching goal of this thesis – the advancement and refinement of methodological approaches for characterizing the permeability and fluid flow behavior through single fractures – it was possible to develop a cost-effective open-source workflow. This workflow enables rapid yet detailed investigation of single-fracture permeability.

5.2 Perspectives and outlook

This thesis confirms the applicability and validity of novel methods and approaches in the scope of permeability characterization of natural single fractures. Although a broad range of topics is covered, there is still potential for further research and optimization. Based on the findings of this thesis, this chapter is divided into two parts. The first part focuses on detailed investigations of the underlying hydro-mechanical processes at the same or a smaller scale. The second part of the chapter addresses approaches enabling the upscaling of the presented results to a larger scale.

5.2.1 Detailed analysis

i) Transfer to other lithologies and scales

A significant limitation of the studies included in this thesis is their dependence on a single fracture sample taken from a sandstone block at the laboratory scale. While this enables a detailed and sequential investigation of HM processes, it simultaneously limits the transferability of the results to other lithologies or scales. Although the sandstone used in this study represents a rock with typical mechanical properties, future research should focus on weaker rocks (e.g., shale) and stronger rocks (e.g., granite) to allow for validation of the HM results obtained in this thesis.

Furthermore, the investigation of single fractures across different scales remains a well-known yet unresolved research question (Viswanathan et al., 2022). While partial studies exist, e.g., on fracture roughness across multiple orders of magnitude (Candela et al., 2012), a holistic understanding of HM processes from the sub-micrometer scale to the kilometer scale within a single fracture or fault is still lacking. However, the rapid development of computational power is expected to enable significant progress in this field of research in the coming years.

ii) Mechanical contact model

Transferring the methods presented in this thesis to other lithologies would require a critical examination of contact mechanics. For all mechanical results shown in this thesis, fully elastic conditions were assumed. In Study 3 (Chapter 4), a fully elastic interpenetration model integrated into the YADE DEM code is used, which allows two spheres to overlap, with the stiffness being adjusted accordingly (Smilauer et al., 2021). In contrast, Study 1 (Chapter 2) generates contacts between the two fracture surfaces only by vertically compressing the surfaces, setting overlapping regions to zero. While this latter method enables precise control over the relative contact area, it neglects the actual contact mechanics. Thus, a comparison with other contact mechanical approaches, such as the Hertzian/Greenwood-Williamson method (Greenwood & Williamson, 1966) or the Fast Fourier Transform approach (Kling et al., 2018), is essential for future studies. This is particularly relevant for mineral compositions, where plastic deformations must also be considered (i.e., shale).

iii) Implementation of three-dimensional Navier-Stokes flow simulations

The results of Studies 1 and 2 (Chapters 2 and 3) demonstrate that flow simulations can be conducted using 2D models, yielding plausible outcomes. However, it should be noted that this approach involves certain simplifications and assumptions, such as projecting the geometry onto a two-dimensional plane and employing Darcy's law to solve the partial differential equation. Previous studies have shown that the accuracy of permeability estimation of such simulations is highly influenced by the Reynolds number (Egert et al., 2021). At high Reynolds numbers (i.e., high flow rates), the simulated flow velocities tend to be elevated compared to validation methods. Consequently, the implementation of Navier-Stokes solvers and the use of 3D geometries are particularly beneficial in cases of high surface roughness or elevated flow velocities.

Although many studies already employ 3D simulations to model fluid flow through fractures (Egert et al., 2021; Marchand et al., 2020; Stoll et al., 2019), it must be noted that this approach involves significantly higher computational effort. In particular, simulating multiple scenarios, as presented in Study 3 (Chapter 4), would increase computational time by several orders of magnitude compared to 2D simulations.

iv) Experimental validation of direct shear test simulations

The results of Study 3 (Chapter 4) enable significant progress in characterizing the hydraulic behavior of individual fractures under normal and shear stress. However, these findings are entirely based on numerical simulations of a DEM and FEM model. Although this enables a powerful approach to investigate HM processes in a single fracture, it lacks experimental validation. Multiple studies have already presented experimental setups, which are able to effectively couple mechanical DST with hydraulic fluid flow through the sample (e.g., Kluge et al., 2021; Li et al., 2023). Although processes such as gouge formation have already been studied in this context (Li et al., 2023), the experimental validation of a transition from an opening to a closing regime remains unresolved. A critical next step should therefore be the transfer of the simulations described in this thesis to experimental investigations, in order to validate the conclusions drawn in Study 3 (Chapter 4).

iv) Coupling of hydro-mechanical simulation

Various studies show the importance of coupling THMC processes in fractures for an adequate and realistic representation of a single fracture (Viswanathan et al., 2022). In this thesis, HM processes during normal loading and shearing are considered. As mentioned in the last section, these processes can already be investigated fully coupled under experimental conditions (Vogler et al., 2016; Welch et al., 2022). However, numerical investigations are not able to represent mechanical processes (i.e., gouge formation, dilation, contact area) and hydraulic processes in a coupled HM workflow yet. The results of Study 3 (Chapter 4) represent a significant advancement toward enabling fully coupled hydro-mechanical (HM) modeling for shear tests, achieved through the combined approach of a mechanical DEM model and a hydraulic FEM model of the fracture. Nevertheless, as in the approach presented by Li et al. (2024), only a one-way coupling of mechanical changes to hydraulic flow is possible in this study. A fully bidirectional coupling is not yet achievable.

Thus, future research should focus on two main directions: first, exploring possibilities for bidirectional coupling between DEM and FEM, allowing hydraulic changes to directly influence mechanical behavior. Second, the implementation of a fluid phase within a purely DEM-based model could also be considered. However, to realize such a highly detailed modeling approach, a substantial increase in computational power would be required.

5.2.2 Upscaling

The results presented in this thesis focus on a small-scale single fracture (centimeter to decimeter scale). However, all commercial applications are either working on full reservoir size or at least on fracture network scale (meters to kilometers). This necessitates an upscaling of the detailed results obtained at the centimeter scale. A particularly relevant factor in this context is the consideration of fracture roughness, which has a significant impact on both mechanical (i.e., gouge formation, dilation) and hydraulic behavior (i.e., preferential flow paths, clogged flow paths), but is not considered in most large-scale studies. In previous studies, fractures at larger scales have been represented mainly as planar surfaces or modeled using a porous equivalent for the combined matrix and fracture permeability. Thus, future research should focus on integrating roughness-dependent hydro-mechanical information into larger-scale investigations.

Study 2 (Chapter 3) has demonstrated that, using topological methods, it is indeed possible to upscale detailed small-scale analyses to larger scales. The effective partitioning of the domain into smaller subdivisions and the determination of permeability for each of these smaller units did not result in degradation of the estimated permeability compared to validation methods. Consequently, this approach represents a promising method for incorporating small-scale effects into larger-scale geometries.

Since permeability estimations of fracture networks with planar fractures are already available (Suzuki et al., 2021), the results obtained in Chapter 3 could serve as a basis for combining the two approaches and determining the permeability of fracture networks with PH while accounting for surface roughness.

Another critical aspect in upscaling results from individual fractures to fracture networks is the hydro-mechanical behavior at the intersections of two fractures. The exact geometry can have a significant impact on the overall permeability of a fractured system (Pyrak-Nolte et al., 2023; Viswanathan et al., 2022). Thus, future research should aim to incorporate the geometry of these junctions and assess their influence on flow patterns.

Appendix

A1 Supporting Information Study 3

This appendix refers to Study 3 (Chapter 4). The content is published in the journal Geophysical Research Letters (GRL) as supporting information.

Introduction

The supporting information contains three chapters C1 – C3 providing additional information to the three sections of the "Material and methods" chapter in the main manuscript. Furthermore, the chapter C4 provides definitions about mechanical and hydraulic parameters to describe fracture aperture. In addition, the Figures S1-S3, as well as the Tables S1-S3 supporting chapters C1 – C3 are shown in this file.

C1 Additional Information to the Fracture Sample

The sandstone sample in this study is Flechtinger sandstone. The sample was taken from a quarry in Bebertal, Saxony-Anhalt, Germany, and is part of the Northern Germany Basin (Fischer et al., 2012). Flechtinger sandstone was already part of multiple previous studies, whereas many mineralogical, chemical, hydraulic, and thermal characteristics of the rock, as well as the fractures within, are well known (Cheng et al., 2020; Fischer et al., 2012; Hassanzadegan et al., 2012, 2014; Heidsiek et al., 2020). Of particular interest are the studies of Hale et al. (2020), Hale & Blum (2022), Fuchs et al. (2024a), Fuchs et al. (2024b), and Gutjahr et al. (2022), in which the exact same fracture sample is studied. Gutjahr et al. (2022) proved self-affinity of the fracture and determined the Hurst exponents to examine the roughness of the fracture surfaces. The median of all calculated Hurst exponents in x-direction is 0.48. The Hurst exponents in y-direction are slightly lower (0.42). The studies of Hale et al. (2020), Hale & Blum (2022), Fuchs et al. (2024a), and Fuchs et al. (2024b) all determined the permeability of the fracture with different methods and in different directions. The derived permeabilities are displayed in Table S3.

C2 Simulation of Direct Shear Tests

The open-source code YADE was used to simulate direct shear tests. YADE is based on the discrete element method (DEM). Thus, the rock is represented as a packing of bonded spherical particles (or discrete elements, DE). YADE works similarly to DEM algorithms in two steps: 1) the interaction forces are calculated between the DE based on their relative position and the predefined contact law, and 2) the acceleration of each DE is calculated based on Newton's second law of motion. The acceleration is then time-integrated to determine the new position of each DE. The entire process is repeated iteratively until the end of the simulation.

In the present study, we used an elastic-brittle contact law that has proven to be effective for simulating rock-like materials (Scholtès & Donzé, 2013). The interaction force F_{int} represents the interaction between DE a and DE b and consists of a normal component F_n and a shear component F_s. These components are related to the relative normal and incremental shear displacements through the normal and shear stiffnesses K_n and K_s, respectively. F_n is calculated by the local constitutive law presented in Figure S1. Under compressive loading, F_n is computed as

$$F_n = K_n \Delta D F_{int} \tag{C2.1}$$

where, ΔD is the relative displacement between interacting DE, and K_n is defined by

$$K_n = E_{eq} \frac{R_a R_b}{(R_a + R_b)} \tag{C2.2}$$

in which E_{eq} is a bulk modulus equivalent, R_a is the radius of DE a, and R_b is the radius of DE b.

Under tensile loading, F_n is computed as in equation (1) up until the maximum tensile force, $F_{n,max}$ is reached:

$$F_{n,max} = -tA_{int} \tag{C2.3}$$

where t is the tensile strength, *and* A_{int} is the interacting surface between DE a and DE b expressed by

$$A_{int} = \pi * (\min(R_a, R_b))^2 \tag{C2.4}$$

When F_n exceeds $F_{n,max}$, a tensile rupture occurs (mode I) and the interaction force is set to 0.

F_s is computed in an incremental manner by updating its orientation and intensity depending on the increment of shear force $\Delta F_s = K_s \Delta u_s$, which develops at the interaction point (as proposed by Hart et al., 1988):

$$F_s = \{F_s\}_{updated} + K_s \Delta u_s \tag{C2.5}$$

with K_s proportional to K_n, and Δu_s the relative incremental tangential displacement.

As illustrated in Figure S2, the maximum shear force $F_{s,max}$ is expressed as

$$F_{s,max} = F_n \tan \varphi_b + cA_{int} \tag{C2.6}$$

where φ_b is the friction angle for bonded contacts, and c the cohesion. When F_s exceeds $F_{s,max}$, a shear rupture occurs (mode II), and the initially bonded interaction becomes purely frictional.

Similarly, if new contacts between two DE are detected during the simulation, they are also treated as purely frictional with a maximum shear force $F_{s,max}$ calculated as:

$$F_{s,max} = F_n \tan \varphi_r \tag{C2.7}$$

with φ_r is the residual friction angle.

In addition, the DEM formulation being fully dynamic, a local non-viscous type damping is used to dissipate kinetic energy and favor the quasi-static response of the model (please see details in Duriez et al., 2016). All simulations in this study were performed with a damping coefficient of 0.5.

Finally, a specificity of the BPM used in this study relies on the possibility for near neighbor interactions between DE. As discussed by Scholtès & Donzé (2013), this feature provides a simple yet effective approach to better reproduce the brittleness of rock like materials (i.e., high UCS/UTS ratios and nonlinear failure envelopes). In the present study, we defined an interaction range coefficient γ_{int} = 1.14 that allows to properly reproduce the behavior of the Flechtinger sandstone as shown in Table S1 (bonds are created between DE if their center to center distance is inferior to $\gamma_{int}(R_a+R_b)$).

C3 Hydraulic Simulation

The open-source, parallel finite element Multiphysics Object Oriented Simulation Environment (MOOSE) framework was used to perform fluid flow simulations in the fracture (Giudicelli et al., 2024). The MOOSE framework includes different physics modules and applications. In this study, the Porous Flow module was used (Wilkins et al., 2020, 2021). Porous Flow is able to solve fluid and heat flow problems with an arbitrary number of phases and fluid components. Here, it is used to simulate single phase fluid flow under saturated conditions. In general, Porous Flow solves the continuity equation of mass conservation for κ fluid species:

$$0 = \frac{\delta M^{\kappa}}{\delta t} + M^{\kappa} \nabla \cdot v_s + \nabla \cdot F^{\kappa} + \Lambda M^{\kappa} - \phi I_{chem} - q^{\kappa} \tag{C2.8}$$

M is the mass of fluid per bulk volume, v_s is the velocity of the porous solid skeleton, F is the fluid flux, Λ is a radioactive decay rate, ϕI_{chem} is the chemical precipitation or dissolution and q is a source or sink term of fluid. In this study, no chemical reactions, radioactive decay, nor a fluid source or sink are present. In addition, there is no consideration of solid mechanics within the fluid flow simulation and, therefore, no change in fluid mass per bulk volume nor movement of the porous solid skeleton. Consequently, Equation 9 can be reduced to the term of fluid flux, which can be represented as

$$F^{\kappa} = \sum_{\beta} \chi_{\beta}^{\kappa} F_{\beta}^{advective} + F_{\kappa}^{diff+disp} \tag{C2.9}$$

with the mass fraction χ of component κ in phase β. $F^{advective}$ is the advective flux component of phase β and $F^{diff+disp}$ is the diffusive-and-dispersive flux component of each fluid component κ. Since only one component and one phase are considered in this study, this reduces to the advective flux term, which is expressed by Darcy's law:

$$F^{adv} = \rho v = -\rho \frac{k}{\mu} (\nabla \mathrm{p} - \rho g) \tag{C2.10}$$

ρ is the density of the fluid phase, v is the Darcy velocity, k is the permeability, μ is the viscosity, p is the pore pressure and g is the gravitational constant. It should be mentioned that since Darcy flux is used in this study, the assumption of laminar flow has to be made. To ensure laminar flow, a small pore pressure gradient of 2 Pa/m was chosen as boundary condition in all of the performed simulations. Furthermore, an initial permeability value had to be assigned to the flow domain to simulate Darcy flux. Thus, a permeability value based on the local mechanical aperture was assigned to each mesh element in the flow domain using the local cubic law.

The FEM flow domain of the hydraulic model also allows a detailed calculation of contact area. The FEM mesh is generated in the interstitial space between the two fracture surfaces exported from the DEM model, which were subsequently interpolated onto a regular grid. The relative contact area $A_{c,r}$ is then calculated based on the mesh elements N_c with a mechanical aperture of $a_m = 0$ and the total number of mesh elements N (Deng et al., 2024):

$$A_{c,r} = \frac{N_c}{N} \tag{C2.11}$$

C4 Definition of mechanical and hydraulic parameters

Dilation is defined as the change of the mechanical distance between the averaging planes of the two fracture surfaces (Fang et al., 2017). Accordingly, the mechanical aperture is the measurable distance between the two fracture surfaces perpendicular to the averaging plane of each fracture surface (Vogler et al., 2018). In contrast, the hydraulic aperture, which is directly related to the permeability using the Cubic Law (Witherspoon et al., 1980), is the hypothetical aperture used for fluid flow through the fracture assuming a parallel plate model.

Following this definition, dilation is a global value representing the entire fracture domain, whereas mechanical aperture is a local parameter. Due to the formation of gouge or contact area, these two mechanical parameters are not necessarily coupled to the hydraulic aperture/permeability (Fang et al., 2017; Li et al., 2023).

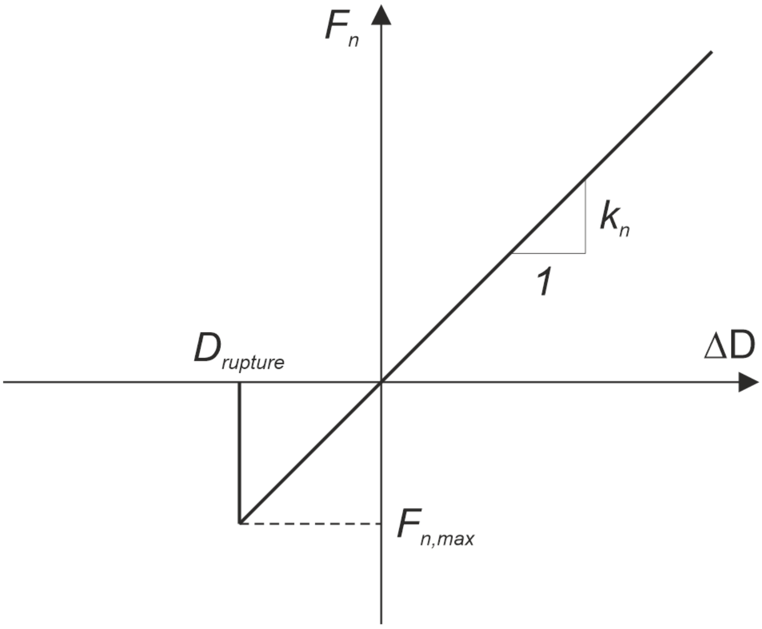

Figure S1: Normal interaction force between DE.

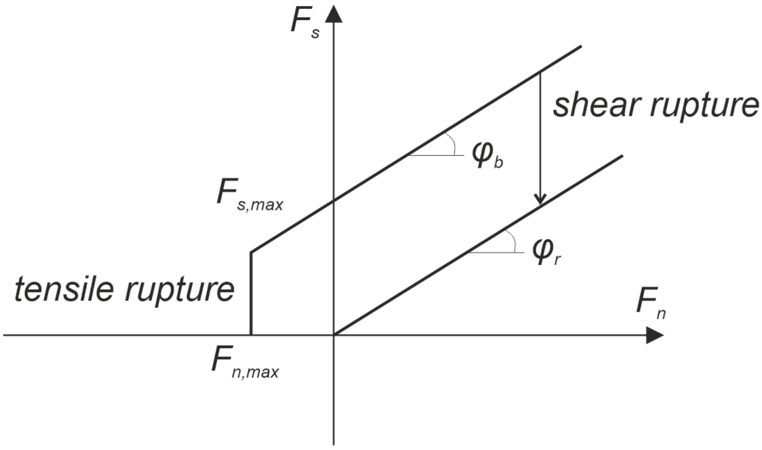

Figure S2: Rupture criterion used in the DEM model.

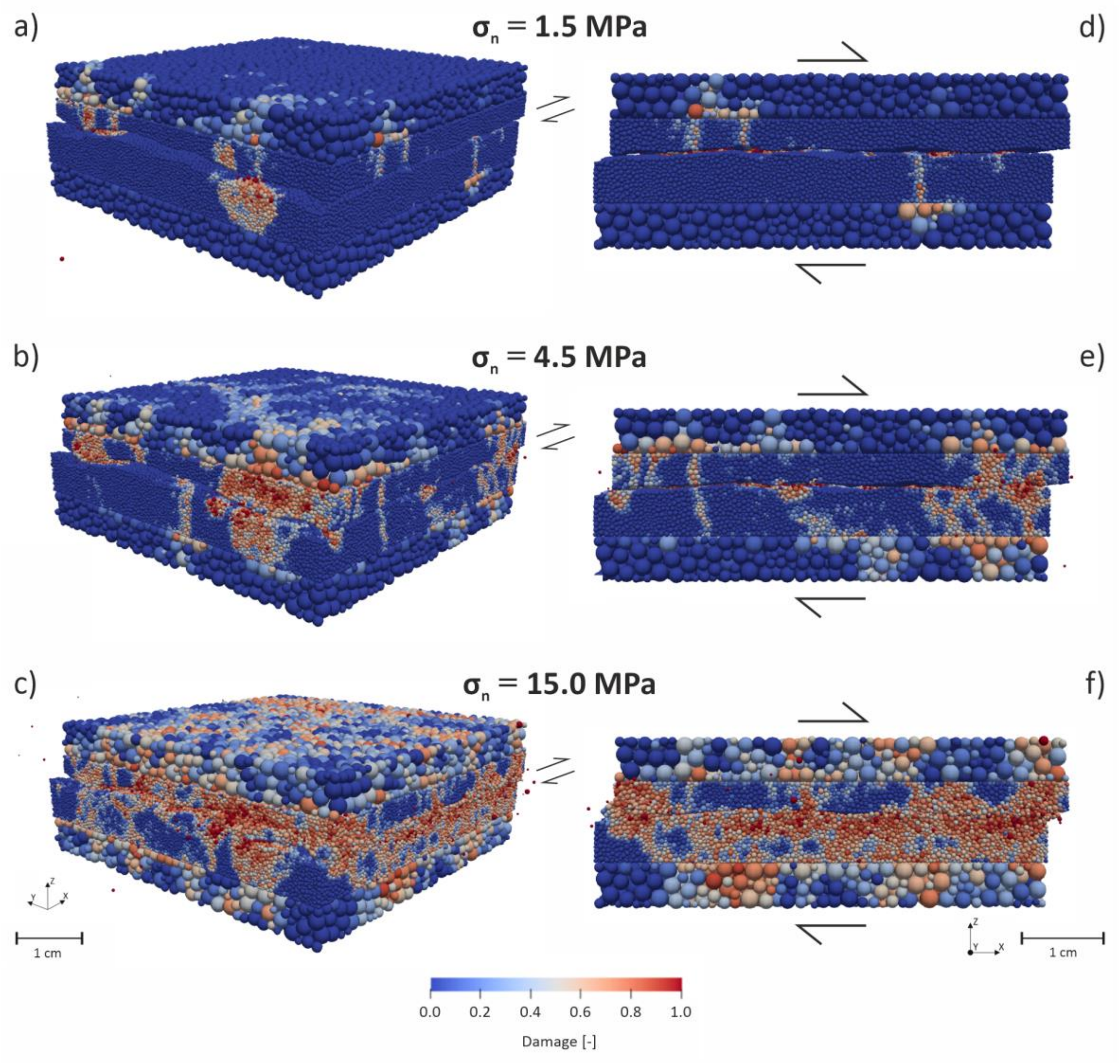

Figure S3: Results of the direct shear tests in 3D (a-c) and 2D (d-f). The state of the BPM model after the end of shearing is shown for three scenarios: 1.5 MPa (a, d), 4.5 MPa (b, e), and 15.0 MPa (c, f) normal stress. The displayed damage value ranges between 0 and 1 and reflects the relative proportion of broken interactions of each discrete element (DE). At a damage value of 1, the DE is referred to as gouge.

Table S1: Macroscopic rock parameters taken from literature and own measurements

Macroscopic rock parameter	Value	Reference
Porosity	9 - 11 %	Cheng et al. (2020); Hassanzadegan et al. (2012)
Density	2380 kg/m³	Hassanzadegan et al. (2012)
Matrix permeability	0.17 – 0.36 mD	Hassanzadegan et al. (2012)
Tensile strength	4.0 MPa	This study
Uniaxial compression strength	56.5 MPa	This study
Young’s modulus	18.1 GPa	This study
Poisson ratio	0.3	This study
Friction angle	28 °	This study

Table S2: Calibrated interparticle parameters in the YADE model

Calibrated interparticle parameter in YADE	Value
Density	2380 kg/m³
Tensile strength	4.5 MPa
Cohesion	34 MPa
Young’s modulus equivalent	16.6 GPa
Poisson’s ratio	0.41
Friction angle	30 °
Coordination number	10.1

Table S3: Permeability values of the exact single fracture derived from different methods in literature

Methodology	**Direction**	**Hydraulic aperture [µm]**	**Permeability [m²]**	**Reference**
Empirical equations (based on mechanical aperture)	x-direction	60 – 285	$3.0 \cdot 10^{-10}$ – $6.8 \cdot 10^{-9}$	Hale et al. (2020)
	y-direction	-	-	-
Air permeameter measurements	x-direction	81	$5.6 \cdot 10^{-10}$	Hale et al. (2020), Hale & Blum (2022)
	y-direction	57	$2.7 \cdot 10^{-10}$	Fuchs et al. (2024b)
Numerical hydraulic simulation	x-direction	85	$6.0 \cdot 10^{-10}$	Fuchs et al. (2024a)
	y-direction	73	$4.4 \cdot 10^{-10}$	Fuchs et al. (2024b)
Persistent Homology	x-direction	73 – 92	$4.4 \cdot 10^{-10}$ – $7.0 \cdot 10^{-10}$	Fuchs et al. (2024b)
	y-direction	62 – 86	$3.2 \cdot 10^{-10}$ – $6.2 \cdot 10^{-10}$	Fuchs et al. (2024b)

References

Alqahtani, N. J., Chung, T., Da Wang, Y., Armstrong, R. T., Swietojanski, P., & Mostaghimi, P. (2021). Flow-Based Characterization of Digital Rock Images Using Deep Learning. *SPE Journal*, *26*(04), 1800–1811. https://doi.org/10.2118/205376-PA

Amann, F., Gischig, V., Evans, K., Doetsch, J., Jalali, R., Valley, B., et al. (2018). The seismo-hydromechanical behavior during deep geothermal reservoir stimulations: open questions tackled in a decameter-scale in situ stimulation experiment. *Solid Earth*, *9*(1), 115–137. https://doi.org/10.5194/se-9-115-2018

Anderson, T. I., Guan, K. M., Vega, B., Aryana, S. A., & Kovscek, A. R. (2020). RockFlow: Fast Generation of Synthetic Source Rock Images Using Generative Flow Models. *Energies*, *13*(24), 6571. https://doi.org/10.3390/en13246571

Andrew, M., Bijeljic, B., & Blunt, M. J. (2014). Pore-scale imaging of trapped supercritical carbon dioxide in sandstones and carbonates. *International Journal of Greenhouse Gas Control*, *22*, 1–14. https://doi.org/10.1016/j.ijggc.2013.12.018

Araya-Polo, M., Alpak, F. O., Hunter, S., Hofmann, R., & Saxena, N. (2020). Deep learning–driven permeability estimation from 2D images. *Computational Geosciences*, *24*(2), 571–580. https://doi.org/10.1007/s10596-019-09886-9

Asadi, M. S., Rasouli, V., & Barla, G. (2012). A Bonded Particle Model Simulation of Shear Strength and Asperity Degradation for Rough Rock Fractures. *Rock Mechanics and Rock Engineering*. https://doi.org/10.1007/s00603-012-0231-4

Auradou, H. (2009). Influence of wall roughness on the geometrical, mechanical and transport properties of single fractures. *Journal of Physics D: Applied Physics*, *42*(21), 214015. https://doi.org/10.1088/0022-3727/42/21/214015

Auradou, H., Drazer, G., Hulin, J. P., & Koplik, J. (2005). Permeability anisotropy induced by the shear displacement of rough fracture walls. *Water Resources Research*, *41*(9), 2005WR003938. https://doi.org/10.1029/2005WR003938

Aydin, A. (2000). Fractures, faults, and hydrocarbon entrapment, migration and flow. *Marine and Petroleum Geology*, *17*(7), 797–814. https://doi.org/10.1016/S0264-8172(00)00020-9

Barton, N. (1982). *Modelling Rock Joint Behavior Form in Situ Block Tests: Implications for Nuclear Waste Repository Design : Technical Report* (Vol. 308). Columbus: Office of Nuclear Waste Isolation, Battelle Project Mangement Division.

Barton, N., & De Quadros, E. F. (1997). Joint aperture and roughness in the prediction of flow and groutability of rock masses. *International Journal of Rock Mechanics and Mining Sciences*, *34*(3–4), 252.e1-252.e14. https://doi.org/10.1016/S1365-1609(97)00081-6

Barton, N., Bandis, S., & Bakhtar, K. (1985). Strength, deformation and conductivity coupling of rock joints. *International Journal of Rock Mechanics and Mining Sciences & Geomechanics Abstracts*, *22*(3), 121–140. https://doi.org/10.1016/0148-9062(85)93227-9

Bear, J. (1972). *Dynamics of fluids in porous media*. New York: American Elsevier Pub. Co.

Berkowitz, B. (2002). Characterizing flow and transport in fractured geological media: A review. *Advances in Water Resources*, *25*(8–12), 861–884. https://doi.org/10.1016/S0309-1708(02)00042-8

Berre, I., Doster, F., & Keilegavlen, E. (2019). Flow in Fractured Porous Media: A Review of Conceptual Models and Discretization Approaches. *Transport in Porous Media*, *130*(1), 215–236. https://doi.org/10.1007/s11242-018-1171-6

Bertels, S. P., DiCarlo, D. A., & Blunt, M. J. (2001). Measurement of aperture distribution, capillary pressure, relative permeability, and in situ saturation in a rock fracture using computed tomography scanning. *Water Resources Research*, *37*(3), 649–662. https://doi.org/10.1029/2000WR900316

Bitenc, M., Kieffer, D. S., & Khoshelham, K. (2019). Range Versus Surface Denoising of Terrestrial Laser Scanning Data for Rock Discontinuity Roughness Estimation. *Rock Mechanics and Rock Engineering*, *52*(9), 3103–3117. https://doi.org/10.1007/s00603-019-01755-2

Bizhani, M., & Haeri Ardakani, O. (2021). Pore Characterization of Organic-Rich Shales through Application of Topological Data Analysis and Persistent Homology. *Energy & Fuels*, *35*(22), 18563–18573. https://doi.org/10.1021/acs.energyfuels.1c03255

Blöcher, G., Kluge, C., Milsch, H., Cacace, M., Jacquey, A. B., & Schmittbuhl, J. (2019). Permeability of matrix-fracture systems under mechanical loading – constraints from laboratory experiments and 3-D numerical modelling. *Advances in Geosciences*, *49*, 95–104. https://doi.org/10.5194/adgeo-49-95-2019

Blum, P., Mackay, R., & Riley, M. S. (2009). Stochastic simulations of regional scale advective transport in fractured rock masses using block upscaled hydro-mechanical rock property data. *Journal of Hydrology*, *369*(3–4), 318–325. https://doi.org/10.1016/j.jhydrol.2009.02.009

BMWK. (2023). 8. Energieforschungsprogramm zur angewandten Energieforschung - Forschungsmissionen für die Energiewende. Bundesministerium für Wirtschaft und Klimaschutz (BMWK).

Bobet, A., Fakhimi, A., Johnson, S., Morris, J., Tonon, F., & Yeung, M. R. (2009). Numerical Models in Discontinuous Media: Review of Advances for Rock Mechanics Applications. *Journal of Geotechnical and Geoenvironmental Engineering*, *135*(11), 1547–1561. https://doi.org/10.1061/(ASCE)GT.1943-5606.0000133

Bond, C. E., Kremer, Y., Johnson, G., Hicks, N., Lister, R., Jones, D. G., et al. (2017). The physical characteristics of a CO 2 seeping fault: The implications of fracture permeability for carbon capture and storage integrity. *International Journal of Greenhouse Gas Control*, *61*, 49–60. https://doi.org/10.1016/j.ijggc.2017.01.015

Bossart, P., Trick, T., Meier, P. M., & Mayor, J.-C. (2004). Structural and hydrogeological characterisation of the excavation-disturbed zone in the Opalinus Clay (Mont Terri Project, Switzerland). *Applied Clay Science*, *26*(1–4), 429–448. https://doi.org/10.1016/j.clay.2003.12.018

Bossart, P., Bernier, F., Birkholzer, J., Bruggeman, C., Connolly, P., Dewonck, S., et al. (2017). Mont Terri rock laboratory, 20 years of research: introduction, site characteristics and overview of experiments. *Swiss Journal of Geosciences*, *110*(1), 3–22. https://doi.org/10.1007/s00015-016-0236-1

Bröker, K., Ma, X., Gholizadeh Doonechaly, N., Rosskopf, M., Obermann, A., Rinaldi, A. P., et al. (2024). Hydromechanical characterization of a fractured crystalline rock volume during multi-stage hydraulic stimulations at the BedrettoLab. *Geothermics*, *124*, 103126. https://doi.org/10.1016/j.geothermics.2024.103126

Brown, S. (1987). Fluid flow through rock joints: The effect of surface roughness. *Journal of Geophysical Research: Solid Earth*, *92*(B2), 1337–1347. https://doi.org/10.1029/JB092iB02p01337

Brown, S. (1995). Simple mathematical model of a rough fracture. *Journal of Geophysical Research: Earth Surface*, *100*(B4), 5941–5952. https://doi.org/10.1029/94JB03262

Brown, S., & Smith, M. (2013). A transient-flow syringe air permeameter. *GEOPHYSICS*, *78*(5), 307–313. https://doi.org/10.1190/geo2012-0534.1

Brown, S., Caprihan, A., & Hardy, R. (1998). Experimental observation of fluid flow channels in a single fracture. *Journal of Geophysical Research*, *103*(B3), 5125–5132. https://doi.org/10.1029/97JB03542

Brush, D. J., & Thomson, N. R. (2003). Fluid flow in synthetic rough-walled fractures: Navier-Stokes, Stokes, and local cubic law simulations. *Water Resources Research*, *39*(4). https://doi.org/10.1029/2002WR001346

Candela, T., Renard, F., Klinger, Y., Mair, K., Schmittbuhl, J., & Brodsky, E. E. (2012). Roughness of fault surfaces over nine decades of length scales. *Journal of Geophysical Research: Earth Surface*, *117*(B8). https://doi.org/10.1029/2011JB009041

Cardenas, M. B., Slottke, D. T., Ketcham, R. A., & Sharp, J. M. (2007). Navier-Stokes flow and transport simulations using real fractures shows heavy tailing due to eddies. *Geophysical Research Letters*, *34*(14), 2007GL030545. https://doi.org/10.1029/2007GL030545

Cardona, A., Finkbeiner, T., & Santamarina, J. C. (2021). Natural Rock Fractures: From Aperture to Fluid Flow. *Rock Mechanics and Rock Engineering*, *54*(11), 5827–5844. https://doi.org/10.1007/s00603-021-02565-1

Carey, J. W., Lei, Z., Rougier, E., Mori, H., & Viswanathan, H. (2015). Fracture-permeability behavior of shale. *Journal of Unconventional Oil and Gas Resources*, *11*, 27–43. https://doi.org/10.1016/j.juogr.2015.04.003

Carlsson, G. (2009). Topology and data. *Bulletin of the Americal Mathmatical Society*, (46), 255–308. https://doi.org/10.1090/S0273-0979-09-01249-X

Carman, P. C. (1937). Fluid flow through a granular bed. *Trans. Inst. Chem. Eng.*, (15), 150–167.

Chae, B. G., Ichikawa, Y., Jeong, G. C., Seo, Y. S., & Kim, B. C. (2004). Roughness measurement of rock discontinuities using a confocal laser scanning microscope and the Fourier spectral analysis. *Engineering Geology*, *72*(3–4), 181–199. https://doi.org/10.1016/j.enggeo.2003.08.002

Chan, J. M., Carlsson, G., & Rabadan, R. (2013). Topology of viral evolution. *Proceedings of the National Academy of Sciences of the United States of America*, *110*(46), 18566–71. https://doi.org/10.1073/pnas.1313480110

Chandler, M. A., Goggin, D., & Lake, L. W. (1989). A Mechanical Field Permeameter for Making Rapid, Non-Destructive, Permeability Measurements. *Journal of Sedimentary Research*, *59*(4), 613–615.

Chen, Y., Selvadurai, A. P. S., & Zhao, Z. (2021). Modeling of flow characteristics in 3D rough rock fracture with geometry changes under confining stresses. *Computers and Geotechnics*, *130*, 103910. https://doi.org/10.1016/j.compgeo.2020.103910

Chen, Z., Narayan, S. P., Yang, Z., & Rahman, S. S. (2000). An experimental investigation of hydraulic behaviour of fractures and joints in granitic rock. *International Journal of Rock Mechanics and Mining Sciences*, *37*(7), 1061–1071. https://doi.org/10.1016/S1365-1609(00)00039-3

Cheng, C., Hale, S., Milsch, H., & Blum, P. (2020). Measuring hydraulic fracture apertures: a comparison of methods. *Solid Earth*, *11*(6), 2411–2423. https://doi.org/10.5194/se-11-2411-2020

Choudhury, A. N. M. I., Wang, B., Rosen, P., & Pascucci, V. (2012). Topological analysis and visualization of cyclical behavior in memory reference traces. In *2012 IEEE Pacific Visualization Symposium* (pp. 9–16). IEEE. https://doi.org/10.1109/PacificVis.2012.6183557

Cignoni, P., Corsini, M., & Ranzuglia, G. (2008, January 1). MeshLab: an Open-Source 3D Mesh Processing System. ERCIM News.

Costa, A. (2006). Permeability-porosity relationship: A reexamination of the Kozeny-Carman equation based on a fractal pore-space geometry assumption. *Geophysical Research Letters*, *33*(2). https://doi.org/10.1029/2005GL025134

Crandall, D., Bromhal, G., & Karpyn, Z. T. (2010). Numerical simulations examining the relationship between wall-roughness and fluid flow in rock fractures. *International Journal of Rock Mechanics and Mining Sciences*, *47*(5), 784–796. https://doi.org/10.1016/j.ijrmms.2010.03.015

Da Wang, Y., Blunt, M. J., Armstrong, R. T., & Mostaghimi, P. (2021). Deep learning in pore scale imaging and modeling. *Earth-Science Reviews, 215*, 103555. https://doi.org/10.1016/j.earscirev.2021.103555

Davis, J. M., Wilson, J. L., & Phillips, F. M. (1994). A Portable Air-Minipermeameter for Rapid In Situ Field Measurements. *Groundwater*, *32*(2), 258–266. https://doi.org/10.1111/j.1745-6584.1994.tb00640.x

Deichmann, N., & Giardini, D. (2009). Earthquakes Induced by the Stimulation of an Enhanced Geothermal System below Basel (Switzerland). *Seismological Research Letters*, *80*(5), 784–798. https://doi.org/10.1785/gssrl.80.5.784

Delgado-Friedrichs, O., Robins, V., & Sheppard, A. (2014). Morse theory and persistent homology for topological analysis of 3D images of complex materials. In *2014 IEEE International Conference on Image Processing (ICIP)* (pp. 4872–4876). IEEE. https://doi.org/10.1109/ICIP.2014.7025987

Deng, Q., Blöcher, G., Cacace, M., & Schmittbuhl, J. (2021). Hydraulic Diffusivity of a Partially Open Rough Fracture. *Rock Mechanics and Rock Engineering*. https://doi.org/10.1007/s00603-021-02629-2

Deng, Q., Schmittbuhl, J., Cacace, M., & Blöcher, G. (2024). Mechanical Stiffness and Permeability of a Reservoir-Scale Rough Fracture During Closure. *Journal of Geophysical Research: Solid Earth*, *129*(9), e2024JB029001. https://doi.org/10.1029/2024JB029001

Durham, W. B., Bourcier, W. L., & Burton, E. A. (2001). Direct observation of reactive flow in a single fracture. *Water Resources Research*, *37*(1), 1–12. https://doi.org/10.1029/2000WR900228

Duriez, J., Scholtès, L., & Donzé, F.-V. (2016). Micromechanics of wing crack propagation for different flaw properties. *Engineering Fracture Mechanics*, *153*, 378–398. https://doi.org/10.1016/j.engfracmech.2015.12.034

Edelsbrunner, H., Letscher, D., & Zomorodian, A. (2000). Topological persistence and simplification. In *Proceedings 41st Annual Symposium on Foundations of Computer Science* (pp. 454–463). IEEE Comput. Soc. https://doi.org/10.1109/SFCS.2000.892133

Egert, R., Nitschke, F., Gholami Korzani, M., & Kohl, T. (2021). Stochastic 3D Navier-Stokes Flow in Self-Affine Fracture Geometries Controlled by Anisotropy and Channeling. *Geophysical Research Letters*, *48*(9). https://doi.org/10.1029/2020GL092138

Egert, R., Nitschke, F., Gholami Korzani, M., & Kohl, T. (2023). Spatial Characterization of Channeling in Sheared Rough-Walled Fractures in the Transition to Nonlinear Fluid Flow. *Water Resources Research*, *59*(10), e2022WR034362. https://doi.org/10.1029/2022WR034362

Eijpe, R., & Weber, K. J. (1971). Mini-Permeameters for Consolidated Rock and Unconsolidated Sand: GEOLOGICAL NOTE. *AAPG Bulletin*, *55*. https://doi.org/10.1306/5d25ce25-16c1-11d7-8645000102c1865d

Ellsworth, W. L. (2013). Injection-Induced Earthquakes. *Science*, *341*(6142), 1225942. https://doi.org/10.1126/science.1225942

Esaki, T., Du, S., Mitani, Y., Ikusada, K., & Jing, L. (1999). Development of a shear-flow test apparatus and determination of coupled properties for a single rock joint. *International Journal of Rock Mechanics and Mining Sciences*, *36*(5), 641–650. https://doi.org/10.1016/S0148-9062(99)00044-3

Fang, Y., Elsworth, D., Wang, C., Ishibashi, T., & Fitts, J. P. (2017). Frictional stability-permeability relationships for fractures in shales. *Journal of Geophysical Research: Solid Earth*, *122*(3), 1760–1776. https://doi.org/10.1002/2016JB013435

Fang, Z., & Wu, W. (2022). Laboratory friction-permeability response of rock fractures: a review and new insights. *Geomechanics and Geophysics for Geo-Energy and Geo-Resources*, *8*(1), 15. https://doi.org/10.1007/s40948-021-00316-8

Fardin, N. (2008). Influence of Structural Non-Stationarity of Surface Roughness on Morphological Characterization and Mechanical Deformation of Rock Joints. *Rock Mechanics and Rock Engineering*, *41*(2), 267–297. https://doi.org/10.1007/s00603-007-0144-9

Faro Technologies Inc. (2016). Faro Scanner Freestyle3D Objects: Medium volume high accuracy color handheld laserscanner for reality capture, reverse engineering and crime scene documentation.

Ferer, M., Crandall, D., Ahmadi, G., & Smith, D. H. (2011). Two-phase flow in a rough fracture: experiment and modeling. *Physical Review. E, Statistical, Nonlinear, and Soft Matter Physics*, *84*(1 Pt 2), 016316. https://doi.org/10.1103/PhysRevE.84.016316

Filomena, C. M., Hornung, J., & Stollhofen, H. (2014). Assessing accuracy of gas-driven permeability measurements: a comparative study of diverse Hassler-cell and probe permeameter devices. *Solid Earth*, *5*(1), 1–11. https://doi.org/10.5194/se-5-1-2014

Fischer, C., Dunkl, I., Von Eynatten, H., Wijbrans, J. R., & Gaupp, R. (2012). Products and timing of diagenetic processes in Upper Rotliegend sandstones from Bebertal (North German Basin, Parchim Formation, Flechtingen High, Germany). *Geological Magazine*, *149*(5), 827–840. https://doi.org/10.1017/S0016756811001087

Frank, S., Heinze, T., Ribbers, M., & Wohnlich, S. (2020). Experimental Reproducibility and Natural Variability of Hydraulic Transport Properties of Fractured Sandstone Samples. *Geosciences*, *10*(11), 458. https://doi.org/10.3390/geosciences10110458

Frash, L. P., Carey, J. W., Lei, Z., Rougier, E., Ickes, T., & Viswanathan, H. S. (2016). High-stress triaxial direct-shear fracturing of Utica shale and in situ X-ray microtomography with permeability measurement. *Journal of Geophysical Research: Solid Earth*, *121*(7), 5493–5508. https://doi.org/10.1002/2016JB012850

Freeze, R. A., & Cherry, J. A. (1979). *Groundwater*. Englewood Cliffs, N.J: Prentice-Hall.

Fuchs, M., Hale, S., Blesch, L., Rau, G. C., Menberg, K., & Blum, P. (2024). Evaluating Fracture Surface Imaging Methods Using Flow Simulations and Air Permeameter Measurements. *Rock Mechanics and Rock Engineering*, *57*(3), 1849–1860. https://doi.org/10.1007/s00603-023-03615-6

Fuchs, M., Suzuki, A., Hasumi, T., & Blum, P. (2024). Investigating rough single-fracture permeabilities with persistent homology. *Solid Earth*, *15*(3), 353–365. https://doi.org/10.5194/se-15-353-2024

Furukawa, Y., Curless, B., Seitz, S. M., & Szeliski, R. (2010). Towards Internet-scale multi-view stereo. *2010 IEEE Computer Society Conference*, 1434–1441. https://doi.org/10.1109/CVPR.2010.5539802

Gaucher, E., Schoenball, M., Heidbach, O., Zang, A., Fokker, P., van Wees, J.-D., & Kohl, T. (2015). Induced seismicity in geothermal reservoirs: Physical processes and key parameters. *World Geothermal Congress*, 1–13.

Gerhart, J. M. (1984). A Model of Regional Ground-Water Flow in Secondary-Permeability Terrane. *Groundwater*, *22*(2), 168–175. https://doi.org/10.1111/j.1745-6584.1984.tb01486.x

Gill, M., Crandall, D., Moore, J., Mackey, P., & Brown, S. (2021). Gouge formation and dilation impacts to flow during fracture shearing. *International Journal of Rock Mechanics and Mining Sciences*, *147*, 104920. https://doi.org/10.1016/j.ijrmms.2021.104920

Giudicelli, G., Lindsay, A., Harbour, L., Icenhour, C., Li, M., Hansel, J. E., et al. (2024). 3.0 - MOOSE: Enabling massively parallel multiphysics simulations. *SoftwareX*, *26*, 101690. https://doi.org/10.1016/j.softx.2024.101690

Giwelli, A. A., Sakaguchi, K., Gumati, A., & Matsuki, K. (2014). Shear behaviour of fractured rock as a function of size and shear displacement. *Geomechanics and Geoengineering*, *9*(4), 253–264. https://doi.org/10.1080/17486025.2014.884728

Grasselli, G., Wirth, J., & Egger, P. (2002). Quantitative three-dimensional description of a rough surface and parameter evolution with shearing. *International Journal of Rock Mechanics and Mining Sciences*, *39*(6), 789–800. https://doi.org/10.1016/S1365-1609(02)00070-9

Greenwood, J. A., & Williamson, J. B. P. (1966). Contact of nominally flat surfaces. *Proceedings of the Royal Society of London. Series A. Mathematical and Physical Sciences*, *295*(1442), 300–319. https://doi.org/10.1098/rspa.1966.0242

Grünthal, G. (2014). Induced seismicity related to geothermal projects versus natural tectonic earthquakes and other types of induced seismic events in Central Europe. *Geothermics*, *52*, 22–35. https://doi.org/10.1016/j.geothermics.2013.09.009

Gutierrez, M., Øino, L. E., & Nygård, R. (2000). Stress-dependent permeability of a de-mineralised fracture in shale. *Marine and Petroleum Geology*, *17*(8), 895–907. https://doi.org/10.1016/S0264-8172(00)00027-1

Gutjahr, T., Hale, S., Keller, K., Blum, P., & Winter, S. (2022). Quantification of Fracture Roughness by Change Probabilities and Hurst Exponents. *Mathematical Geosciences*, *54*(4), 679–710. https://doi.org/10.1007/s11004-021-09985-3

Hakami, E. (1995). *Aperture Distribution of Rock Fractures*. Stockholm.

Hakami, E., & Larsson, E. (1996). Aperture measurements and flow experiments on a single natural fracture. *International Journal of Rock Mechanics and Mining Sciences &*

Geomechanics Abstracts, *33*(4), 395–404. https://doi.org/10.1016/0148-9062(95)00070-4

Hale, S. (2022). *Coupled hydro-mechanical-chemical processes in porous and fractured media*. Karlsruhe Institute of Technology (KIT), Karlsruhe.

Hale, S., & Blum, P. (2022). Bestimmung der hydraulischen Durchlässigkeiten eines Sandsteins mithilfe eines Luftpermeameters. *Grundwasser*. https://doi.org/10.1007/s00767-021-00504-z

Hale, S., Naab, C., Butscher, C., & Blum, P. (2020). Method Comparison to Determine Hydraulic Apertures of Natural Fractures. *Rock Mechanics and Rock Engineering*, *53*(3), 1467–1476. https://doi.org/10.1007/s00603-019-01966-7

Hale, S., Ries, X., Jaeggi, D., & Blum, P. (2021). Mechanical and hydraulic properties of the excavation damaged zone (EDZ) in the Opalinus Clay of the Mont Terri rock laboratory, Switzerland. *Solid Earth*, *12*(7), 1581–1600. https://doi.org/10.5194/se-12-1581-2021

Hale, S., Trindade Pedrosa, E., Jacob, A., Reinhardt, M., Enzmann, F., Kersten, M., et al. (2022). Upscaling calcite dissolution rates in a tight reservoir sandstone. *Environmental Earth Sciences*, *81*(11), 303. https://doi.org/10.1007/s12665-022-10399-5

Hart, R., Cundall, P. A., & Lemos, J. (1988). Formulation of a three-dimensional distinct element model—Part II. Mechanical calculations for motion and interaction of a system composed of many polyhedral blocks. *International Journal of Rock Mechanics and Mining Sciences & Geomechanics Abstracts*, *25*(3), 117–125. https://doi.org/10.1016/0148-9062(88)92294-2

Hassanzadegan, A., Blöcher, G., Zimmermann, G., & Milsch, H. (2012). Thermoporoelastic properties of Flechtinger sandstone. *International Journal of Rock Mechanics and Mining Sciences*, *49*, 94–104. https://doi.org/10.1016/j.ijrmms.2011.11.002

Hassanzadegan, A., Blöcher, G., Milsch, H., Urpi, L., & Zimmermann, G. (2014). The Effects of Temperature and Pressure on the Porosity Evolution of Flechtinger Sandstone. *Rock Mechanics and Rock Engineering*, *47*(2), 421–434. https://doi.org/10.1007/s00603-013-0401-z

Heidsiek, M., Butscher, C., Blum, P., & Fischer, C. (2020). Small-scale diagenetic facies heterogeneity controls porosity and permeability pattern in reservoir sandstones. *Environmental Earth Sciences*, *79*(18), 425. https://doi.org/10.1007/s12665-020-09168-z

Heiland, J. (2003). Permeability of Triaxially Compressed Sandstone: Influence of Deformation and Strain-rate on Permeability. In H.-J. Kümpel (Ed.), *Thermo-Hydro-Mechanical Coupling in Fractured Rock* (pp. 889–908). Basel: Birkhäuser Basel. https://doi.org/10.1007/978-3-0348-8083-1_6

Hiraoka, Y., Nakamura, T., Hirata, A., Escolar, E. G., Matsue, K., & Nishiura, Y. (2016). Hierarchical structures of amorphous solids characterized by persistent homology. *Proceedings of the National Academy of Sciences of the United States of America*, *113*(26), 7035–40. https://doi.org/10.1073/pnas.1520877113

Hong, J., & Liu, J. (2020). Rapid estimation of permeability from digital rock using 3D convolutional neural network. *Computational Geosciences*, *24*(4), 1523–1539. https://doi.org/10.1007/s10596-020-09941-w

Hopkins, D. L., Cook, N. G. W., & Myer, L. R. (1987). Fracture Stiffness And Aperture As A Function Of Applied Stress And Contact Geometry (p. ARMA-87-0673). Presented at the The 28th U.S. Symposium on Rock Mechanics (USRMS).

Huang, S. L., Oelfke, S. M., & Speck, R. C. (1992). Applicability of fractal characterization and modelling to rock joint profiles. *International Journal of Rock Mechanics and Mining Sciences & Geomechanics Abstracts*, *29*(2), 89–98. https://doi.org/10.1016/0148-9062(92)92120-2

Huerta, N. J., Hesse, M. A., Bryant, S. L., Strazisar, B. R., & Lopano, C. L. (2013). Experimental evidence for self-limiting reactive flow through a fractured cement core: implications for time-dependent wellbore leakage. *Environmental Science & Technology*, *47*(1), 269–75. https://doi.org/10.1021/es3013003

Hurst, A., & Goggin, D. (1995). Probe Permeametry: An Overview and Bibliography. *AAPG Bulletin*, *79*. https://doi.org/10.1306/8d2b1566-171e-11d7-8645000102c1865d

Ingebritsen, S. E., & Manning, C. E. (2011). Permeability of the continental crust: dynamic variations inferred from seismicity and metamorphism. In *Frontiers in Geofluids*. Chichester: John Wiley & Sons.

Ishibashi, T., Elsworth, D., Fang, Y., Riviere, J., Madara, B., Asanuma, H., et al. (2018). Friction-Stability-Permeability Evolution of a Fracture in Granite. *Water Resources Research*, *54*(12), 9901–9918. https://doi.org/10.1029/2018WR022598

Iwai, K. (1976). *Fundamental studies of fluid flow through a single fracture*. University of California, Berkeley.

James, M. R., & Robson, S. (2012). Straightforward reconstruction of 3D surfaces and topography with a camera: Accuracy and geoscience application. *Journal of Geophysical Research: Earth Surface*, *117*(F3). https://doi.org/10.1029/2011JF002289

Javadi, M., Sharifzadeh, M., & Shahriar, K. (2010). A new geometrical model for non-linear fluid flow through rough fractures. *Journal of Hydrology*, *389*(1–2), 18–30. https://doi.org/10.1016/j.jhydrol.2010.05.010

Javanmard, H., Ebigbo, A., Walsh, S. D. C., Saar, M. O., & Vogler, D. (2021). No-Flow Fraction (NFF) Permeability Model for Rough Fractures Under Normal Stress. *Water Resources Research*, *57*(3), e2020WR029080. https://doi.org/10.1029/2020WR029080

Jiang, F., Tsuji, T., & Shirai, T. (2018). Pore Geometry Characterization by Persistent Homology Theory. *Water Resources Research*, *54*(6), 4150–4163. https://doi.org/10.1029/2017WR021864

Johns, R. A., Steude, J. S., Castanier, L. M., & Roberts, P. V. (1993). Nondestructive measurements of fracture aperture in crystalline rock cores using X ray computed tomography. *Journal of Geophysical Research: Solid Earth*, *98*(B2), 1889–1900. https://doi.org/10.1029/92JB02298

Karpyn, Z. T., Grader, A. S., & Halleck, P. M. (2007). Visualization of fluid occupancy in a rough fracture using micro-tomography. *Journal of Colloid and Interface Science*, *307*(1), 181–7. https://doi.org/10.1016/j.jcis.2006.10.082

Kling, T., Da Huo, Schwarz, J.-O., Enzmann, F., Benson, S., & Blum, P. (2016). Simulating stress-dependent fluid flow in a fractured core sample using real-time X-ray CT data. *Solid Earth*, *7*(4), 1109–1124. https://doi.org/10.5194/se-7-1109-2016

Kling, T., Schwarz, J.-O., Wendler, F., Enzmann, F., & Blum, P. (2017). Fracture flow due to hydrothermally induced quartz growth. *Advances in Water Resources*, *107*, 93–107. https://doi.org/10.1016/j.advwatres.2017.06.011

Kling, T., Vogler, D., Pastewka, L., Amann, F., & Blum, P. (2018). Numerical Simulations and Validation of Contact Mechanics in a Granodiorite Fracture. *Rock Mechanics and Rock Engineering*, *51*(9), 2805–2824. https://doi.org/10.1007/s00603-018-1498-x

Kluge, C., Blöcher, G., Barnhoorn, A., Schmittbuhl, J., & Bruhn, D. (2021). Permeability Evolution During Shear Zone Initiation in Low-Porosity Rocks. *Rock Mechanics and Rock Engineering*, *54*(10), 5221–5244. https://doi.org/10.1007/s00603-020-02356-0

Kozeny, J. (1927). Ueber kapillare Leitung des Wassers im Boden. *Sitzungsber. Akad. Wiss.*, (136), 271–306.

Kulatilake, P. H. S. W., Shou, G., Huang, T. H., & Morgan, R. M. (1995). New peak shear strength criteria for anisotropic rock joints. *International Journal of Rock Mechanics and Mining Sciences & Geomechanics Abstracts*, *32*(7), 673–697. https://doi.org/10.1016/0148-9062(95)00022-9

Lambert, C., & Coll, C. (2014). Discrete modeling of rock joints with a smooth-joint contact model. *Journal of Rock Mechanics and Geotechnical Engineering*, *6*(1), 1–12. https://doi.org/10.1016/j.jrmge.2013.12.003

Lanaro, F. (2000). A random field model for surface roughness and aperture of rock fractures. *International Journal of Rock Mechanics and Mining Sciences*, *37*(8), 1195–1210. https://doi.org/10.1016/S1365-1609(00)00052-6

Lee, D., Karadimitriou, N., Ruf, M., & Steeb, H. (2022). Detecting micro fractures: a comprehensive comparison of conventional and machine-learning-based segmentation methods. *Solid Earth*, *13*(9), 1475–1494. https://doi.org/10.5194/se-13-1475-2022

Li, X., Zhang, F., Xiu, N., Weng, D., Cai, B., & Fu, H. (2024). Shear-induced permeability evolution of natural fractures in granite: Implications for stimulation of EGS reservoirs. *Engineering Geology*, *338*, 107629. https://doi.org/10.1016/j.enggeo.2024.107629

Li, Y., Chen, Y.-F., & Zhou, C.-B. (2014). Hydraulic properties of partially saturated rock fractures subjected to mechanical loading. *Engineering Geology*, *179*, 24–31. https://doi.org/10.1016/j.enggeo.2014.06.019

Li, Z., Ma, X., Kong, X.-Z., Saar, M. O., & Vogler, D. (2023). Permeability evolution during pressure-controlled shear slip in saw-cut and natural granite fractures. *Rock Mechanics Bulletin*, *2*(2), 100027. https://doi.org/10.1016/j.rockmb.2022.100027

Lianheng, Z., Dongliang, H., Jingyu, C., Xiang, W., Wei, L., Zhiheng, Z., et al. (2020). A practical photogrammetric workflow in the field for the construction of a 3D rock joint surface database. *Engineering Geology*, *279*, 105878. https://doi.org/10.1016/j.enggeo.2020.105878

Liu, H. Y., Han, H., An, H. M., & Shi, J. J. (2016). Hybrid finite-discrete element modelling of asperity degradation and gouge grinding during direct shearing of rough rock joints. *International Journal of Coal Science & Technology*, *3*(3), 295–310. https://doi.org/10.1007/s40789-016-0142-1

Lomize, G. (1951). Flow in fractured rocks. Gosenergoizdat, Moscow.

Louis, C. (1967). *Strömungswirkung in klüftigen Medien und ihre Wirkung auf die Standsicherheit von Bauwerken und Böschungen im Fels*. Karlsruhe.

Louis, C. (1969). *A study of groundwater flow in jointed rock and its influence on the stability of rock masses* (Vol. 10). Imperial College of Science and Technology.

Louis, C. (1972). Rock Hydraulics. In L. Müller (Ed.), *Rock Mechanics* (pp. 299–387). Vienna: Springer Vienna. https://doi.org/10.1007/978-3-7091-4109-0_16

Makurat, A., Gutierrez, M., & Backer, L. (1997). Fracture flow and fracture cross flow experiments. In *Norwegian Petroleum Society Special Publications* (Vol. 7, pp. 139–148). Elsevier. https://doi.org/10.1016/S0928-8937(97)80012-4

Marchand, S., Mersch, O., Selzer, M., Nitschke, F., Schoenball, M., Schmittbuhl, J., et al. (2020). A Stochastic Study of Flow Anisotropy and Channelling in Open Rough Fractures. *Rock Mechanics and Rock Engineering*, *53*(1), 233–249. https://doi.org/10.1007/s00603-019-01907-4

Marsch, K., Wujanz, D., & Fernandez-Steeger, T. M. (2020). On the usability of different optical measuring techniques for joint roughness evaluation. *Bulletin of Engineering Geology and the Environment*, *79*(2), 811–830. https://doi.org/10.1007/s10064-019-01606-y

Matsuki, K., Lee, J.-J., Sakaguchi, K., & Hayashi, K. (1999). Size effect in flow conductance of a closed small-scale hydraulic fracture in granite. *Geothermal Science and Technology*, *1–4*(6), 113–138.

Méheust, Y., & Schmittbuhl, J. (2003). Scale Effects Related to Flow in Rough Fractures. *Pure and Applied Geophysics PAGEOPH*, *160*(5–6), 1023–1050. https://doi.org/10.1007/PL00012559

Mehmani, Y., & Tchelepi, H. A. (2017). Minimum requirements for predictive pore-network modeling of solute transport in micromodels. *Advances in Water Resources*, *108*, 83–98. https://doi.org/10.1016/j.advwatres.2017.07.014

Milsch, H., Hofmann, H., & Blöcher, G. (2016). An experimental and numerical evaluation of continuous fracture permeability measurements during effective pressure cycles. *International Journal of Rock Mechanics and Mining Sciences*, *89*, 109–115. https://doi.org/10.1016/j.ijrmms.2016.09.002

Min, K.-B., Jing, L., & Stephansson, O. (2004). Determining the equivalent permeability tensor for fractured rock masses using a stochastic REV approach: Method and application to the field data from Sellafield, UK. *Hydrogeology Journal*, *12*(5), 497–510. https://doi.org/10.1007/s10040-004-0331-7

Moon, C., Mitchell, S. A., Heath, J. E., & Andrew, M. (2019). Statistical Inference Over Persistent Homology Predicts Fluid Flow in Porous Media. *Water Resources Research*, *55*(11), 9592–9603. https://doi.org/10.1029/2019WR025171

Moreno, L., Tsang, Y. W., Tsang, C. F., Hale, F. V., & Neretnieks, I. (1988). Flow and tracer transport in a single fracture: A stochastic model and its relation to some field observations. *Water Resources Research*, *24*(12), 2033–2048. https://doi.org/10.1029/WR024i012p02033

Muljadi, B. P., Blunt, M. J., Raeini, A. Q., & Bijeljic, B. (2016). The impact of porous media heterogeneity on non-Darcy flow behaviour from pore-scale simulation. *Advances in Water Resources*, *95*, 329–340. https://doi.org/10.1016/j.advwatres.2015.05.019

Müller, C., Siegesmund, S., & Blum, P. (2010). Evaluation of the representative elementary volume (REV) of a fractured geothermal sandstone reservoir. *Environmental Earth Sciences*, *61*(8), 1713–1724. https://doi.org/10.1007/s12665-010-0485-7

Nelson, R. A., & Handin, J. (1977). Experimental Study of Fracture Permeability in Porous Rock. *The American Association of Petroleum Geologists Bulletin*, *61*(2), 227–236.

Nemoto, K., Watanabe, N., Hirano, N., & Tsuchiya, N. (2009). Direct measurement of contact area and stress dependence of anisotropic flow through rock fracture with heterogeneous aperture distribution. *Earth and Planetary Science Letters*, *281*(1–2), 81–87. https://doi.org/10.1016/j.epsl.2009.02.005

Neuville, A., Toussaint, R., & Schmittbuhl, J. (2010). Hydrothermal coupling in a self-affine rough fracture. *Physical Review. E, Statistical, Nonlinear, and Soft Matter Physics*, *82*(3 Pt 2), 036317. https://doi.org/10.1103/PhysRevE.82.036317

New England Research Inc. (2016). *TinyPerm 3*. White River Junction, VT.

Nguyen, H. N. G., Scholtès, L., Guglielmi, Y., Donzé, F. V., Ouraga, Z., & Souley, M. (2021). Micromechanics of Sheared Granular Layers Activated by Fluid Pressurization. *Geophysical Research Letters*, *48*(14), e2021GL093222. https://doi.org/10.1029/2021GL093222

Nikon Metrology NV. (2010). *MCA II Articulated arms: Portable productivity*.

Nikon Metrology NV. (2018). ModelMaker Handheld scanners, MCAx Articulated arms.

Nolte, D. D., Pyrak-Nolte, L. J., & Cook, N. G. W. (1989). The fractal geometry of flow paths in natural fractures in rock and the approach to percolation. *Pure and Applied Geophysics PAGEOPH*, *131*(1–2), 111–138. https://doi.org/10.1007/BF00874483

Novakowski, K. S., & Lapcevic, P. A. (1994). Field measurement of radial solute transport in fractured rock. *Water Resources Research*, *30*(1), 37–44. https://doi.org/10.1029/93WR02401

Obayashi, I., Nakamura, T., & Hiraoka, Y. (2022). Persistent Homology Analysis for Materials Research and Persistent Homology Software: HomCloud. *Journal of the Physical Society of Japan*, *91*(9), 091013. https://doi.org/10.7566/JPSJ.91.091013

Oliveira, G. L. P., Ceia, M. A. R., Missagia, R. M., Lima Neto, I., Santos, V. H., & Paranhos, R. (2020). Core plug and 2D/3D-image integrated analysis for improving permeability estimation based on the differences between micro- and macroporosity in Middle East carbonate rocks. *Journal of Petroleum Science and Engineering*, *193*, 107335. https://doi.org/10.1016/j.petrol.2020.107335

Olsson, R., & Barton, N. (2001). An improved model for hydromechanical coupling during shearing of rock joints. *International Journal of Rock Mechanics and Mining Sciences*, *38*(3), 317–329. https://doi.org/10.1016/S1365-1609(00)00079-4

Oron, A. P., & Berkowitz, B. (1998). Flow in rock fractures: The local cubic law assumption reexamined. *Water Resources Research*, *34*(11), 2811–2825. https://doi.org/10.1029/98WR02285

Patir, N., & Cheng, H. S. (1978). An Average Flow Model for Determining Effects of Three-Dimensional Roughness on Partial Hydrodynamic Lubrication. *Journal of Lubrication Technology*, *100*(1), 12–17. https://doi.org/10.1115/1.3453103

Permann, C. J., Gaston, D. R., Andrš, D., Carlsen, R. W., Kong, F., Lindsay, A. D., et al. (2020). MOOSE: Enabling massively parallel multiphysics simulation. *SoftwareX*, *11*, 100430. https://doi.org/10.1016/j.softx.2020.100430

Pyrak-Nolte, L. J., & Morris, J. P. (2000). Single fractures under normal stress: The relation between fracture specific stiffness and fluid flow. *International Journal of Rock Mechanics and Mining Sciences*, *37*(1–2), 245–262. https://doi.org/10.1016/S1365-1609(99)00104-5

Pyrak-Nolte, L. J., Sumner, M. E., Deng, J., & Kang, P. K. (2023). Geometry of Fracture Intersections: The Impact on Flow and Mixing (Vol. 2023, pp. H11C-06). Presented at the AGU Fall Meeting Abstracts. Retrieved from https://ui.adsabs.harvard.edu/abs/2023AGUFM.H11C..06P

Renard, F., Voisin, C., Marsan, D., & Schmittbuhl, J. (2006). High resolution 3D laser scanner measurements of a strike-slip fault quantify its morphological anisotropy at all scales. *Geophysical Research Letters*, *33*(4). https://doi.org/10.1029/2005GL025038

Renard, F., Bernard, D., Desrues, J., & Ougier-Simonin, A. (2009). 3D imaging of fracture propagation using synchrotron X-ray microtomography. *Earth and Planetary Science Letters*, *286*(1–2), 285–291. https://doi.org/10.1016/j.epsl.2009.06.040

Renard, F., McBeck, J., & Cordonnier, B. (2020). Competition between slow slip and damage on and off faults revealed in 4D synchrotron imaging experiments. *Tectonophysics*, *782–783*, 228437. https://doi.org/10.1016/j.tecto.2020.228437

Renshaw, C. E. (1995). On the relationship between mechanical and hydraulic apertures in rough-walled fractures. *Journal of Geophysical Research: Solid Earth*, *100*(B12), 24629–24636. https://doi.org/10.1029/95JB02159

Riegel, H., Zambrano, M., Balsamo, F., Mattioni, L., & Tondi, E. (2019). Petrophysical Properties and Microstructural Analysis of Faulted Heterolithic Packages: A Case Study from Miocene Turbidite Successions, Italy. *Geofluids*, *2019*, 1–23. https://doi.org/10.1155/2019/9582359

Robins, V., Saadatfar, M., Delgado-Friedrichs, O., & Sheppard, A. P. (2016). Percolating length scales from topological persistence analysis of micro- CT images of porous materials. *Water Resources Research*, *52*(1), 315–329. https://doi.org/10.1002/2015WR017937

Ruf, M., & Steeb, H. (2020). An open, modular, and flexible micro X-ray computed tomography system for research. *The Review of Scientific Instruments*, *91*(11), 113102. https://doi.org/10.1063/5.0019541

Rutqvist, J. (2015). Fractured rock stress-permeability relationships from in situ data and effects of temperature and chemical-mechanical couplings. *Geofluids*, *15*(1–2), 48–66. https://doi.org/10.1111/gfl.12089

Schädle, P. (2020). SaintBernard: A MOOSE Application to model flow and transport through lower dimensional rough fractures.

Schmittbuhl, J., Lambotte, S., Lengliné, O., Grunberg, M., Jund, H., Vergne, J., et al. (2022). Induced and triggered seismicity below the city of Strasbourg, France from November

2019 to January 2021. *Comptes Rendus. Géoscience*, *353*(S1), 561–584. https://doi.org/10.5802/crgeos.71

Scholtès, L., & Donzé, F.-V. (2013). A DEM model for soft and hard rocks: Role of grain interlocking on strength. *Journal of the Mechanics and Physics of Solids*, *61*(2), 352–369. https://doi.org/10.1016/j.jmps.2012.10.005

Sidle, R. C., Nilsson, B., Hansen, M., & Fredericia, J. (1998). Spatially varying hydraulic and solute transport characteristics of a fractured till determined by field tracer tests, Funen, Denmark. *Water Resources Research*, *34*(10), 2515–2527. https://doi.org/10.1029/98wr01735

Smilauer, V., Angelidakis, V., Catalano, E., Caulk, R., Chareyre, B., Chèvremont, W., et al. (2021, November 15). Yade documentation (Version 3rd). Zenodo. https://doi.org/10.5281/ZENODO.5705394

Stoll, M., Huber, F. M., Trumm, M., Enzmann, F., Meinel, D., Wenka, A., et al. (2019). Experimental and numerical investigations on the effect of fracture geometry and fracture aperture distribution on flow and solute transport in natural fractures. *Journal of Contaminant Hydrology*, *221*, 82–97. https://doi.org/10.1016/j.jconhyd.2018.11.008

Sudakov, O., Burnaev, E., & Koroteev, D. (2019). Driving digital rock towards machine learning: Predicting permeability with gradient boosting and deep neural networks. *Computers & Geosciences*, *127*, 91–98. https://doi.org/10.1016/j.cageo.2019.02.002

Suzuki, A., Watanabe, N., Li, K., & Horne, R. N. (2017). Fracture network created by 3-D printer and its validation using CT images. *Water Resources Research*, *53*(7), 6330–6339. https://doi.org/10.1002/2017WR021032

Suzuki, A., Minto, J. M., Watanabe, N., Li, K., & Horne, R. N. (2019). Contributions of 3D Printed Fracture Networks to Development of Flow and Transport Models. *Transport in Porous Media*, *129*(2), 485–500. https://doi.org/10.1007/s11242-018-1154-7

Suzuki, A., Miyazawa, M., Okamoto, A., Shimizu, H., Obayashi, I., Hiraoka, Y., et al. (2020). Inferring fracture forming processes by characterizing fracture network patterns with persistent homology. *Computers & Geosciences*, *143*, 104550. https://doi.org/10.1016/j.cageo.2020.104550

Suzuki, A., Miyazawa, M., Minto, J. M., Tsuji, T., Obayashi, I., Hiraoka, Y., & Ito, T. (2021). Flow estimation solely from image data through persistent homology analysis. *Scientific Reports*, *11*(1), 17948. https://doi.org/10.1038/s41598-021-97222-6

Tatone, B. S. A., & Grasselli, G. (2012). Quantitative Measurements of Fracture Aperture and Directional Roughness from Rock Cores. *Rock Mechanics and Rock Engineering*, *45*(4), 619–629. https://doi.org/10.1007/s00603-011-0219-5

Tatone, B. S. A., & Grasselli, G. (2013). An Investigation of Discontinuity Roughness Scale Dependency Using High-Resolution Surface Measurements. *Rock Mechanics and Rock Engineering*, *46*(4), 657–681. https://doi.org/10.1007/s00603-012-0294-2

Tatone, B. S. A., & Grasselli, G. (2015). Characterization of the effect of normal load on the discontinuity morphology in direct shear specimens using X-ray micro-CT. *Acta Geotechnica*, *10*(1), 31–54. https://doi.org/10.1007/s11440-014-0320-5

Thiele, S. T., Jessell, M. W., Lindsay, M., Ogarko, V., Wellmann, J. F., & Pakyuz-Charrier, E. (2016). The topology of geology 1: Topological analysis. *Journal of Structural Geology*, *91*, 27–38. https://doi.org/10.1016/j.jsg.2016.08.009

Thomas, R. D., & Ward, D. C. (1972). Effect of Overburden Pressure and Water Saturation on Gas Permeability of Tight Sandstone Cores. *Journal of Petroleum Technology*, *24*(02), 120–124. https://doi.org/10.2118/3634-pa

Thörn, J., & Fransson, Å. (2015). A new apparatus and methodology for hydromechanical testing and geometry scanning of a rock fracture under low normal stress. *International Journal of Rock Mechanics and Mining Sciences*, *79*, 216–226. https://doi.org/10.1016/j.ijrmms.2015.08.015

Thörn, J., Ericsson, L. O., & Fransson, Å. (2015). Hydraulic and Hydromechanical Laboratory Testing of Large Crystalline Rock Cores. *Rock Mechanics and Rock Engineering*, *48*(1), 61–73. https://doi.org/10.1007/s00603-013-0538-9

Torskaya, T., Shabro, V., Torres-Verdín, C., Salazar-Tio, R., & Revil, A. (2014). Grain Shape Effects on Permeability, Formation Factor, and Capillary Pressure from Pore-Scale Modeling. *Transport in Porous Media*, *102*(1), 71–90. https://doi.org/10.1007/s11242-013-0262-7

Tsang, C.-F. (1991). Coupled hydromechanical-thermochemical processes in rock fractures. *Reviews of Geophysics*, *29*(4), 537–551. https://doi.org/10.1029/91rg01832

Tsang, C.-F. (2024). Coupled Thermo-Hydro-Mechanical Processes in Fractured Rocks: Some Past Scientific Highlights and Future Research Directions. *Rock Mechanics and Rock Engineering*, *57*(8), 5303–5316. https://doi.org/10.1007/s00603-023-03676-7

Tsang, C.-F., & Neretnieks, I. (1998). Flow channeling in heterogeneous fractured rocks. *Reviews of Geophysics*, *36*(2), 275–298. https://doi.org/10.1029/97RG03319

Tsang, Y. W. (1992). Usage of “Equivalent apertures” for rock fractures as derived from hydraulic and tracer tests. *Water Resources Research*, *28*(5), 1451–1455. https://doi.org/10.1029/92WR00361

Unger, A. J. A., & Mase, C. W. (1993). Numerical study of the hydromechanical behavior of two rough fracture surfaces in contact. *Water Resources Research*, *29*(7), 2101–2114. https://doi.org/10.1029/93WR00516

Viswanathan, H. S., Ajo-Franklin, J., Birkholzer, J. T., Carey, J. W., Guglielmi, Y., Hyman, J. D., et al. (2022). From Fluid Flow to Coupled Processes in Fractured Rock: Recent Advances and New Frontiers. *Reviews of Geophysics*, *60*(1). https://doi.org/10.1029/2021RG000744

Vogler, D., Amann, F., Bayer, P., & Elsworth, D. (2016). Permeability Evolution in Natural Fractures Subject to Cyclic Loading and Gouge Formation. *Rock Mechanics and Rock Engineering*, *49*(9), 3463–3479. https://doi.org/10.1007/s00603-016-1022-0

Vogler, D., Settgast, R. R., Annavarapu, C., Madonna, C., Bayer, P., & Amann, F. (2018). Experiments and Simulations of Fully Hydro-Mechanically Coupled Response of Rough Fractures Exposed to High-Pressure Fluid Injection. *Journal of Geophysical Research: Solid Earth*, *123*(2), 1186–1200. https://doi.org/10.1002/2017JB015057

Walsh, J. B. (1981). Effect of pore pressure and confining pressure on fracture permeability. *International Journal of Rock Mechanics and Mining Sciences & Geomechanics Abstracts*, *18*(5), 429–435. https://doi.org/10.1016/0148-9062(81)90006-1

Wang, C., Elsworth, D., & Fang, Y. (2019). Ensemble Shear Strength, Stability, and Permeability of Mixed Mineralogy Fault Gouge Recovered From 3D Granular Models. *Journal of Geophysical Research: Solid Earth*, *124*(1), 425–441. https://doi.org/10.1029/2018JB016066

Wang, C., Elsworth, D., Fang, Y., & Zhang, F. (2020). Influence of fracture roughness on shear strength, slip stability and permeability: A mechanistic analysis by three-dimensional digital rock modeling. *Journal of Rock Mechanics and Geotechnical Engineering*, *12*(4), 720–731. https://doi.org/10.1016/j.jrmge.2019.12.010

Wang, M., Chen, Y.-F., Ma, G.-W., Zhou, J.-Q., & Zhou, C.-B. (2016). Influence of surface roughness on nonlinear flow behaviors in 3D self-affine rough fractures: Lattice Boltzmann simulations. *Advances in Water Resources*, *96*, 373–388. https://doi.org/10.1016/j.advwatres.2016.08.006

Wang, Q., Hu, X., Zheng, W., Li, L., Zhou, C., Ying, C., & Xu, C. (2021). Mechanical Properties and Permeability Evolution of Red Sandstone Subjected to Hydro-mechanical Coupling: Experiment and Discrete Element Modelling. *Rock Mechanics and Rock Engineering*, *54*(5), 2405–2423. https://doi.org/10.1007/s00603-021-02396-0

Watanabe, N., Hirano, N., & Tsuchiya, N. (2008). Determination of aperture structure and fluid flow in a rock fracture by high-resolution numerical modeling on the basis of a flow-through experiment under confining pressure. *Water Resources Research*, *44*(6). https://doi.org/10.1029/2006WR005411

Weede, M., & Hötzl, H. (2005). Strömung und Transport in einer natürlichen Einzelkluft in poröser Matrix—Experimente und Modellierung. *Grundwasser*, *10*(3), 137–145. https://doi.org/10.1007/s00767-005-0090-y

Welch, N. J., Carey, J. W., Frash, L. P., Hyman, J. D., Hicks, W., Meng, M., et al. (2022). Effect of Shear Displacement and Stress Changes on Fracture Hydraulic Aperture and Flow Anisotropy. *Transport in Porous Media*, *141*(1), 17–47. https://doi.org/10.1007/s11242-021-01708-w

Wenning, Q. C., Madonna, C., Kurotori, T., & Pini, R. (2019). Spatial Mapping of Fracture Aperture Changes With Shear Displacement Using X-ray Computerized Tomography. *Journal of Geophysical Research: Solid Earth*, *124*(7), 7320–7340. https://doi.org/10.1029/2019JB017301

Westerman, A. R. (1981). *The development of secondary porosity and permeability in fractured rock*. Durham University. Retrieved from http://etheses.dur.ac.uk/7840/

Wilkins, A., Green, C., & Ennis-King, J. (2020). PorousFlow: a multiphysics simulation code for coupled problems in porous media. *Journal of Open Source Software*, *5*(55), 2176. https://doi.org/10.21105/joss.02176

Wilkins, A., Green, C. P., & Ennis-King, J. (2021). An open-source multiphysics simulation code for coupled problems in porous media. *Computers & Geosciences*, *154*, 104820. https://doi.org/10.1016/j.cageo.2021.104820

Witherspoon, P. A., Wang, J. S. Y., Iwai, K., & Gale, J. E. (1980). Validity of Cubic Law for fluid flow in a deformable rock fracture. *Water Resources Research*, *16*(6), 1016–1024. https://doi.org/10.1029/WR016i006p01016

Wu, C. (2007). SiftGPU: A GPU implementation of Scale Invariant Feature Transform (SIFT).

Wu, C. (2013). Towards Linear-time Incremental Structure From Motion. *2013 International Conference on 3D Vision*, 127–134. https://doi.org/10.1109/3DV.2013.25

Wu, C., Agarwal, S., Curless, B., & Seitz, S. M. (2011). Multicore bundle adjustment. *CVPR 2011*, 3057–3064. https://doi.org/10.1109/CVPR.2011.5995552

Xiong, X., Li, B., Jiang, Y., Koyama, T., & Zhang, C. (2011). Experimental and numerical study of the geometrical and hydraulic characteristics of a single rock fracture during shear. *International Journal of Rock Mechanics and Mining Sciences*, *48*(8), 1292–1302. https://doi.org/10.1016/j.ijrmms.2011.09.009

Yeo, I. W., De Freitas, M. H., & Zimmerman, R. W. (1998). Effect of shear displacement on the aperture and permeability of a rock fracture. *International Journal of Rock Mechanics and Mining Sciences*, *35*(8), 1051–1070. https://doi.org/10.1016/S0148-9062(98)00165-X

Zambrano, M., Tondi, E., Mancini, L., Lanzafame, G., Trias, F. X., Arzilli, F., et al. (2018). Fluid flow simulation and permeability computation in deformed porous carbonate grainstones. *Advances in Water Resources*, *115*, 95–111. https://doi.org/10.1016/j.advwatres.2018.02.016

Zambrano, M., Pitts, A. D., Salama, A., Volatili, T., Giorgioni, M., & Tondi, E. (2019). Analysis of Fracture Roughness Control on Permeability Using SfM and Fluid Flow Simulations: Implications for Carbonate Reservoir Characterization. *Geofluids*, *2019*, 1–19. https://doi.org/10.1155/2019/4132386

Zhang, Y., & Zhao, G.-F. (2020). A global review of deep geothermal energy exploration: from a view of rock mechanics and engineering. *Geomechanics and Geophysics for Geo-Energy and Geo-Resources*, *6*(1), 4. https://doi.org/10.1007/s40948-019-00126-z

Zhao, Z. (2013). Gouge Particle Evolution in a Rock Fracture Undergoing Shear: a Microscopic DEM Study. *Rock Mechanics and Rock Engineering*, *46*(6), 1461–1479. https://doi.org/10.1007/s00603-013-0373-z

Zimmerman, R. W., & Bodvarsson, G. S. (1996). Hydraulic conductivity of rock fractures. *Transport in Porous Media*, *23*(1). https://doi.org/10.1007/BF00145263

Zimmermann, G., Moeck, I., & Blöcher, G. (2010). Cyclic waterfrac stimulation to develop an Enhanced Geothermal System (EGS)—Conceptual design and experimental results. *Geothermics*, *39*(1), 59–69. https://doi.org/10.1016/j.geothermics.2009.10.003

Zomorodian, A., & Carlsson, G. (2005). Computing Persistent Homology. *Discrete & Computational Geometry*, *33*(2), 249–274. https://doi.org/10.1007/s00454-004-1146-y

Acknowledgements

I am grateful to many people who have supported me on this journey. This thesis would not have been possible without them.

Thus, I would like to thank …

… my supervisor, Prof. Dr. Philipp Blum, for providing me the opportunity to do a PhD in a great working group. I want to thank you for giving me the freedom to develop my own research, the many insightful conversations and discussions, and, of course, for always keeping things short and simple.

… Prof. Dr. Martin O. Saar for his willingness to be my co-examiner.

… Prof. Dr. Christoph Hilgers and Prof. Dr. Hans-Henning Stutz for being part of my doctoral committee.

… Dr. Luc Scholtès for giving me the opportunity of my stay in Clermont-Ferrand, the great working environment, and the countless discussions about rock mechanics and DEM models. I had a wonderful time in Clermont and will always remember that cheese can – and should – be eaten with the rind.

… my co-authors Dr. Sina Hale, Larissa Blesch, Dr. Gabriel Rau, PD Dr. Kathrin Menberg, Dr. Anna Suzuki, Togo Hasumi, and PD Dr. Guido Blöcher for the great collaboration and the support in paper-writing.

… Nicole Suteu and Christine Mackert for their support in administrative matters.

… Kevin Altinger, for his support with all technical matters, and in particular for his assistance with the NMR measurements conducted in Kiel.

… Dr. Hagen Steger, for his support with laboratory and field experiments, and for the many enjoyable lunch breaks together.

… Dr. Ruben Stemmle for the great time as office roommates and the sociable atmosphere, as well as for the help reviewing this thesis. I will always remember that discipline is better than motivation.

… all my colleagues and friends from the Engineering Geology and Hydrogeology group for the great time in the office, on field trips, at conferences, and especially outside the university. You created a great atmosphere in which I felt comfortable and welcome throughout my entire time at KIT.

… all other colleagues at AGW and IBF who supported me with my research during my time as a PhD student at KIT.

… the Graduate School “Enabling Net Zero” (ENZo), and in particular Heike Kull, for the numerous opportunities to grow both scientifically and personally, for the engaging evening lectures, and not least for the annual retreats, which I always thoroughly enjoyed. Special thanks also go to Laksh Narayanan Palaniswamy and Xheni Garipi for the productive yet enjoyable time working on our project.

… the Karlsruhe House of Young Scientists (KHYS) as well as the InVolc Graduate Track of the Université Clermont Auvergne for the funding of my research stays in Clermont-Ferrand.

… last but not least, my family and friends, especially my parents Monika and Jürgen Fuchs, as well as my wonderful fiancée Magdalena Broß. This work would not have been possible without your continuous support and belief in me. Thank you for celebrating the good times with me and cheering me up during the difficult ones. Thank you for always being there!

Declaration of authorship

Study 1 (Chapter 2)

Fuchs, M., Hale, S., Blesch, L., Rau, G. C., Menberg, K., Blum, P. (2024): Evaluating Fracture Surface Imaging Methods Using Flow Simulations and Air Permeameter Measurements. Rock Mechanics and Rock Engineering 57, 1849–1860, https://doi.org/10.1007/s00603-023-03615-6

Marco Fuchs: Writing – original draft, Conceptualization, Methodology, Visualization, Software, Investigation, Writing – review & editing. Sina Hale: Conceptualization, Investigation, Supervision, Writing – review & editing. Larissa Blesch: Investigation. Gabriel C. Rau: Supervision, Writing – review & editing. Kathrin Menberg: Writing – review & editing. Philipp Blum: Conceptualization, Funding acquisition, Supervision, Writing – review & editing.

Study 2 (Chapter 3)

Fuchs, M., Suzuki, A., Hasumi, T., Blum, P. (2024): Investigating rough single-fracture permeabilities with persistent homology. Solid Earth 15, 353-365, https://doi.org/10.5194/se-15-353-2024

Marco Fuchs (MF), Anna Suzuki (AS), and Philipp Blum (PB) initiated the key concepts. MF prepared the data for persistent homology analysis, performed numerical simulations, conducted air permeameter measurements, and visualized the results. AS performed the persistent homology analysis and supervised the research. Togo Hasumi (TH) assisted with the persistent homology analysis. PB supervised the research. MF wrote the original draft. All authors reviewed and edited the paper.

Study 3 (Chapter 4)

Fuchs, M., Blum, P., Blöcher, G., Scholtès, L.: Permeability evolution and gouge formation during fracture shearing. Geophysical Research Letters, e2025GL117217. https://doi.org/10.1029/2025GL117217

Marco Fuchs: Conceptualization, Investigation, Methodology, Software, Validation, Visualization, Writing – original draft, Writing – review & editing. Philipp Blum: Conceptualization, Supervision. Writing – review & editing. Guido Blöcher: Investigation, Supervision, Validation, Writing – review & editing. Luc Scholtès: Conceptualization, Methodology, Software, Supervision, Validation, Writing – original draft, Writing – review & editing.